INVESTIGATION OF LASER DISCHARGE IN A SUPERSONIC FLOW AND SHOCK WAVE LAMINAR BOUNDARY LAYER INTERACTION IN A HYPERSONIC FLOW

by

MAHSAALSADAT MORTAZAVI RAVARI

A dissertation submitted to the

School of Graduate Studies

Rutgers, The State University of New Jersey

in partial fulfillment of the requirements

for the degree of

Doctor of Philosophy

Graduate Program in Mechanical and Aerospace Engineering

Written under the direction of

Doyle Knight

and approved by

____

____

____

____

New Brunswick, New Jersey

January, 2018

ABSTRACT OF THE DISSERTATION

Investigation of Laser Discharge in a Supersonic Flow and Shock Wave Laminar Boundary Layer Interaction in a Hypersonic Flow

By Mahsaalsadat Mortazavi Ravari

Dissertation Director:

Doyle Knight

In this Ph.D. dissertation, two separate phenomena have been numerically studied: flow control using a laser discharge in a supersonic flow and laminar shock wave boundary layer interaction in a hypersonic flow. In the first section of the study, the interaction of a laser-generated plasma with a hemisphere cylinder at Mach 3.45 is simulated using the Euler and Navier Stokes equations, separately and assuming a perfect gas with no chemical reactions in the laser discharge. The instantaneous laser discharge creates a plasma region which in this study is assumed to be spherical. From this spherical plasma region, a blast wave and an expansion wave form which propagate radially outward and inward, respectively. The heated region convects with the flow and interacts with the blunt body shock in the upstream of the hemisphere and changes the flow structure and parameters in that region. The impact of the blast wave with the hemisphere surface momentarily raises the pressure on the hemisphere. When the heated region reaches the blunt body shock lensing of the shock wave occurs and a toroidal vortex forms due to the Richtmyer-Meshkov instability; as a result, the pressure on the hemisphere drops momentarily. Later on, the flow parameters converge to their steady state condition

as the heated region convects to the downstream of the hemisphere. The results are compared with experimental data of a separate study to validate the numerical model used in these simulations.

To investigate the hypersonic shock wave laminar boundary layer interaction, two separate geometric configurations are used: axisymmetric flow over a hollow-cylinder flare, and three-dimensional flow over a cylindrically blunted fin mounted on a flat plate. In the first case, the capability of the chosen numerical model in predicting the pressure and heat transfer in a hypersonic shock wave boundary layer interaction over an axisymmetric hollow cylinder flare at a Mach 10 flow is investigated. In the second case, the assessment of the capability of a laminar perfect gas model to predict the heat transfer in a three-dimensional hypersonic flow with shock wave boundary layer interaction was studied. In this study, the freestream Mach number and Reynolds number - based on the diameter of the cylindrical fin - are 14 and 8,000, respectively. Numerical heat transfer on the blunt fin is compared with the experimental data for validation. Moreover, investigation of the effects of the sweep angle of the blunt fin on the shock wave boundary layer interaction is the other objective of this research. Three discrete sweep angles of zero, 22.5 and 45 degree have been chosen and comparison of their results have been made.

It has been shown that the adverse pressure gradient imposed from the shock wave to the boundary layer can separate the boundary layer. The separation shock wave formed over the separated region can interact with the other shock waves and create a lambda shock wave structure with a transmitted shock wave. As the separated boundary layer reattaches to the surface, it increases the localized heat transfer and produces a reattachment shock wave, which increases the pressure on the surface of the vehicle. The localized high aerothermodynamic loads as well as the low frequency oscillations regarding the shock wave boundary layer interaction impose design limitations on the hypersonic aircrafts and show the importance of fully understanding the physics behind these phenomena as well as gaining the ability to predict the flow with such interactions.

Acknowledgements

It is with immense gratitude that I acknowledge my adviser Professor Doyle Knight for his patience, motivation, and immense knowledge. I owe the completion of my degree to his consideration on my academic requirements. During the past years, his attitude has continually conveyed a spirit of excitement in regard to research and teaching. I wish to thank his guidance, support, and attention. I could not have imagined having a better advisor and mentor for my Ph.D studies.

Besides my adviser, I would like to thank my committee members Professor Hao Lin and Professor Michael Muller from the Department of Mechanical and Aerospace Engineering, as well as Dr. Olga Azarova from Dorodnicyn Computing Centre, Federal Research Center Computer Science and Control of Russian Academy of Sciences. Moreover, this thesis would not have been possible unless for the scholarships I have received from Rutgers Engineering School.

Foremost, I would like to express my gratitude to God in the first place and then to my lovely and supportive parents and brother Mitra Akhgar, Mansour Mortazavi and Milad Mortazavi, to whom I owe my whole life. It gives me great pleasure to thank my dear friends Shirin Estahbanati, Sonia Razavi and Behnam Tavakkol, who filled the absence of my family when they were oceans away.

Dedication

To my lovely parents and brother

Table of Contents

Abstract ii

Acknowledgements iv

Dedication v

1. Introduction 1

2. Methodology 12

2.1. Governing Equations 12

2.2. Numerical Algorithm 13

2.2.1. Finite Volume Method 13

2.2.2. Inviscid Fluxes 18

Roe's Method 19

Van Leer's Method 21

2.2.3. Reconstruction 24

First Order 24

MUSCL 25

Modified ENO 28

Van Albada's Limiter 30

2.2.4. Viscous Fluxes 31

2.2.5. Time Integration 33

Time Step 33

Runge-Kutta Method 34

DPLR's Method 34

Dual-Time Stepping Method 39

Gauss-Seidel Relaxation Method 40

2.2.6. Message Passing Interface (MPI) 40
2.2.7. Boundary Condition 40
Fixed Boundary Condition 41
Zero Gradient Boundary Condition 41
Symmetry or Slip Boundary Condition 41
No-slip Adiabatic Boundary Condition 42
No-slip Isothermal Boundary Condition 42
Internal Boundary Condition 42
2.2.8. Challenges of High Gradients 42

3. Description of the Experiments 44
3.1. Adelgren *et.al.* Experiment 44
3.2. Chanetz *et.al.* Experiment 47
3.3. Hiers *et al.* Experiment 49

4. Numerical Simulation Methods 52
4.1. Numerical Simulation of Adelgren *et.al.* Experiment 52
4.1.1. Inviscid Model 55
4.1.2. Viscous Model 56
4.1.3. Determination of Laser Discharge Parameter ($\Delta T/T_\infty$) 56
4.2. Numerical Simulation of Chanetz *et.al.* Experiment 57
4.3. Numerical Simulation of Hiers *et.al.* Experiment 58
4.3.1. Grid Generation 59
Grid-Refinement Study 64

5. Results 67
5.1. Numerical Simulation of Adelgren *et.al.* Experiment 67
5.1.1. Steady State 67
5.1.2. Flow Structure in Unsteady Simulation 68
5.1.3. Drag Coefficient 70

5.1.4. Comparison with Experiment 73

5.2. Numerical Simulation of Chanetz *et.al.* Experiment 75

5.3. Numerical Simulation of Hiers *et.al.* Experiment 79

6. Conclusion 105

References 108

Chapter 1

Introduction

There is a renewed interest in aerospace vehicles with speeds ranging from supersonic to hypersonic in the past few decades [1]. From the Wright brothers who built the first successful airplane in 1903 [2], the technology of the airplane has enhanced and the further accomplishments have even made outerspace accessible. An example of the growing interest in advancing high speed flight is the funding that NASA provided to two private companies (SpaceX and Orbital Sciences Corporation) to build space capsules in order to transmit cargo and eventually crew to the International Space Station. Moreover, Space Exploration Technologies Corporation (SpaceX), aims to reduce space transportation costs by manufacturing reusable spacecraft [3]. The Boeing X-37 is another example of a reusable unmanned spacecraft, which is designed to re-enter the Earth's atmosphere after its launch and land as a spaceplane [4]. Moreover, the Orion Multi-Purpose Crew Vehicle (Orion MPCV) is a spacecraft designed to carry a crew of four to low Earth orbit (LEO) or beyond, and it intends to facilitate human exploration of asteroids and Mars [5]. In addition, Virgin Galactic will provide access to the public to launch from the Earth and travel at Mach number 3.5 and have several minutes of weightlessness with multiple windowed views of our home planet. Up to now, there have been around 700 people from all over the world who have reserved places to fly on Virgin Galactic's reusable space launch system [6].

This Ph.D. dissertation focuses on two critical aspects of modern high speed flights, namely, 1) flow control and drag reduction using energy deposition, and 2) analysis of aerothermodynamic loads due to shock wave boundary layer interaction. As the speed of the vehicle increases, the importance of the flexibility and maneuverability of the aircraft becomes more significant. In high speed flights a little delay in altering the direction of the aircraft creates a considerable difference in the resulting location of the vehicle. Consequently, flow control in high speed flights to increase the maneuverability of the aircraft is an important research topic of recent studies. Additionally, drag reduction for aerodynamic vehicles is another important design objective due to the benefit of improved fuel efficiency and increased range of flexibility in operation.

Shock wave boundary layer interaction can create very complex flow structures and cause low frequency unsteadiness and damage the vehicle's structure or limit its performance. In addition, shock wave boundary layer interactions are the origin of severe aero-heating problems when the shock wave is strong enough to separate the boundary layer. Improving the capability of CFD models to predict the aerothermodynamic loads on the vehicle due to shock wave boundary layer interaction and using flow control techniques to improve high speed aircrafts are open research objectives. The numerical simulation of these phenomena is the objective of this PhD dissertation.

There have been many studies in regard of reducing the drag on the aircraft in order to increase the efficiency of the flight. One method of reducing drag in supersonic flights is a physical spike in front of the vehicle to produce conical shock waves and reduce the local Mach number in front of the vehicle. The spike creates a recirculation region, which acts like aerodynamic streamlining of the aircraft's body [7, 8]. However, this method has disadvantages regarding the large pitching moment generated in the flight and large heat transfer rate at the apex. More recent studies show the possibility of drag reduction using energy deposition [9]. Pulsed laser or microwave discharge in front of a blunt body changes the flow structure after the shock wave and reduces the drag without the disadvantages of the spike.

Many studies have been performed in the past few decades to explain the physical phenomena behind the energy discharge in a supersonic flow. Belokon *et al.* [10] analytically studied the two-dimensional energy disposition using the linearized inviscid equations and a defined energy source function. Krasnobaev and Syunyaev [11] used a three dimensional energy source function and solved it analytically and observed the static pressure drop due to the energy discharge. In later analytical studies, Krasnobaev [12] and Terent'eva [13] extended the linearized supersonic solutions for a general energy source function in two and three dimensional spaces, respectively.

In addition to analytical studies, experimental investigations have been conducted to understand the physics behind laser discharge in a supersonic flow. Tretyakov *et al.* [14, 15] studied the drag reduction for laser discharge upstream a cone cylinder and a hemisphere in argon and CO_2 at Mach 2. They investigated the effect of the location of the laser discharge on the drag of the model. Zaidi *et al.* [16] examined a single pulse laser discharge upstream of a 10 degree half-angle wedge at Mach 2.4. They studied the interaction of the plasma region with the oblique shock both experimentally and numerically and observed the blast wave generated from the energy deposition and its effects on the shock generated from the wedge surface. Adelgren *et al.* [17] observed a momentary pressure drop on the sphere surface when a laser discharge is applied upstream in a supersonic flow. Sakai *et al.* [18] showed that increasing instability in the stagnation region enhances the drag reduction.

There have been many numerical studies to achieve a deeper understanding of the flow with energy deposition in a supersonic regime. Vlasov *et al.* [19] solved the two dimensional Euler equations for the cases where the energy discharge is upstream, downstream and interacting with the shock wave. Levin and Terent'eva [20] considered a steady symmetric Gaussian function for the energy deposition source with zero degree angle of attack and solved the Euler equations for a supersonic flow past a cone. They found the most effective location of the energy discharge with the fixed energy deposited and freestream Mach number. They further simulated a steady asymmetric Gaussian energy source function with non-zero angle of attack [21]. They observed that adding a positive angle of attack to the energy deposition location reduces the drag and increases the lift on the cone. Riggins *et al.* [22] and Riggins and Nelson [23] used a laminar viscous model and computed the steady energy deposition in a supersonic flow past a hemisphere. They captured the vortices generated due to the interaction of the heated region with the blunt body shock. Georgievskii and Levin [24] numerically solved the Euler equations for supersonic flow past a sphere at Mach 3. They modeled the energy deposition as an initial condition with uniform reduced density. They observed lensing of the shock (*i.e.* upstream motion of the blunt body shock) with the interaction of the heated region. Furthermore, they captured an expansion wave generated from the interaction of the thermal spot with the blunt body shock which propagates to the sphere and momentarily reduces the surface pressure. They further examined the effect of the size of the heated region on the drag reduction [25]. Kandala and Candler [26] numerically studied the energy absorption mechanism in a laser discharge by solving Navier-Stokes equations assuming thermochemical nonequilibrium. An 11-species thermochemical model was used for the air to account for real gas effects and a radiation model was used to simulate the laser pulse. They studied energy deposition in supersonic flow past a sphere and verified the pressure jump due to the interaction of the blast wave with the sphere surface and the decrease of the static pressure on the body associated with the expansion waves reaching the sphere. Ogino *et al.* [27] numerically studied the interaction of the blast wave with the normal shock wave in a supersonic flow past a sphere using an inviscid perfect gas model and focused on hydrodynamic effects on drag reduction due to this interaction.

With the exception of the simulation by Kandala and Candler [26], the aforementioned numerical investigations are based on the Euler or Navier-Stokes equations for a perfect gas. This approach assumes that the principal physical phenomena of the interaction are thermal, *i.e.*, attributable to the change in temperature (specifically, translational-rotational temperature) of the gas by the laser discharge. In other words, the laser discharge generates a volume of fluid with a lower Mach number (compared to the freestream) which upon interaction with the shock structure of the aerodynamic body results in movement of the shock (lensing), generation of expansion wave propagating to the body and hence momentary reduction in surface pressure. There are several reasons to assume such an approach is an accurate representation of the physics of the interaction. A simple one-dimensional gas dynamic analysis [17] demonstrates the aforementioned phenomena. Moreover, the cited numerical investigations display qualitative agreement with experiment. However, the main limitation of this approach is the requirement of an empirical model for the laser discharge consistent with the Euler (or Navier-Stokes) modeling. In other words, the complex thermochemical processes accompanying the laser discharge and the resultant heated plasmoid must be parameterized in some manner that provides an initial temperature, pressure and velocity distribution in an assumed bounded region in space. If such an empirical model can be found that provides accurate prediction of the interaction of the laser discharge with an aerodynamic body, then the Euler (or Navier-Stokes) modeling would constitute an efficient method for predicting the effect of the laser discharge on the aerodynamic performance of a realistic vehicle.

The experiment conducted by Adelgren *et al*. [17] is one of the selected problems for examination in this PhD dissertation. There have been only few numerical studies on this case [28]. The experiment consists of an instantaneous laser discharge upstream a sphere in a supersonic flow with Mach number 3.45. The simulation has been conducted using the commercial code GASPex [29] and its objective is the assessment of a simple laser discharge model to accurately predict the interaction of a laser discharge with a simplified aerodynamic body using the Euler or Navier-Stokes equations with the assumption of a perfect gas. The laser discharge model is based on the minimum number of empirical parameters. A single experimental data point is used to define the model. The resultant time-dependent flowfield is compared with the experiment to assess the validity of the model.

Furthermore, in order to obtain a deeper understanding of high speed flows, shock wave laminar boundary layer interaction is investigated in this Ph.D. dissertation. The complicated structure of the shock wave boundary layer interaction is due to the adverse pressure gradient that the shock wave imposes on the boundary layer and creates a separation region, causing a strong alteration in the velocity profile [30]. This interaction can change the whole structure of the flow field and create intense vortices and complex shock patterns. Shock wave boundary layer interaction is an example of a coupling of an inviscid phenomena (shock waves) with a viscous boundary layer, which requires clear understanding of both regimes. The investigation of shock wave boundary layer interaction has started since the early 1940s [31, 32, 33, 34]. Many studies have been devoted to understanding the physics of shock wave boundary layer interaction and the assessment of the capability of the existing numerical models in predicting the flow parameters and structures. Some examples of these attempts are research conducted by Chantez [35, 36], Bur [37], Boldyrev [38] and Swantek [39]. In their works experimental and numerical simulations have been performed to study the fundamentals of laminar/turbulent transition, real gas effects, heat transfer distributions, the effect of ramped leading edge and many other topics related to shock wave boundary layer interaction.

In an extensive experimental study, Holden and Wadhams [40] presented measurements of heat transfer and pressure as well as Schlieren photographs for variety of models with hollow cylinder flare and double cone configurations. The main objective of this research was to provide detailed experimental database of surface and flow field measurements to be used for assessment of the capabilities of the current numerical models in prediction of surface loads. The results of a blind comparison of these experimental measurements and some numerical calculations have been presented in a paper by Harvey *et.al* [41]. Moreover, a series of experiments on two models of a double cone configuration with Edney type VI and V shock interactions have been performed by Wright *et.al.* [42]. The comparison of the computations with the experiment illustrates more agreement for the results of the type IV, compared with the type V shock interaction. Moreover, the study showed that for the type V interaction and a laminar flow, the separation size increases by increase in the Reynolds number; whereas the opposite trend is observed for a turbulent flow.

Moreover, Neuenhahn and Olivier [43] experimentally investigated the two-dimensional shock wave laminar boundary layer interaction in a blunted double wedge configuration and studied the effect of the elevated wall temperature on the extent of the separation. They showed that an increase in wall temperature increases the size of the separation region for all leading edge bluntness radii. Coet *et al*. [44, 45] showed that the bluntness of the plate reduces the aerothermodynamic loads due to the reduction of the speed of the flow from hypersonic to supersonic regime at the shock wave boundary layer interaction region. Borovoy *et al.* [46] obtain the same result with the effect of the plate's bluntness on the heat transfer rate at the interaction region due to increase in the separation bubble size and decrease in the gas density in the high-entropy layer.

Moreover, they showed that as the radius of the plate's bluntness increases, the heat transfer rate decreases to a certain threshold value for the bluntness radius. They further observed that by increase in freestream Mach number, the threshold value decays and the effect of the bluntness of the plate on the heat transfer rate enhances.

In a numerical simulation, John and Kulkarni studied the effect of the leading edge bluntness on the extent of the separation bubble size in a two-dimensional hypersonic shock wave laminar boundary layer interaction [47]. They showed that the extent of the separation region increases by increase in leading edge radius until a maximum separation size is reached at a critical radius, referred to as "inversion radius". The size of the separation region decreases by further increase in the bluntness leading edge radius. The maximum separation size corresponds to the equality of the entropy and boundary layer thicknesses. In further investigation of John and Kulkarni [48] they numerically analyzed a two-dimensional ramp-induced shock wave laminar boundary layer interaction and studied the extent of upstream influence, separation bubble size and peak heat transfer.

In addition, Needham and Stollery [49] and Holden [50] investigated the parameters that affect the location of the flow separation region, separation bubble size and the extent of upstream influence. They found out that freestream Mach number, local Reynolds number, specific heat ratio, temperature, *etc* have the most effect on the mentioned parameters. Hankey and Holden [51] showed that the effect of the upstream parameters increase with increase in the ramp angle and it decreases with increase in Mach number. Katzer [52] concluded that the extent of the separation region normalized with the displacement thickness scales with the strength of the shock wave and the inverse of the viscous interaction parameter.

Moreover, Druguet and Candler [53] studied the effect of the numerical flux algorithm and slope limiter for a hypersonic flow past a double cone. They showed that for a realistic case, where the grid spacing is not sufficiently small, the numerical results depend strongly on the dissipativity of the numerical flux method and limiter. In another attempt of a numerical simulation, Gaitonde *et.al.* [54] assessed the capabilities of a numerical model in prediction of surface loads in a hypersonic shock wave laminar boundary layer interaction in a two-dimensional double cone configuration. In addition, Grasso and Marini [55] numerically studied hypersonic shock wave laminar boundary layer interaction over wing-flap and wing-fuselage junction configurations. They analyzed the influence of Mach number, viscous interaction parameters, and geometric parameters such as control surface deflection angle, sweep angle and the leading edge shape. They further established scaling laws for the extent of the upstream influence. Moreover, Olejniczak *et.al.* [56] numerically investigated different types of shock interactions in a double wedge geometry. They observed that standard Edney types IV, V and VI, as well as a new interaction can occur in this configuration. They further showed that these flows are highly dependent on the grid resolution in order to simulate the accurate interaction.

In addition, Nompelis *et al.* [57] investigated the high enthalpy effects on hypersonic shock wave boundary layer interaction in a double cone flow, both experimentally and numerically. They observed improvement of the agreement of the numerical results with the experiment at lower total enthalpies. Further numerical investigation of hypersonic shock wave laminar boundary layer interaction on a hollow cylinder flare by Gnoffo [58] showed the sensitivity of the predicted location of the separation point on the grid spacing. These numerical calculations proposed significant influence of the freestream Reynolds number on the extent of separation. Moreover, flow unsteadiness was observed for their calculations regarding to the double-cone geometry. Roy *et al.* [59] used DSMC and Navier-Stokes simulations to study hypersonic laminar flows past a blunted double cone model. They showed that insufficient grid refinement in the rarefied biconic simulations create discrepancies for the DSMC simulation approach.

Marini [60] further investigated the effect of the flow and geometric parameters on shock wave boundary layer interaction in two dimensional configurations by numerical and experimental approaches. He studied the effect of geometric variables such as flap deflection and leading edge shape, as well as flow characteristics including Reynolds number and equilibrium real gas assumption. His study attempted to reach to appropriate scaling laws for separation characteristics and aerothermodynamic loads to be used in design of hypersonic vehicles.

In addition, Gai and Hayne [61] considered high enthalpy hypersonic flow behind a step and numerically studied the heat transfer rate, showing that it is most influenced by the viscous effects. John *et al.* [62] studied the ramp induced shock wave laminar boundary layer interaction in hypersonic flows and proposed that the ratio of the wall temperature to the freestream stagnation temperature is the critical value in this interaction, rather than the individual temperatures. Moreover, they showed suppression in the upstream influence by increase in the Mach number, which results in decrease in extent of the separation.

Although investigation of two-dimensional shock wave boundary layer interactions provides insight and a deeper understanding of the physics of this phenomena, encounter of three-dimensional interactions is highly more ubiquitous. A canonical configuration associated with three-dimensional shock wave boundary layer interaction is a blunt fin-plate junction. This configuration is a generic model that represents many geometric areas of high speed vehicles, such as wing-body, fin-wing and wing-pylon junctions. In an attempt to further study this three-dimensional shock wave boundary layer interaction, Houwing *et.al.* [63] experimentally investigated a laminar hypersonic separation at a fin-plate junction and visualized the separation point, the angle of the separation shock and the shock stand-off distance at the plane of symmetry, using Planar Laser-Induced Fluorescence (PLIF). They showed that there may exist some extent of unsteadiness in the separated region due to some perturbations caused by the flow separation at Reynolds numbers below the transitional value. However, the frequencies corresponding to these oscillations are well below the fluctuations of a fully turbulent case.

Additionally, an experimental investigation of a separation induced by a blunt fin in a Mach 7.8 flow has been carried out using oil flow visualization with measurements of wall pressure and heat transfer by Wang *et.al* [64]. In this research, two distinct regions of outer and inner domains have been categorized and it has been shown that the position and the shape of the separation in the inner region is determined mainly by the diameter of the fin, and outer flow properties depend mostly on the freestream

Mach number and the angle of the fin. In a separate research, Dolling [65] has experimentally studied the effect of bluntness of the fin on the shock wave turbulent boundary layer interaction in a Mach 3 flow with adiabatic wall temperature. He showed that there is a region at the vicinity of the fin, where the leading edge diameter affects the flow parameters, and outside this "leading-edge dominated" region, the flow field is independent of the leading edge bluntness.

In a separate numerical study, Dolling and Bogdonoff [66] investigated on a blunt fin-plate junction and showed that the most dominant parameters on the shock wave boundary layer interaction in this configuration are the diameter of the fin and the sweep angle of the fin relative to the plate. They further studied the spanwise and vertical development of the interaction at a Mach 3 incoming flow with a turbulent boundary layer. Moreover, in investigation by Hung and Buning [67], shock wave boundary layer interaction induced by a blunt fin in a flow with freestream Mach number 2.95 was numerically simulated. By studying different boundary layer thickness of the incoming flow, they showed that the size of the horseshoe vortex and the spatial extent of the interaction are dominated by inviscid flow and only weakly dependent on the Reynolds number. The shock wave boundary layer interaction at a fin-plate junction is highly three-dimensional; therefore, unlike a two-dimensional interaction, there exists an additional direction for the fluid to escape the adverse pressure gradient. As a result, for a three-dimensional interaction, the boundary layer thickness is not the dominant factor to affect the extent of the separation and the size of the horseshoe vortex.

Two separate experiments conducted by Chanetz [68] and Hiers *et al.* [69] are chosen for simulation in this PhD dissertation. These experiments investigate the shock wave laminar boundary layer interaction in two different geometries. The geometry used in Chanetz's experiment is a hollow cylinder flare, which creates an axisymmetric flow with an Edney type IV interaction. The experiment conducted by Hiers *et al.* studies a three dimensional flow over a fin mounted on a flat plate. An MPI code written in C++ language, developed in part by the author, is used to numerically simulate these experiments. The results of the numerical calculations of the simulation of the Chanetz's experiment is used for validation of the MPI code which is later used to simulate the experiment conducted by Hiers *et al.*.

The objective of this PhD dissertation is the assessment of the capability of the prediction of aerothermodynamic loads in a compressible flow using Euler or Navier-Stokes equations assuming perfect gas. Two major types of the compressible phenomena have been chosen to investigate: flow control and drag reduction in supersonic flows, and shock wave laminar boundary layer interactions in hypersonic flows. Numerical calculations -both using a commercial code and an MPI code developed in part by the author- are performed and the numerical results are compared with experiments for validation.

Chapter 2

Methodology

2.1 Governing Equations

There are two models used in this Ph.D. dissertation: inviscid perfect gas and viscous laminar perfect gas models. Unsteady Euler and unsteady Navier-Stokes equations coupled with the Ideal Gas Equation are solved for the first and second models, respectively. The difference between these two models is that in the unsteady Navier-Stokes equations the viscous fluxes are considered in addition to the inviscid fluxes. On the other hand, the viscous fluxes -which take account the viscous and thermal diffusion- are neglected in the Euler equations used in the inviscid perfect gas model. The unsteady Navier-Stokes equations, which are the equations for the conservation of mass, momentum and energy in the laminar viscous model coupled by the Ideal Gas Equation are presented in Equations 2.1 to 2.6.

$$\partial\rho/\partial t + \nabla\cdot(\rho\mathbf{u}) = 0 \tag{2.1}$$

$$\partial(\rho\mathbf{u})/\partial t + \nabla\cdot(\mathbf{u}\otimes(\rho\mathbf{u})) + \nabla p - \nabla\cdot\underline{\underline{\tau}} = 0 \tag{2.2}$$

$$\partial(\rho e)/\partial t + \nabla\cdot(\mathbf{u}(\rho e + p)) - \nabla\cdot(\underline{\underline{\tau}}\mathbf{u}) - \nabla\cdot(k\nabla T) = 0 \tag{2.3}$$

$$p - \rho RT = 0 \tag{2.4}$$

where $\otimes$ is the outer product, (e) is the total energy per unit mass and ($\underline{\underline{\tau}}$) is the stress tensor defined as follows

$$\underline{\underline{\tau}} = -\frac{2}{3}\mu\nabla\cdot\mathbf{u}\underline{\underline{I}} + \mu(\nabla\mathbf{u} + (\nabla\mathbf{u})^T) \tag{2.5}$$

$$e = c_v T + \frac{1}{2}\mathbf{u}\cdot\mathbf{u} \tag{2.6}$$

The unsteady Euler equations are the mathematical description of the conservation of mass, momentum and energy, neglecting the viscous and thermal diffusion. Equations

2.7 to 2.10 present the Euler equations as well as the Ideal Gas Equation used to solve for the inviscid perfect gas model. The last term in the momentum equation (Equation 2.2) and the last two terms in the energy equation (Equation 2.3) implement the viscous diffusion effects in the Navier-Stokes equations and are omitted in the Euler equations. In addition, the last term in the energy equation (Equation 2.3) implements the effects of thermal diffusion and it does not appear in the Euler equations as well.

$$\partial\rho/\partial t + \nabla \cdot (\rho\mathbf{u}) = 0 \tag{2.7}$$

$$\partial(\rho\mathbf{u})/\partial t + \nabla \cdot (\mathbf{u} \otimes (\rho\mathbf{u})) + \nabla p = 0 \tag{2.8}$$

$$\partial(\rho e)/\partial t + \nabla \cdot (\mathbf{u}(\rho e + p)) = 0 \tag{2.9}$$

$$p - \rho RT = 0 \tag{2.10}$$

The further assumptions used in both of the above models are first of all that the fluid is calorically perfect, *i.e.,* the specific heats are constant. Moreover, radiation effects and chemical reactions are omitted and the fluid is assumed to be homogeneous with uniform molecular composition [70].

2.2 Numerical Algorithm

2.2.1 Finite Volume Method

The equations for the conservation of mass, momentum and energy described in section 2.1 can be written in a matrix format presented in Equation 2.11. Arbitrary control volumes -which are the computational cells in the computational domain- are considered and the partial differential equations introduced in Equation 2.11 are integrated in the control volume V with boundary surface ∂V. The divergence terms are converted to surface integrals, using the divergence theorem. In the integral format of the equations the Navier-Stokes equations, which are the more general format compared with the Euler equations are being described. The integral form of the equations in a matrix structure is presented in Equation 2.12.

$$\frac{\partial \mathcal{Q}}{\partial t} + \frac{\partial \mathcal{F}}{\partial x} + \frac{\partial \mathcal{G}}{\partial y} + \frac{\partial \mathcal{H}}{\partial z} + \frac{\partial \mathcal{R}}{\partial x} + \frac{\partial \mathcal{S}}{\partial y} + \frac{\partial \mathcal{T}}{\partial z} = 0 \tag{2.11}$$

$$\frac{d}{dt}\int_V \mathcal{Q}dV + \int_{\partial V}(\mathcal{F}\hat{i} + \mathcal{G}\hat{j} + \mathcal{H}\hat{k}) \cdot \hat{n}dA + \int_{\partial V}(\mathcal{R}\hat{i} + \mathcal{S}\hat{j} + \mathcal{T}\hat{k}) \cdot \hat{n}dA = 0 \tag{2.12}$$

where

$$\mathcal{Q} = \begin{Bmatrix} \rho \\ \rho u \\ \rho v \\ \rho w \\ \rho e \end{Bmatrix}, \quad \mathcal{F} = \begin{Bmatrix} \rho u \\ \rho u^2 + p \\ \rho v u \\ \rho w u \\ u(\rho e + p) \end{Bmatrix}, \quad \mathcal{G} = \begin{Bmatrix} \rho v \\ \rho u v \\ \rho v^2 + p \\ \rho w v \\ v(\rho e + p) \end{Bmatrix} \tag{2.13}$$

$$\mathcal{H} = \begin{Bmatrix} \rho w \\ \rho u w \\ \rho v w \\ \rho w^2 + p \\ w(\rho e + p) \end{Bmatrix}, \quad \mathcal{R} = -\begin{Bmatrix} 0 \\ \tau_{xx} \\ \tau_{xy} \\ \tau_{xz} \\ q_x + \tau_{xx}u + \tau_{xy}v + \tau_{xz}w \end{Bmatrix} \tag{2.14}$$

$$\mathcal{S} = -\begin{Bmatrix} 0 \\ \tau_{xy} \\ \tau_{yy} \\ \tau_{yz} \\ q_y + \tau_{xy}u + \tau_{yy}v + \tau_{yz}w \end{Bmatrix}, \quad \mathcal{T} = -\begin{Bmatrix} 0 \\ \tau_{xz} \\ \tau_{yz} \\ \tau_{zz} \\ q_z + \tau_{xz}u + \tau_{yz}v + \tau_{zz}w \end{Bmatrix} \tag{2.15}$$

The first term in Equation 2.12 is the integration over time for the flow parameters that are being updated for the next step in time (ρ, ρu, ρv, ρw and ρe). vector $\mathcal{Q}$ contains all the five flow parameters in each control volume that are sufficient to obtain all other information of the flow in that cell. These values are saved in the cell center and they are the cell-average values. Moreover, in the finite volume approach inviscid and viscous fluxes are calculated at each surface of each cell. The contribution of the inviscid fluxes are presented in the second integration in Equation 2.12 with the vectors $\mathcal{F}$, $\mathcal{G}$ and $\mathcal{H}$. The contribution of the viscous fluxes are accounted in the third integration in Equation 2.12 with vectors $\mathcal{R}$, $\mathcal{S}$ and $\mathcal{T}$. In the Euler equations, the Equation 2.12 is simplified to only the first two integrations.

In a general computational domain with arbitrary shapes of the control volumes the coordinates of the cells and their edges are going to be described with a set of variables named as $\xi(x,y,z)$, $\eta(x,y,z)$ and $\zeta(x,y,z)$. Using these variables, we can identify the unit vectors normal and tangent to each surface of each control volume. As a result, the fluxes at each surface of each cell can be calculated knowing the defining vectors of each surface. To convert the Equation 2.11 to an equation based on the $\xi(x,y,z)$, $\eta(x,y,z)$ and $\zeta(x,y,z)$ coordinates, we can use the chain rule as follows.

$$\begin{aligned}
&\frac{\partial \mathcal{Q}}{\partial t}+\frac{\partial \mathcal{F}}{\partial \xi}\frac{\partial \xi}{\partial x}+\frac{\partial \mathcal{F}}{\partial \eta}\frac{\partial \eta}{\partial x}+\frac{\partial \mathcal{F}}{\partial \zeta}\frac{\partial \zeta}{\partial x}+\frac{\partial \mathcal{G}}{\partial \xi}\frac{\partial \xi}{\partial y}+\frac{\partial \mathcal{G}}{\partial \eta}\frac{\partial \eta}{\partial y}+\frac{\partial \mathcal{G}}{\partial \zeta}\frac{\partial \zeta}{\partial y}+\frac{\partial \mathcal{H}}{\partial \xi}\frac{\partial \xi}{\partial z}+\\
&\frac{\partial \mathcal{H}}{\partial \eta}\frac{\partial \eta}{\partial z}+\frac{\partial \mathcal{H}}{\partial \zeta}\frac{\partial \zeta}{\partial z}+\frac{\partial \mathcal{R}}{\partial \xi}\frac{\partial \xi}{\partial x}+\frac{\partial \mathcal{R}}{\partial \eta}\frac{\partial \eta}{\partial x}+\frac{\partial \mathcal{R}}{\partial \zeta}\frac{\partial \zeta}{\partial x}+\frac{\partial \mathcal{S}}{\partial \xi}\frac{\partial \xi}{\partial y}+\frac{\partial \mathcal{S}}{\partial \eta}\frac{\partial \eta}{\partial y}+\frac{\partial \mathcal{S}}{\partial \zeta}\frac{\partial \zeta}{\partial y}\\
&+\frac{\partial \mathcal{T}}{\partial \xi}\frac{\partial \xi}{\partial z}+\frac{\partial \mathcal{T}}{\partial \eta}\frac{\partial \eta}{\partial z}+\frac{\partial \mathcal{T}}{\partial \zeta}\frac{\partial \zeta}{\partial z}=0
\end{aligned} \tag{2.16}$$

After some further algebraic simplifications we get to a set of equations in the $\xi(x,y,z)$, $\eta(x,y,z)$ and $\zeta(x,y,z)$ coordinates as presented in Equation 2.17. The vectors in this equation are functions of the variables in both sets of system of coordinates and the Jacobian matrix is defined as $\partial(\xi,\eta,\zeta)/\partial(x,y,z)$ with its determinate labeled as J. We can rewrite the equation with new vectors labeled by a prime notation as follows.

$$\frac{\partial \mathcal{Q}'}{\partial t}+\frac{\partial \mathcal{F}'}{\partial \xi}+\frac{\partial \mathcal{G}'}{\partial \eta}+\frac{\partial \mathcal{H}'}{\partial \zeta}+\frac{\partial \mathcal{R}'}{\partial \xi}+\frac{\partial \mathcal{S}'}{\partial \eta}+\frac{\partial \mathcal{T}'}{\partial \zeta}=0 \tag{2.17}$$

The equations are then multiplied to $d\xi d\eta d\zeta$ and integrated. Note that in these equations $d\xi = d\eta = d\zeta = 1$. The set of final equations is presented in Equation 2.18. In these equations i, j and k are the counters of the cell in the ξ, η and ζ directions, respectively. $\mathcal{Q}_{ijk}$ is the vector presented in Equation 2.13, which consists of the key variables in the cell ijk and the notation of ν_{ijk} is assigned for the volume of the cell ijk. For simplicity, from this point on, the notation prime is dropped from the vectors. The subtractions $(\mathcal{F}_{i+\frac{1}{2}}-\mathcal{F}_{i-\frac{1}{2}})$ and $(\mathcal{R}_{i+\frac{1}{2}}-\mathcal{R}_{i-\frac{1}{2}})$ represents the net inviscid and viscous fluxes in the ξ direction, respectively. The subtractions $(\mathcal{G}_{j+\frac{1}{2}}-\mathcal{G}_{j-\frac{1}{2}})$ and $(\mathcal{S}_{j+\frac{1}{2}}-\mathcal{S}_{j-\frac{1}{2}})$ represents the net inviscid and viscous fluxes in the η direction, respectively. The subtractions $(\mathcal{H}_{k+\frac{1}{2}}-\mathcal{H}_{k-\frac{1}{2}})$ and $(\mathcal{T}_{k+\frac{1}{2}}-\mathcal{T}_{k-\frac{1}{2}})$ represents the net inviscid and viscous fluxes in the ζ direction, respectively. I should again emphasize that except for the vector $\mathcal{Q}$, the vectors introduced in Equations 2.18 through 2.21

are not the same as the vectors presented in Equation 2.11. The same notation has been chosen for simplicity. More detailed description of the vectors are presented in Equations 2.19 through 2.21.

$$\frac{d}{dt}(\mathcal{Q}_{ijk}\nu_{ijk}) + (\mathcal{F}_{i+\frac{1}{2}} - \mathcal{F}_{i-\frac{1}{2}}) + (\mathcal{G}_{j+\frac{1}{2}} - \mathcal{G}_{j-\frac{1}{2}}) + (\mathcal{H}_{k+\frac{1}{2}} - \mathcal{H}_{k-\frac{1}{2}}) + (\mathcal{R}_{i+\frac{1}{2}} - \mathcal{R}_{i-\frac{1}{2}})$$
$$+ (\mathcal{S}_{j+\frac{1}{2}} - \mathcal{S}_{j-\frac{1}{2}}) + (\mathcal{T}_{k+\frac{1}{2}} - \mathcal{T}_{k-\frac{1}{2}}) = 0 \tag{2.18}$$

$$\mathcal{F} = \begin{Bmatrix} \rho U \\ \rho u U + l'_x p \\ \rho v U + l'_y p \\ \rho w U + l'_z p \\ U(\rho e + p) \end{Bmatrix}, \quad \mathcal{G} = \begin{Bmatrix} \rho V \\ \rho u V + m'_x p \\ \rho v V + m'_y p \\ \rho w V + m'_z p \\ V(\rho e + p) \end{Bmatrix}, \quad \mathcal{H} = \begin{Bmatrix} \rho W \\ \rho u W + n'_x p \\ \rho v W + n'_y p \\ \rho w W + n'_z p \\ W(\rho e + p) \end{Bmatrix} \tag{2.19}$$

$$\mathcal{R} = -\begin{Bmatrix} 0 \\ l'_x\tau_{xx} + l'_y\tau_{xy} + l'_z\tau_{xz} \\ l'_x\tau_{xy} + l'_y\tau_{yy} + l'_z\tau_{yz} \\ l'_x\tau_{xz} + l'_y\tau_{yz} + l'_z\tau_{zz} \\ l'_x\beta_x + l'_y\beta_y + l'_z\beta_z \end{Bmatrix}, \quad \mathcal{S} = -\begin{Bmatrix} 0 \\ m'_x\tau_{xx} + m'_y\tau_{xy} + m'_z\tau_{xz} \\ m'_x\tau_{xy} + m'_y\tau_{yy} + m'_z\tau_{yz} \\ m'_x\tau_{xz} + m'_y\tau_{yz} + m'_z\tau_{zz} \\ m'_x\beta_x + m'_y\beta_y + m'_z\beta_z \end{Bmatrix}, \tag{2.20}$$

$$\mathcal{T} = -\begin{Bmatrix} 0 \\ n'_x\tau_{xx} + n'_y\tau_{xy} + n'_z\tau_{xz} \\ n'_x\tau_{xy} + n'_y\tau_{yy} + n'_z\tau_{yz} \\ n'_x\tau_{xz} + n'_y\tau_{yz} + n'_z\tau_{zz} \\ n'_x\beta_x + n'_y\beta_y + n'_z\beta_z \end{Bmatrix} \tag{2.21}$$

where

$$\vec{l'} = \frac{\vec{\nabla}\xi}{J}d\eta d\zeta \tag{2.22}$$
$$\vec{m'} = \frac{\vec{\nabla}\eta}{J}d\xi d\zeta \tag{2.23}$$
$$\vec{n'} = \frac{\vec{\nabla}\zeta}{J}d\xi d\eta \tag{2.24}$$

$\vec{l'}$ is defined the normal to the face vector in ξ direction with its magnitude equal to the area of cell surface in ξ direction. The analogous definition can be made for $\vec{m'}$ and $\vec{n'}$ in η and ζ directions, respectively. The capital letters U, V and W are proportional to the velocities in ξ, η and ζ directions, respectively and they are defined in Equations 2.25 through 2.27. In these equations $\vec{V}$ represents the three dimensional velocity vector.

$$U = (\xi_x u + \xi_y v + \xi_z w) d\eta d\zeta / J = \vec{V} \cdot \vec{l'} \tag{2.25}$$

$$V = (\eta_x u + \eta_y v + \eta_z w) d\xi d\zeta / J = \vec{V} \cdot \vec{m'} \tag{2.26}$$

$$W = (\zeta_x u + \zeta_y v + \zeta_z w) d\xi d\eta / J = \vec{V} \cdot \vec{n'} \tag{2.27}$$

and

$$\beta_x = q_x + \tau_{xx} u + \tau_{xy} v + \tau_{xz} w \tag{2.28}$$

$$\beta_y = q_y + \tau_{xy} u + \tau_{yy} v + \tau_{yz} w \tag{2.29}$$

$$\beta_z = q_z + \tau_{xz} u + \tau_{yz} v + \tau_{zz} w \tag{2.30}$$

where

$$\tau_{xx} = \mu J[\frac{4}{3}(u_\xi l'_x + u_\eta m'_x + u_\zeta n'_x) - \frac{2}{3}(v_\xi l'_y + v_\eta m'_y + v_\zeta n'_y + w_\xi l'_z + w_\eta m'_z + w_\zeta n'_z)] \tag{2.31}$$

$$\tau_{xy} = \mu J[u_\xi l'_y + u_\eta m'_y + u_\zeta n'_y + v_\xi l'_x + v_\eta m'_x + v_\zeta n'_x] \tag{2.32}$$

$$\tau_{xz} = \mu J[u_\xi l'_z + u_\eta m'_z + u_\zeta n'_z + w_\xi l'_x + w_\eta m'_x + w_\zeta n'_x] \tag{2.33}$$

$$\tau_{yy} = \mu J[\frac{4}{3}(v_\xi l'_y + v_\eta m'_y + v_\zeta n'_y) - \frac{2}{3}(u_\xi l'_x + u_\eta m'_x + u_\zeta n'_x + w_\xi l'_z + w_\eta m'_z + w_\zeta n'_z)] \tag{2.34}$$

$$\tau_{yz} = \mu J[v_\xi l'_z + v_\eta m'_z + v_\zeta n'_z + w_\xi l'_y + w_\eta m'_y + w_\zeta n'_y] \tag{2.35}$$

$$\tau_{zz} = \mu J[\frac{4}{3}(w_\xi l'_z + w_\eta m'_z + w_\zeta n'_z) - \frac{2}{3}(u_\xi l'_x + u_\eta m'_x + u_\zeta n'_x + v_\xi l'_y + v_\eta m'_y + v_\zeta n'_y)] \tag{2.36}$$

and

$$q_x = kJ(T_\xi l'_x + T_\eta m'_x + T_\zeta n'_x) \tag{2.37}$$

$$q_y = kJ(T_\xi l'_y + T_\eta m'_y + T_\zeta n'_y) \tag{2.38}$$

$$q_z = kJ(T_\xi l'_z + T_\eta m'_z + T_\zeta n'_z) \tag{2.39}$$

The viscosity is calculated using the Sutherland's law described in the the Equation 2.40, where $S = 110.4^0$ K and μ_{ref} and T_{ref} are reference viscosity and temperature calculated at some reference point.

$$\mu = \mu_{ref}(\frac{T}{T_{ref}})^{\frac{3}{2}}(\frac{T_{ref} + S}{T + S}) \tag{2.40}$$

At the end, we have a powerful and simple equation (Equation 2.18), which we need to proceed to solve. In order to solve this set of equations, we need to calculate the inviscid and viscous fluxes at each surface. After calculation of the fluxes, the equations should be integrated in time to solve for the variables in the next time step. This is the finite volume approach used in this Ph.D. dissertation.

2.2.2 Inviscid Fluxes

The inviscid fluxes contain nonlinear terms, making their calculations more challenging compared with the viscous fluxes. Shock capturing methods have been used in calculation of the inviscid fluxes to allow obtaining physical features such as shock and expansion waves more feasible in a coarser grid spacing. To discuss the methods used in the calculation of the inviscid fluxes, the one dimensional Euler equations will be analyzed. For the three-dimensional case used in this Ph.D. dissertation, the same concept has been used. One dimensional Euler equations can be written in vector format as follows.

$$\frac{\partial \mathcal{Q}}{\partial t} + \frac{\partial \mathcal{F}}{\partial x} = 0 \tag{2.41}$$

where

$$\mathcal{Q} = \begin{Bmatrix} \rho \\ \rho u \\ \rho e \end{Bmatrix}, \quad \mathcal{F} = \begin{Bmatrix} \rho u \\ \rho u u + p \\ \rho e u + p u \end{Bmatrix} \tag{2.42}$$

We can further write

$$\frac{\partial \mathcal{Q}}{\partial t} + \mathcal{A}\frac{\partial \mathcal{Q}}{\partial x} = 0 \tag{2.43}$$

where the matrix $\mathcal{A}$ is the Jacobian matrix defined as follows.

$$\mathcal{A} = \frac{\partial \mathcal{F}}{\partial \mathcal{Q}} = \begin{Bmatrix} 0 & 1 & 0 \\ \frac{(\gamma-3)}{2}u^2 & (3-\gamma)u & (\gamma-1) \\ \frac{(\gamma-1)}{2}u^3 - Hu & H-(\gamma-1)u^2 & \gamma u \end{Bmatrix} \tag{2.44}$$

where H is the total enthalpy per unit mass defined by $H = c_p T + \frac{1}{2}u^2$. The semi-discrete form of the Equation 2.41 is presented in Equation 2.45 and the evaluation of the inviscid fluxes ($\mathcal{F}_{i+\frac{1}{2}}$ and $\mathcal{F}_{i-\frac{1}{2}}$) are discussed in this section.

$$\frac{d\mathcal{Q}_i}{dt} + \frac{(\mathcal{F}_{i+\frac{1}{2}} - \mathcal{F}_{i-\frac{1}{2}})}{\Delta x} = 0 \tag{2.45}$$

Roe's Method

Roe's method [71],[72] proposes the exact solution to an approximation of the generalized Riemann problem. Each surface of a cell is treated as the generalized Riemann problem with left and right states at $\mathcal{Q}_r$ and $\mathcal{Q}_l$ as presented in Figure 2.1. The inviscid fluxes are then calculated at the surfaces of each cell with a method proposed using the concept of the generalized Riemann problem. The approximated format of the Euler equation used in Roe's method in presented in Equation 2.46.

$$\frac{\partial \mathcal{Q}}{\partial t} + \tilde{\mathcal{A}}(\mathcal{Q}_r, \mathcal{Q}_l)\frac{\partial \mathcal{Q}}{\partial x} = 0 \tag{2.46}$$

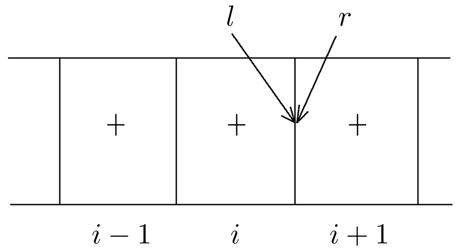

Figure 2.1: Schematics of the Left and Right Sides of the Cell Surfaces

The matrix $\tilde{\mathcal{A}}(\mathcal{Q}_r, \mathcal{Q}_l)$ is the *Roe matrix*, defined in the Equation 2.47 and the quantities $\tilde{u}$ and $\tilde{H}$ defined in Equations 2.48 are the *Roe-averaged velocity* and *Roe-averaged total enthalpy, respectively.*

$$\tilde{\mathcal{A}} = \left\{ \begin{array}{ccc} 0 & 1 & 0 \\ \frac{(\gamma-3)}{2}\tilde{u}^2 & (3-\gamma)\tilde{u} & (\gamma-1) \\ \frac{(\gamma-1)}{2}\tilde{u}^3 - \tilde{H}\tilde{u} & \tilde{H} - (\gamma-1)\tilde{u}^2 & \gamma\tilde{u} \end{array} \right\} \tag{2.47}$$

$$\tilde{u} = \frac{\sqrt{\rho_l}u_l + \sqrt{\rho_r}u_r}{\sqrt{\rho_l} + \sqrt{\rho_r}}, \quad \tilde{H} = \frac{\sqrt{\rho_l}H_l + \sqrt{\rho_r}H_r}{\sqrt{\rho_l} + \sqrt{\rho_r}} \tag{2.48}$$

The matrix $\tilde{\mathcal{A}}(\mathcal{Q}_r, \mathcal{Q}_l)$ is diagonalizable with real and distinct eigenvalues and linearly independent eigenvectors. The Roe matrix can be diagonalized as follows.

$$\tilde{\mathcal{A}}(\mathcal{Q}_r, \mathcal{Q}_l) = \tilde{S}\tilde{\Lambda}\tilde{S}^{-1} \tag{2.49}$$

where

$$\tilde{S} = \left\{ \begin{array}{ccc} 1 & 1 & 1 \\ \tilde{u} & \tilde{u} + \tilde{a} & \tilde{u} - \tilde{a} \\ \frac{1}{2}\tilde{u}^2 & \tilde{H} + \tilde{u}\tilde{a} & \tilde{H} - \tilde{u}\tilde{a} \end{array} \right\} \tag{2.50}$$

$$\tilde{S}^{-1} = \left\{ \begin{array}{ccc} 1 - (\gamma-1)\tilde{u}^2/2\tilde{a}^2 & (\gamma-1)\tilde{u}/\tilde{a}^2 & -(\gamma-1)/\tilde{a}^2 \\ (\gamma-1)\tilde{u}^2/4\tilde{a}^2 - \tilde{u}/2\tilde{a} & -(\gamma-1)\tilde{u}/2\tilde{a}^2 + 1/2\tilde{a} & (\gamma-1)/2\tilde{a}^2 \\ (\gamma-1)\tilde{u}^2/4\tilde{a}^2 + \tilde{u}/2\tilde{a} & -(\gamma-1)\tilde{u}/2\tilde{a}^2 - 1/2\tilde{a} & (\gamma-1)/2\tilde{a}^2 \end{array} \right\} \tag{2.51}$$

$$\tilde{\Lambda} \equiv \left\{ \begin{array}{ccc} \tilde{\lambda}_1 & 0 & 0 \\ 0 & \tilde{\lambda}_2 & 0 \\ 0 & 0 & \tilde{\lambda}_3 \end{array} \right\} \tag{2.52}$$

The $\tilde{\lambda}_i$ are eigenvalues of the Roe matrix, where $\tilde{\lambda}_1 = \tilde{u}$, $\tilde{\lambda}_2 = \tilde{u} + \tilde{a}$ and $\tilde{\lambda}_3 = \tilde{u} - \tilde{a}$. $\tilde{S}$ is the matrix of right eigenvectors of the matrix $\tilde{\mathcal{A}}$, and with the assumption of a constant $\tilde{\mathcal{A}}(\mathcal{Q}_r, \mathcal{Q}_l)$ we can write

$$\frac{\partial R}{\partial t} + \tilde{\Lambda}\frac{\partial R}{\partial x} = 0 \tag{2.53}$$

where

$$R \equiv \tilde{S}^{-1}\mathcal{Q} = \begin{Bmatrix} R_1 \\ R_2 \\ R_3 \end{Bmatrix} \tag{2.54}$$

The exact solution of the Equation 2.53 -which is an approximation to the Euler equation- is as follows. R_1 is constant on the curve defined by $\frac{dx}{dt} = \tilde{\lambda}_1 = \tilde{u}$, R_2 is constant on the curve defined by $\frac{dx}{dt} = \tilde{\lambda}_2 = \tilde{u} + \tilde{a}$, and finally, R_3 is constant on the curve defined by $\frac{dx}{dt} = \tilde{\lambda}_3 = \tilde{u} - \tilde{a}$. The curves introduced above are the characteristic curves of the Equation 2.53.

The Equation 2.41 can be discretized in the spatial coordinate as follows.

$$\frac{d\mathcal{Q}_i}{dt} + \frac{(\mathcal{F}_{i+\frac{1}{2}} - \mathcal{F}_{i-\frac{1}{2}})}{\Delta x} = 0 \tag{2.55}$$

The inviscid flux $\mathcal{F}_{i+\frac{1}{2}}$ can be calculated below.

$$\mathcal{F}_{i+\frac{1}{2}} = \tilde{\mathcal{A}}\mathcal{Q} = (\tilde{S}\tilde{\Lambda}\tilde{S}^{-1})(\tilde{S}R)_{i+\frac{1}{2}} = \tilde{S}\tilde{\Lambda}R_{i+\frac{1}{2}} \tag{2.56}$$

Using the solution obtained for the Equation 2.53 and some further algebraic procedures we get to the Equation 2.57, which is the equation used in the Roe's method to calculate the inviscid flux at the surface $i + \frac{1}{2}$.

$$\mathcal{F}_{i+\frac{1}{2}} = \frac{1}{2}[F_l + F_r + \tilde{S}|\tilde{\Lambda}|\tilde{S}^{-1}(\mathcal{Q}^l_{i+\frac{1}{2}} - \mathcal{Q}^r_{i+\frac{1}{2}})] \tag{2.57}$$

Van Leer's Method

The Van Leer's method [73] is a flux splitting method based on the Mach number. The flux vector presented in Equation 2.42 can be rewritten as follows.

$$\mathcal{F} = \left\{ \begin{array}{c} \rho a M \\ \frac{\rho a^2}{\gamma}(\gamma M^2 + 1) \\ \rho a^3 M[\frac{1}{(\gamma-1)} + \frac{1}{2}M^2] \end{array} \right\} \tag{2.58}$$

The terms involving the Mach number is then split into two parts and the average Mach number M is calculated using the left and right properties (Equation 2.72). The mass, momentum and energy fluxes can be further evaluated by a split method chosen by Van Leer as follows.

$$\rho u = \rho_l a_l M^+ + \rho_r a_r M^- \tag{2.59}$$

$$\rho u^2 + p = \frac{\rho_l a_l^2}{\gamma}(\gamma M^2 + 1)^+ + \frac{\rho_r a_r^2}{\gamma}(\gamma M^2 + 1)^- \tag{2.60}$$

$$(\rho e + p)u = \rho_l a_l^3 M[(\gamma - 1)^{-1} + \frac{1}{2}M^2]^+ + \rho_r a_r^3 M[(\gamma - 1)^{-1} + \frac{1}{2}M^2]^- \tag{2.61}$$

where

$$M^+ = \begin{cases} 0 & \text{for } M \leq -1 \\ f_1^+ & \text{for } -1 \leq M \leq 1 \\ M & \text{for } M \geq 1 \end{cases}, \quad M^- = \begin{cases} M & \text{for } M \leq -1 \\ f_1^- & \text{for } -1 \leq M \leq 1 \\ 0 & \text{for } M \geq 1 \end{cases} \tag{2.62}$$

$$(\gamma M^2 + 1)^+ = \begin{cases} 0 & \text{for } M \leq -1 \\ f_2^+ & \text{for } -1 \leq M \leq 1 \\ \gamma M^2 + 1 & \text{for } M \geq 1 \end{cases}, \tag{2.63}$$

$$(\gamma M^2 + 1)^- = \begin{cases} \gamma M^2 + 1 & \text{for } M \leq -1 \\ f_2^- & \text{for } -1 \leq M \leq 1 \\ 0 & \text{for } M \geq 1 \end{cases} \tag{2.64}$$

$$M[(\gamma-1)^{-1}+\frac{1}{2}M^2]^+ = \begin{cases} 0 & \text{for } M \le -1 \\ f_3^+ & \text{for } -1 \le M \le 1 \\ M[(\gamma-1)^{-1}+\frac{1}{2}M^2] & \text{for } M \ge 1 \end{cases}, \tag{2.65}$$

$$M[(\gamma-1)^{-1}+\frac{1}{2}M^2]^- = \begin{cases} M[(\gamma-1)^{-1}+\frac{1}{2}M^2] & \text{for } M \le -1 \\ f_3^- & \text{for } -1 \le M \le 1 \\ 0 & \text{for } M \ge 1 \end{cases} \tag{2.66}$$

where

$$f_1^+ = \frac{1}{4}(M+1)^2, \quad f_1^- = -\frac{1}{4}(M-1)^2 \tag{2.67}$$

$$f_2^+ = \frac{1}{4}(M+1)^2[(\gamma-1)M+2] \tag{2.68}$$

$$f_2^- = -\frac{1}{4}(M-1)^2[(\gamma-1)M-2] \tag{2.69}$$

$$f_3^+ = \frac{1}{8}(\gamma+1)^{-1}(\gamma-1)^{-1}(M+1)^2[(\gamma-1)M+2]^2 \tag{2.70}$$

$$f_3^- = -\frac{1}{8}(\gamma+1)^{-1}(\gamma-1)^{-1}(M-1)^2[(\gamma-1)M-2]^2 \tag{2.71}$$

and

$$M = \frac{u_l+u_r}{a_l+a_r} \tag{2.72}$$

Using the Equations 2.59 to 2.72 we can calculate the mass, momentum and energy fluxes as follows.

$$\rho u = \begin{cases} \rho_r a_r M & \text{for } M \le -1 \\ \rho_l a_l f_1^+ + \rho_r a_r f_1^- & \text{for } -1 \le M \le 1 \\ \rho_l a_l M & \text{for } M \ge 1 \end{cases} \tag{2.73}$$

$$\rho u^2 + p = \begin{cases} \frac{\rho_r a_r^2}{\gamma}(\gamma M^2+1) & \text{for } M \le -1 \\ \frac{\rho_r a_r^2}{\gamma} f_2^+ + \frac{\rho_r a_r^2}{\gamma} f_2^- & \text{for } -1 \le M \le 1 \\ \frac{\rho_l a_l^2}{\gamma}(\gamma M^2+1) & \text{for } M \ge 1 \end{cases} \tag{2.74}$$

$$\rho e u + p u = \begin{cases} \rho_r a_r^3 M[(\gamma-1)^{-1} + \frac{1}{2}M^2] & \text{for } M \leq -1 \\ \rho_l a_l^3 f_3^+ + \rho_r a_r^3 f_3^+ & \text{for } -1 \leq M \leq 1 \\ \rho_l a_l^3 M[(\gamma-1)^{-1} + \frac{1}{2}M^2] & \text{for } M \geq 1 \end{cases} \tag{2.75}$$

2.2.3 Reconstruction

As it was discussed in the section 2.2.2, the inviscid fluxes are calculated knowing the left and right properties at the surface of the cell ($\mathcal{Q}_l$ and $\mathcal{Q}_r$). However, in the finite volume method the flow variables are stored and evaluated at the cell centers, not on the left and right sides of each cell surfaces. The values stored at the center of the cells are the cell averaged values. The role of the reconstruction is to calculate the flow properties at left and right sides of the cell surfaces ($\mathcal{Q}_l$ and $\mathcal{Q}_r$) using the cell averaged values of the neighboring cells in order to calculate the inviscid fluxes.

I should add that the choice of the discretization in space has a crucial role in stability of the code. A stable code is the one which does not produce exponentially growing solutions that are physically implausible; on the other hand, an unstable code due to certain spatial discretization can potentially yield to exponentially growing and unphysical solutions. The spatial discretization must contain the physical domain of dependency in order to be stable. As a result, the flux algorithms should be strongly influenced by the flow physics in order to be useful.

First Order

A very simple approach to evaluate the variables at each surface of each cell is to simply assign $\mathcal{Q}_i(x) = \mathcal{Q}_i$. This actually assigns the cell averaged values of the adjacent cells to the left and right values at each surface (Equation 2.76). This approach is first order accurate leading to excessive numerical diffusion and it is not generally acceptable to use in numerical calculations. However, this reconstruction can be used to provide a better initial condition for further calculations with higher order accuracy.

$$\mathcal{Q}^r_{i+\frac{1}{2}} = \mathcal{Q}_{i+1}, \quad \mathcal{Q}^l_{i+\frac{1}{2}} = \mathcal{Q}_i \tag{2.76}$$

MUSCL

The MUSCL (*Modified Upwind Scheme for Conservation Laws*) algorithm [74], uses a polynomial function to obtain a second order accurate reconstruction on the surfaces of the cells, in order to estimate the values of $\mathcal{Q}$ on the left and right sides of the cell surfaces. A primitive function $I(x)$ is defined (Equation 2.77) and a unique third-order polynomial that interpolates the primitive function $I(x)$ is obtained using Newton's formula. From the derivative of the obtained third-order polynomial, the function $Q_i(x)$ can be calculated.

$$I(x) = \int_{x_{i-\frac{3}{4}}}^{x} \mathcal{Q} dx \qquad \text{for} \quad x_{i-\frac{3}{2}} \leq x \leq x_{i+\frac{3}{2}} \tag{2.77}$$

However, this approach assumes that the function $\mathcal{Q}$ is continuous, which is not the case for problems with shock waves or contact surfaces in gas dynamics. The reconstruction scheme can be modified in a way that a directional bias is used at the points of discontinuity. Although, since the exact function $\mathcal{Q}$ is unknown, recognition of discontinuous points are challenging. A simple approach to this problem would be to use a method in order to avoid formation of new local extrema relative to the cell averaged values of the adjacent cells. This approach is known as *No New Extrema (NNE)* and works as a limiter for the reconstruction scheme.

MUSCL is an abbreviation for Modified Upwind Scheme for Conservation Laws and a summery of the final equations used in this scheme for a non-uniform grid is as follows. No New Extrema approach has been used in this algorithm to avoid creating a new extrema at the surfaces of the cells.

$$\mathcal{Q}^l_{i+\frac{1}{2}} = \mathcal{Q}_i + \widehat{\Delta\mathcal{Q}_{i+\frac{1}{2}}}\kappa^l_{i+\frac{1}{2}} + \widehat{\Delta\mathcal{Q}_{i-\frac{1}{2}}}\kappa^l_{i-\frac{1}{2}} \tag{2.78}$$

$$\mathcal{Q}^r_{i-\frac{1}{2}} = \mathcal{Q}_i - \widehat{\Delta\mathcal{Q}_{i+\frac{1}{2}}}\kappa^r_{i+\frac{1}{2}} - \widehat{\Delta\mathcal{Q}_{i-\frac{1}{2}}}\kappa^r_{i-\frac{1}{2}} \tag{2.79}$$

where

$$\kappa^l_{i+\frac{1}{2}} = \frac{(\Delta x_i + \Delta x_{i-1})\Delta x_i}{(\Delta x_{i+1} + \Delta x_i)(\Delta x_{i+1} + \Delta x_i + \Delta x_{i-1})} \tag{2.80}$$

$$\kappa^l_{i-\frac{1}{2}} = \frac{\Delta x_{i+1}\Delta x_i}{(\Delta x_i + \Delta x_{i-1})(\Delta x_{i+1} + \Delta x_i + \Delta x_{i-1})} \tag{2.81}$$

$$\kappa^r_{i+\frac{1}{2}} = \frac{\Delta x_i \Delta x_{i-1}}{(\Delta x_{i+1} + \Delta x_i)(\Delta x_{i+1} + \Delta x_i + \Delta x_{i-1})} \tag{2.82}$$

$$\kappa^r_{i-\frac{1}{2}} = \frac{(\Delta x_i + \Delta x_{i+1})\Delta x_i}{(\Delta x_i + \Delta x_{i-1})(\Delta x_{i+1} + \Delta x_i + \Delta x_{i-1})} \tag{2.83}$$

The values $\widehat{\Delta\mathcal{Q}_{i+\frac{1}{2}}}$ and $\widehat{\Delta\mathcal{Q}_{i-\frac{1}{2}}}$ are chosen in a way so they create no new extrema in the reconstruction of the surface values. Four cases can be considered and different values for $\widehat{\Delta\mathcal{Q}_{i+\frac{1}{2}}}$ and $\widehat{\Delta\mathcal{Q}_{i-\frac{1}{2}}}$ are calculate that are within the limitations imposed by the No New Extrema condition. The condition for No New Extrema implies that

$$min(\mathcal{Q}_{i-1}, \mathcal{Q}_i, \mathcal{Q}_{i+1}) \leq \mathcal{Q}^l_{i+\frac{1}{2}} \leq max(\mathcal{Q}_{i-1}, \mathcal{Q}_i, \mathcal{Q}_{i+1}) \tag{2.84}$$

$$min(\mathcal{Q}_{i-1}, \mathcal{Q}_i, \mathcal{Q}_{i+1}) \leq \mathcal{Q}^r_{i-\frac{1}{2}} \leq max(\mathcal{Q}_{i-1}, \mathcal{Q}_i, \mathcal{Q}_{i+1}) \tag{2.85}$$

The four different possible cases are as follows.

case 1:

$$\Delta\mathcal{Q}_{i+\frac{1}{2}} = (\mathcal{Q}_{i+1} - \mathcal{Q}_i) \geq 0, \quad \Delta\mathcal{Q}_{i-\frac{1}{2}} = (\mathcal{Q}_i - \mathcal{Q}_{i-1}) \geq 0 \tag{2.86}$$

We have

$$\widehat{\Delta\mathcal{Q}_{i-\frac{1}{2}}} = min(\Delta\mathcal{Q}_{i-\frac{1}{2}}, (\frac{1-\kappa^l_{i+\frac{1}{2}}}{\kappa^l_{i-\frac{1}{2}}})\Delta\mathcal{Q}_{i+\frac{1}{2}}) \tag{2.87}$$

$$\widehat{\Delta\mathcal{Q}_{i+\frac{1}{2}}} = min(\Delta\mathcal{Q}_{i+\frac{1}{2}}, (\frac{1-\kappa^r_{i-\frac{1}{2}}}{\kappa^r_{i+\frac{1}{2}}})\Delta\mathcal{Q}_{i-\frac{1}{2}}) \tag{2.88}$$

case 2:

$$\Delta\mathcal{Q}_{i+\frac{1}{2}} \geq 0, \quad \Delta\mathcal{Q}_{i-\frac{1}{2}} \leq 0 \tag{2.89}$$

We have

$$\widehat{\Delta\mathcal{Q}_{i-\frac{1}{2}}} = max(\Delta\mathcal{Q}_{i-\frac{1}{2}}, \frac{\kappa^l_{i+\frac{1}{2}}}{\kappa^l_{i-\frac{1}{2}}}\Delta\mathcal{Q}_{i+\frac{1}{2}}) \tag{2.90}$$

$$\widehat{\Delta\mathcal{Q}_{i+\frac{1}{2}}} = min(\Delta\mathcal{Q}_{i+\frac{1}{2}}, -\frac{\kappa^r_{i-\frac{1}{2}}}{\kappa^r_{i+\frac{1}{2}}}\Delta\mathcal{Q}_{i-\frac{1}{2}}) \tag{2.91}$$

case 3:

$$\Delta\mathcal{Q}_{i+\frac{1}{2}} \leq 0, \quad \Delta\mathcal{Q}_{i-\frac{1}{2}} \geq 0 \tag{2.92}$$

We have

$$\widehat{\Delta\mathcal{Q}_{i-\frac{1}{2}}} = min(\Delta\mathcal{Q}_{i-\frac{1}{2}}, -\frac{\kappa^l_{i+\frac{1}{2}}}{\kappa^l_{i-\frac{1}{2}}}\Delta\mathcal{Q}_{i+\frac{1}{2}}) \tag{2.93}$$

$$\widehat{\Delta\mathcal{Q}_{i+\frac{1}{2}}} = max(\Delta\mathcal{Q}_{i+\frac{1}{2}}, -\frac{\kappa^r_{i-\frac{1}{2}}}{\kappa^r_{i+\frac{1}{2}}}\Delta\mathcal{Q}_{i-\frac{1}{2}}) \tag{2.94}$$

case 4:

$$\Delta\mathcal{Q}_{i+\frac{1}{2}} \leq 0, \quad \Delta\mathcal{Q}_{i-\frac{1}{2}} \leq 0 \tag{2.95}$$

We have

$$\widehat{\Delta\mathcal{Q}_{i-\frac{1}{2}}} = max(\Delta\mathcal{Q}_{i-\frac{1}{2}}, (\frac{1-\kappa^l_{i+\frac{1}{2}}}{\kappa^l_{i-\frac{1}{2}}})\Delta\mathcal{Q}_{i+\frac{1}{2}}) \tag{2.96}$$

$$\widehat{\Delta\mathcal{Q}_{i+\frac{1}{2}}} = max(\Delta\mathcal{Q}_{i+\frac{1}{2}}, (\frac{1-\kappa^r_{i-\frac{1}{2}}}{\kappa^r_{i+\frac{1}{2}}})\Delta\mathcal{Q}_{i-\frac{1}{2}}) \tag{2.97}$$

In some cases, instead of using the MUSCL scheme to reconstruct for the vector $\mathcal{Q}$, this scheme is used to reconstruct the primitive variables such as velocities, temperature and pressure or density. The experience in this Ph.D. dissertation shows that the code is more numerically stable if we reconstruct the primitive variables, instead of the vector $\mathcal{Q}$. Knowing the primitive values at the surface, the vector $\mathcal{Q}$ can be simply calculated and be used in calculation of the fluxes and integration in time.

Modified ENO

ENO is an abbreviation for *Essentially Non-Oscillatory* and refers to a reconstruction which is suitable for functions with discontinuities [75],[76]. As we addressed in MUSCL reconstruction, the use of a fixed symmetric stencil of cells to reconstruct for the flow properties in the cell surfaces can lead to unphysical extrema in the vicinity of discontinuities. ENO reconstruction method permits an asymmetric stencil of cells in order to avoid creating new extrema in the reconstruction process. The *Total Variation* of the function $\mathcal{Q}$ is defined as

$$TV(\mathcal{Q}) = \int_{x_{i-\frac{1}{2}}}^{x_{i+\frac{1}{2}}} |\frac{d\mathcal{Q}}{dx}|dx \tag{2.98}$$

The function $Q_i(x)$, which is the reconstructed function of $\mathcal{Q}$ is defined in a way to satisfy the Essentially Non-Oscillatory property described in Equation 2.99.

$$TV(Q_i(x)) \leq TV(\mathcal{Q}) + \mathcal{O}(\Delta x^3) \tag{2.99}$$

The derivative function can be written as follows.

$$\frac{d\mathcal{Q}_i}{dx} = \alpha + \beta(x - x_{i+k-\frac{1}{2}}) \qquad \text{where} \quad k = 0 \text{ or } 1 \tag{2.100}$$

Thus we have

$$TV(\mathcal{Q}_i(x)) \leq |\alpha|\Delta x_i + |\beta|\frac{(\Delta x_i)^2}{2} \tag{2.101}$$

A primitive function $I(x)$ is defined (Equation 2.102) and the variable a is selected from zero to two in order to minimize the Total Variation function (Equation 2.98). When a is equal to zero the reconstruction for $\mathcal{Q}_i(x)$ is performed using the cells $i, i+1$ and $i+2$, where for $a = 1$ the cells $i-1, i$ and $i+1$ are used. Finally, for a equal to two, the cells $i-2, i-1$ and i are the cells used to reconstruct for the function $\mathcal{Q}_i(x)$.

$$I(x) = \int_{x_{i-a-\frac{1}{2}}}^{x} \mathcal{Q}dx \qquad \text{for} \quad x_{i-a-\frac{1}{2}} \leq x \leq x_{i-a+\frac{5}{2}} \tag{2.102}$$

The variables α and β are calculated for different values of a (Equations 2.103 through 2.108), and the a which leads to minimum Total Variation function is selected to use for reconstruction. For a non-uniform grid spacing the values α and β can be expressed as follows.

For $a = 0$:

$$\alpha = \frac{2}{(\Delta x_{i+2} + \Delta x_{i+1} + \Delta x_i)}[\frac{\Delta\mathcal{Q}_{i+\frac{1}{2}}(\Delta x_{i+2} + 2\Delta x_{i+1} + 3\Delta x_i)}{(\Delta x_{i+1} + \Delta x_i)} - \frac{\Delta\mathcal{Q}_{i+\frac{3}{2}}(2\Delta x_i + \Delta x_{i+1})}{(\Delta x_{i+2} + \Delta x_{i+1})}] \tag{2.103}$$

$$\beta = \frac{6}{(\Delta x_{i+2} + \Delta x_{i+1} + \Delta x_i)}[\frac{\Delta\mathcal{Q}_{i+\frac{3}{2}}}{(\Delta x_{i+2} + \Delta x_{i+1})} - \frac{\Delta\mathcal{Q}_{i+\frac{1}{2}}}{(\Delta x_{i+1} + \Delta x_i)}] \tag{2.104}$$

For $a = 1$:

$$\alpha = \frac{2}{(\Delta x_{i+1} + \Delta x_i + \Delta x_{i-1})}[\frac{\Delta\mathcal{Q}_{i-\frac{1}{2}}(\Delta x_{i+1} + 2\Delta x_i)}{(\Delta x_i + \Delta x_{i-1})} + \frac{\Delta\mathcal{Q}_{i+\frac{1}{2}}(\Delta x_{i-1} + \Delta x_i)}{(\Delta x_{i+1} + \Delta x_i)}] \tag{2.105}$$

$$\beta = \frac{6}{(\Delta x_{i+1} + \Delta x_i + \Delta x_{i-1})}[\frac{\Delta\mathcal{Q}_{i+\frac{1}{2}}}{(\Delta x_{i+1} + \Delta x_i)} - \frac{\Delta\mathcal{Q}_{i-\frac{1}{2}}}{(\Delta x_i + \Delta x_{i-1})}] \tag{2.106}$$

For $a = 2$:

$$\alpha = \frac{2}{(\Delta x_i + \Delta x_{i-1} + \Delta x_{i-2})}[\frac{\Delta\mathcal{Q}_{i-\frac{3}{2}}(\Delta x_i - \Delta x_{i-1})}{(\Delta x_{i-1} + \Delta x_{i-2})} + \frac{\Delta\mathcal{Q}_{i-\frac{1}{2}}(\Delta x_{i-2} + 2\Delta x_{i-1})}{(\Delta x_i + \Delta x_{i-1})}] \tag{2.107}$$

$$\beta = \frac{6}{(\Delta x_i + \Delta x_{i-1} + \Delta x_{i-2})}[\frac{\Delta\mathcal{Q}_{i-\frac{1}{2}}}{(\Delta x_i + \Delta x_{i-1})} - \frac{\Delta\mathcal{Q}_{i-\frac{3}{2}}}{(\Delta x_{i-1} + \Delta x_{i-2})}] \tag{2.108}$$

After the selection of the variable a, the reconstruction of the function $\mathcal{Q}_i(x)$ can be performed by the following equations.

$$a_1 = \mathcal{Q}_{i-a} \tag{2.109}$$

$$a_2 = \frac{\Delta\mathcal{Q}_{i-a+\frac{1}{2}}}{\Delta x_{i-a+1} + \Delta x_{i-a}} \tag{2.110}$$

$$a_3 = \Delta\mathcal{Q}_{i-a+\frac{3}{2}}[\Delta x_{i-a+2} + \Delta x_{i-a+1}]^{-1}[\Delta x_{i-a+2} + \Delta x_{i-a+1} + \Delta x_{i-a}]^{-1} - \Delta\mathcal{Q}_{i-a+\frac{1}{2}}[\Delta x_{i-a+1} + \Delta x_{i-a}]^{-1}[\Delta x_{i-a+2} + \Delta x_{i-a+1} + \Delta x_{i-a}]^{-1} \tag{2.111}$$

Finally

$$\mathcal{Q}_i^r(x_{i-\frac{1}{2}}) = a_1 + a_2[\Delta\xi_1 + \Delta\xi_0] + a_3[\Delta\xi_1\Delta\xi_2 + \Delta\xi_0\Delta\xi_2 + \Delta\xi_0\Delta\xi_1] \qquad (2.112)$$

where

$$\Delta\xi_k \equiv x_{i-\frac{1}{2}} - x_{i-a+k-\frac{1}{2}} \quad , \quad k = 0, 1, 2 \qquad (2.113)$$

and

$$\mathcal{Q}_i^l(x_{i+\frac{1}{2}}) = a_1 + a_2[\Delta\xi_1 + \Delta\xi_0] + a_3[\Delta\xi_1\Delta\xi_2 + \Delta\xi_0\Delta\xi_2 + \Delta\xi_0\Delta\xi_1] \qquad (2.114)$$

where

$$\Delta\xi_k \equiv x_{i+\frac{1}{2}} - x_{i-a+k-\frac{1}{2}} \quad , \quad k = 0, 1, 2 \qquad (2.115)$$

In the *modified* ENO method, the reconstruction is downgraded to first-order if the forward and backward gradients change in sign [29].

Van Albada's Limiter

Another limiter imposed to the reconstruction to avoid formation of new extrema is Van Albada's limiter [77]. In this scheme, a function $R(\theta)$ is multiplied to the change of the vector $\mathcal{Q}_i$ to form the *limited* $\Delta\mathcal{Q}_i$. The function $R(\theta)$, which performs as a filter, is defined based on the ratio of the forward and backward gradients (θ).

$$(\Delta\mathcal{Q}_i)_{limited} = R(\theta)\Delta\mathcal{Q}_i \qquad (2.116)$$

where

$$R(\theta) = \frac{2\theta}{\theta^2 + 1} \quad , \quad \theta > 0 \qquad (2.117)$$

and

$$\theta \equiv \frac{\mathcal{Q}_{i+1} - \mathcal{Q}_i}{\mathcal{Q}_i - \mathcal{Q}_{i-1}} \qquad (2.118)$$

2.2.4 Viscous Fluxes

Since the viscous terms are linear, their calculation is considerably simpler compared with the inviscid fluxes. Viscous fluxes consist of the derivative of the velocity and temperature in each direction. Consider the function f as an arbitrary function. The derivatives of the function f in each face can be calculated as follows.

ξ face:

$$\frac{\partial f}{\partial \xi} = f_{i,j,k} - f_{i-1,j,k} \tag{2.119}$$
$$\frac{\partial f}{\partial \eta} = \frac{1}{4}(f_{i-1,j+1,k} + f_{i,j+1,k} - f_{i-,j-1,k} - f_{i,j-1,k}) \tag{2.120}$$
$$\frac{\partial f}{\partial \zeta} = \frac{1}{4}(f_{i-1,j,k+1} + f_{i,j,k+1} - f_{i-1,j,k-1} - f_{i,j,k-1}) \tag{2.121}$$

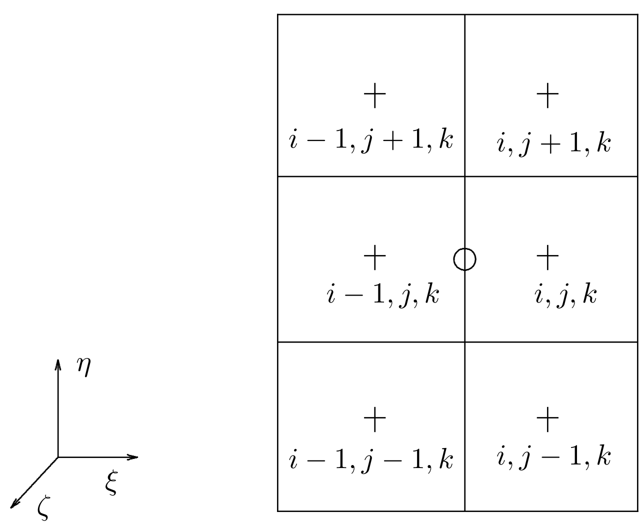

Figure 2.2: ξ Face

η face:

$$\frac{\partial f}{\partial \xi} = \frac{1}{4}(f_{i+1,j,k} + f_{i+1,j-1,k} - f_{i-1,j,k} - f_{i-1,j-1,k}) \tag{2.122}$$
$$\frac{\partial f}{\partial \eta} = f_{i,j,k} - f_{i,j-1,k} \tag{2.123}$$
$$\frac{\partial f}{\partial \zeta} = \frac{1}{4}(f_{i,j-1,k+1} + f_{i,j,k+1} - f_{i,j-1,k-1} - f_{i,j,k-1}) \tag{2.124}$$

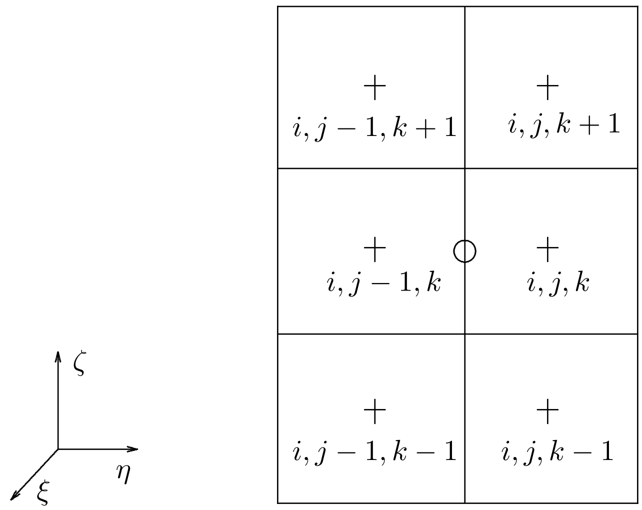

Figure 2.3: η Face

ζ face:

$$\frac{\partial f}{\partial \xi} = \frac{1}{4}(f_{i+1,j,k} + f_{i+1,j,k-1} - f_{i-1,j,k} - f_{i-1,j,k-1}) \tag{2.125}$$

$$\frac{\partial f}{\partial \eta} = \frac{1}{4}(f_{i,j+1,k} + f_{i,j+1,k-1} - f_{i,j-1,k} - f_{i,j-1,k-1}) \tag{2.126}$$

$$\frac{\partial f}{\partial \zeta} = f_{i,j,k} - f_{i,j,k-1} \tag{2.127}$$

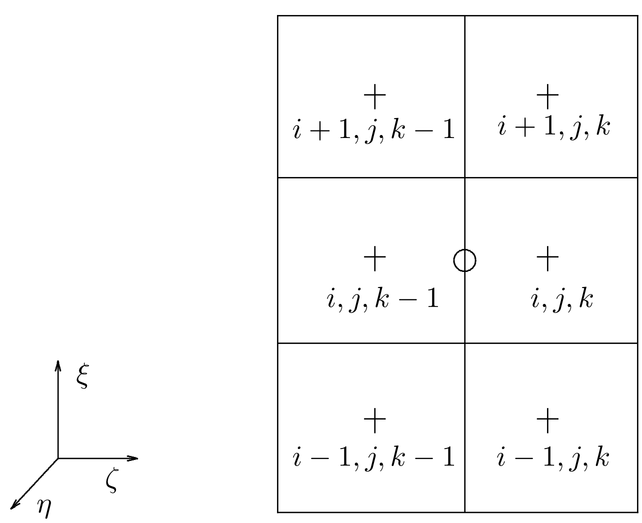

Figure 2.4: ζ Face

The viscosity coefficient and thermal conductivity is calculated by averaging the centroid values of the two adjacent cells at the face of calculation of the viscous fluxes.

2.2.5 Time Integration

Time Step

Temporal quadrature algorithms can be categorized by explicit and implicit methods. In the simpler approach known as explicit, the values Q_i are calculated at each time step independently; while in the implicit time integration, the equations are solved simultaneously. In addition to the choice of the spatial discretization, the choice of the time step influences the stability of the numerical calculations. An explicit Euler equation is conditionally stable with the time step restriction as follows.

$$\Delta t_{inv} \leq \frac{\Delta x}{|\lambda_{i,max}|} \tag{2.128}$$

where λ_i presents the eigenvalues of the Jacobian matrix $\mathcal{A}$ in Equation 2.44. We can define Δt_{CFL} and the CFL (*Courant-Friedrichs-Lewy*) number as described in the Equations 2.129 and 2.130, respectively.

$$\Delta t_{CFL} = \min_i \frac{\Delta x}{|\lambda_i|} \tag{2.129}$$

$$CFL = \frac{\Delta t}{\Delta t_{CFL}} \tag{2.130}$$

The restriction described in Equation 2.128 -known as Courant-Friedrichs-Lewy restriction- can be rewritten as

$$CFL \leq 1 \tag{2.131}$$

As a result, inviscid time step can be written as

$$\Delta t_{inv} = CFL \times \min_i \frac{\Delta x}{|\lambda_i|} \tag{2.132}$$

The viscous time step can be calculated by the Equation 2.133, where $\nu = \mu/\rho$.

$$\Delta t_{vis} = CFL \frac{[min(\Delta x, \Delta y, \Delta z)]^2}{\nu} \tag{2.133}$$

The final time step is the minimum of the viscous and inviscid time steps to assure stability in the numerical calculations. The implicit time integration methods are typically not restricted to the Courant-Friedrichs-Lewy restriction.

Runge-Kutta Method

The semi-discrete Navier-Stokes equations can be written as

$$\frac{d\mathcal{Q}_i}{dt} = RHS_i \tag{2.134}$$

where RHS_i represents the *Right-Hand-Side* of the Navier-Stokes equations and consist of the net inviscid and viscous fluxes. The *two-stage Runge-Kutta* method [78],[79] is an explicit second order accurate time integration method and can be described as follows.

$$\mathcal{Q}_i^0 = \mathcal{Q}_i^n \tag{2.135}$$

$$\mathcal{Q}_i^1 = \mathcal{Q}_i^0 + \frac{\Delta t}{2} \cdot RHS_i^0 \tag{2.136}$$

$$\mathcal{Q}_i^2 = \mathcal{Q}_i^0 + \Delta t \cdot RHS_i^1 \tag{2.137}$$

$$\mathcal{Q}_i^{n+1} = \mathcal{Q}_i^2 \tag{2.138}$$

In this algorithm we have introduced three temporary vectors $\mathcal{Q}_i^0$, $\mathcal{Q}_i^1$ and $\mathcal{Q}_i^2$, where the final temporary vector is assigned as the solution for the next time step ($\mathcal{Q}_i^{n+1}$). The matrices RHS_i^0 and RHS_i^1 are evaluated using the vectors $\mathcal{Q}_i^0$ and $\mathcal{Q}_i^1$, respectively.

DPLR's Method

The *Data Parallel Line Relaxation* method [80] is a time integration method that is only implicit in one direction (usually η direction) and explicit in the other two directions. This method is used when the grid spacing is much finer in one direction compared with the other two, and the time step is limited by the minimum spacing in that particular direction. As a result of implicit formation of the equations in that direction, the code is unconditionally stable in that direction and the Courant-Friedrichs-Lewy restriction only applies to the other two directions. This allows having a larger time step, while the calculations are still stable. However, the DPLR method is first order accurate in time.

The fully implicit form of the Navier-Stokes equations is as follows.

$$\begin{aligned}&\frac{\mathcal{Q}\nu_{ijk}^{n+1} - \mathcal{Q}\nu_{ijk}^{n}}{\Delta t} + (\mathcal{F}_{i+\frac{1}{2}}^{n+1} - \mathcal{F}_{i-\frac{1}{2}}^{n+1}) + (\mathcal{G}_{j+\frac{1}{2}}^{n+1} - \mathcal{G}_{j-\frac{1}{2}}^{n+1}) + (\mathcal{H}_{k+\frac{1}{2}}^{n+1} - \mathcal{H}_{k-\frac{1}{2}}^{n+1}) \\ &+ (\mathcal{R}_{i+\frac{1}{2}}^{n+1} - \mathcal{R}_{i-\frac{1}{2}}^{n+1}) + (\mathcal{S}_{j+\frac{1}{2}}^{n+1} - \mathcal{S}_{j-\frac{1}{2}}^{n+1}) + (\mathcal{T}_{k+\frac{1}{2}}^{n+1} - \mathcal{T}_{k-\frac{1}{2}}^{n+1}) = 0\end{aligned} \tag{2.139}$$

We can write the flux vector $\mathcal{F}$ in the following format.

$$\mathcal{F} = \mathcal{D}^{-1}\bar{\mathcal{F}}dA \tag{2.140}$$

where

$$\mathcal{D} = \begin{Bmatrix} 1 & 0 & 0 & 0 & 0 \\ 0 & n_x & s_x & t_x & 0 \\ 0 & n_y & s_y & t_y & 0 \\ 0 & n_z & s_z & t_z & 0 \\ 0 & 0 & 0 & 0 & 1 \end{Bmatrix}, \quad \bar{\mathcal{F}} = \begin{Bmatrix} \rho\bar{u} \\ \rho\bar{u}^2 + p \\ \rho\bar{v}\bar{u} \\ \rho\bar{w}\bar{u} \\ (\rho e + p)\bar{u} \end{Bmatrix} \tag{2.141}$$

and $\bar{u}$, $\bar{v}$ and $\bar{w}$ are the components of velocity in the $\hat{n}, \hat{s}$ and $\hat{t}$ directions, which are orthogonal vectors normal ($\hat{n}$) and tangent ($\hat{s}$ and $\hat{t}$) to the surface of the cell. Moreover, dA is the surface area of the ξ-face of the cell. We can further write

$$\begin{aligned} \mathcal{F}^{n+1}_{i+\frac{1}{2}} - \mathcal{F}^{n+1}_{i-\frac{1}{2}} =& \mathcal{F}^{n}_{i+\frac{1}{2}} - \mathcal{F}^{n}_{i-\frac{1}{2}} + \frac{\partial \mathcal{F}}{\partial \mathcal{Q}}\bigg|^{n}_{i+\frac{1}{2}} (\mathcal{Q}^{n+1} - \mathcal{Q}^{n})_{i+\frac{1}{2}} \\ &- \frac{\partial \mathcal{F}}{\partial \mathcal{Q}}\bigg|^{n}_{i-\frac{1}{2}} (\mathcal{Q}^{n+1} - \mathcal{Q}^{n})_{i-\frac{1}{2}} + \mathcal{O}(\Delta\mathcal{Q})^2 \end{aligned} \tag{2.142}$$

We can further expand

$$\frac{\partial \mathcal{F}}{\partial \mathcal{Q}} = \frac{\partial}{\partial \mathcal{Q}}[\mathcal{D}^{-1}\bar{\mathcal{F}}dA] = \mathcal{D}^{-1}\frac{\partial \bar{\mathcal{F}}}{\partial \mathcal{Q}}dA = \mathcal{D}^{-1}\frac{\partial \bar{\mathcal{F}}}{\partial \bar{\mathcal{Q}}}\frac{\partial \bar{\mathcal{Q}}}{\partial \mathcal{Q}} = \mathcal{D}^{-1}\frac{\partial \bar{\mathcal{F}}}{\partial \bar{\mathcal{Q}}}\mathcal{D}dA \tag{2.143}$$

where $\bar{\mathcal{Q}}$ is based on the velocity components in the $\hat{n}$, $\hat{s}$ and $\hat{t}$ directions (Equation 2.147), which are the normal and two tangent components of the surface unit vector. We can simply show that the velocity components in the x, y, z coordinate can relate to the velocity components normal ($\bar{u}$) and tangent ($\bar{v}$ and $\bar{w}$) to the surface of the control volume by the following equations.

$$u = \bar{u}n_x + \bar{v}s_x + \bar{w}t_x \tag{2.144}$$

$$v = \bar{u}n_y + \bar{v}s_y + \bar{w}t_y \tag{2.145}$$

$$w = \bar{u}n_z + \bar{v}s_z + \bar{w}t_z \tag{2.146}$$

$$\bar{\mathcal{Q}} = \begin{Bmatrix} \rho \\ \rho\bar{u} \\ \rho\bar{v} \\ \rho\bar{w} \\ \rho\bar{e} \end{Bmatrix} \tag{2.147}$$

We can further write

$$\frac{\partial \bar{\mathcal{F}}}{\partial \bar{\mathcal{Q}}} = \mathrm{R}\Lambda\mathrm{L} \tag{2.148}$$

where R and L are the right and left eigenvectors of the Jacobian matrix in Equation 2.148, respectively, and Λ is the diagonal vector of the eigenvalues as follows.

$$\Lambda = diag(\bar{u}, \bar{u}, \bar{u}, \bar{u} + a, \bar{u} - a) = diag(\lambda_1, \lambda_2, \lambda_3, \lambda_4, \lambda_5) \tag{2.149}$$

We can define

$$\Lambda^+ = \frac{1}{2} diag(\lambda_1 + |\lambda_1|, \lambda_2 + |\lambda_2|, \lambda_3 + |\lambda_3|, \lambda_4 + |\lambda_4|, \lambda_5 + |\lambda_5|) \tag{2.150}$$

$$\Lambda^- = \frac{1}{2} diag(\lambda_1 - |\lambda_1|, \lambda_2 - |\lambda_2|, \lambda_3 - |\lambda_3|, \lambda_4 - |\lambda_4|, \lambda_5 - |\lambda_5|) \tag{2.151}$$

where Λ^+ and Λ^- contain non-negative and non-positive eigenvalues, respectively. We can further write

$$\frac{\partial \mathcal{F}}{\partial \mathcal{Q}} = \mathcal{D}^{-1}\mathrm{R}\Lambda^+\mathrm{L}\mathcal{D}dA + \mathcal{D}^{-1}\mathrm{R}\Lambda^-\mathrm{L}\mathcal{D}dA = \mathrm{A}^+ + \mathrm{A}^- \tag{2.152}$$

Similarly for η and ζ faces matrices analogous to A^+ and A^- can be formed as B^+, B^- and C^+, C^-, respectively. Equation 2.142 can be further approximated to

$$\begin{aligned} \mathcal{F}^{n+1}_{i+\frac{1}{2}} - \mathcal{F}^{n+1}_{i-\frac{1}{2}} = \mathcal{F}^{n}_{i+\frac{1}{2}} - \mathcal{F}^{n}_{i-\frac{1}{2}} + \mathrm{A}^-_{i+\frac{1}{2}}\delta\mathcal{Q}^n_{i+1} + (\mathrm{A}^+_{i+\frac{1}{2}} - \mathrm{A}^-_{i+\frac{1}{2}})\delta\mathcal{Q}^n_i \\ -\mathrm{A}^+_{i+\frac{1}{2}}\delta\mathcal{Q}^n_{i-1} \end{aligned} \tag{2.153}$$

where

$$\delta\mathcal{Q}^n = \mathcal{Q}^{n+1} - \mathcal{Q}^n \tag{2.154}$$

Analogous algebraic methodology can be applied to the vectors $\mathcal{G}$ and $\mathcal{H}$ to expand the inviscid fluxes. If we exclude the viscous fluxes and write for the Euler equations we will have

$$\begin{aligned}\delta\mathcal{Q}^n_{i,j,k} &+ \frac{\Delta t}{\nu_{i,j,k}}[\mathrm{A}^-_{i+\frac{1}{2}}\delta\mathcal{Q}^n_{i+1} + (\mathrm{A}^+_{i+\frac{1}{2}} - \mathrm{A}^-_{i-\frac{1}{2}})\delta\mathcal{Q}^n_i - \mathrm{A}^+_{i-\frac{1}{2}}\delta\mathcal{Q}^n_{i-1}] \\ &+ \frac{\Delta t}{\nu_{i,j,k}}[\mathrm{B}^-_{j+\frac{1}{2}}\delta\mathcal{Q}^n_{j+1} + (\mathrm{B}^+_{j+\frac{1}{2}} - \mathrm{B}^-_{j-\frac{1}{2}})\delta\mathcal{Q}^n_j - \mathrm{B}^+_{j-\frac{1}{2}}\delta\mathcal{Q}^n_{j-1}] \\ &+ \frac{\Delta t}{\nu_{i,j,k}}[\mathrm{C}^-_{k+\frac{1}{2}}\delta\mathcal{Q}^n_{k+1} + (\mathrm{C}^+_{k+\frac{1}{2}} - \mathrm{C}^-_{k-\frac{1}{2}})\delta\mathcal{Q}^n_k - \mathrm{C}^+_{k-\frac{1}{2}}\delta\mathcal{Q}^n_{k-1}] \\ &= -\frac{\Delta t}{\nu_{i,j,k}}[\mathcal{F}^n_{i+\frac{1}{2}} - \mathcal{F}^n_{i-\frac{1}{2}} + \mathcal{G}^n_{j+\frac{1}{2}} - \mathcal{G}^n_{j-\frac{1}{2}} + \mathcal{H}^n_{k+\frac{1}{2}} - \mathcal{H}^n_{k-\frac{1}{2}}] \end{aligned} \tag{2.155}$$

where the absence of indices i, j and k implies the indices i, j and k, respectively. The DPLR method assumes implicit time integration in only one direction, which is j or η direction. As a result, the Euler equations will be further simplified to

$$\begin{aligned}&\{I + \frac{\Delta t}{\nu_{i,j,k}}[(\mathrm{A}^+_{i+\frac{1}{2}} - \mathrm{A}^-_{i-\frac{1}{2}}) + (\mathrm{B}^+_{j+\frac{1}{2}} - \mathrm{B}^-_{j-\frac{1}{2}}) + (\mathrm{C}^+_{k+\frac{1}{2}} - \mathrm{C}^-_{k-\frac{1}{2}})]\}\delta\mathcal{Q}^n_{i,j,k} + \\ &\frac{\Delta t}{\nu_{i,j,k}}[\mathrm{B}^-_{j+\frac{1}{2}}]\delta\mathcal{Q}^n_{i,j+1,k} + \frac{\Delta t}{\nu_{i,j,k}}[-\mathrm{B}^+_{j-\frac{1}{2}}]\delta\mathcal{Q}^n_{i,j-1,k} = -\frac{\Delta t}{\nu_{i,j,k}}[\mathcal{F}^n_{i+\frac{1}{2}} - \mathcal{F}^n_{i-\frac{1}{2}} + \\ &\mathcal{G}^n_{j+\frac{1}{2}} - \mathcal{G}^n_{j-\frac{1}{2}} + \mathcal{H}^n_{k+\frac{1}{2}} - \mathcal{H}^n_{k-\frac{1}{2}}] - \frac{\Delta t}{\nu_{i,j,k}}[\mathrm{A}^-_{i+\frac{1}{2}}\delta\mathcal{Q}_{i+1} - \mathrm{A}^+_{i-\frac{1}{2}}\delta\mathcal{Q}_{i-1} + \\ &\mathrm{C}^-_{k+\frac{1}{2}}\delta\mathcal{Q}_{k+1} - \mathrm{C}^+_{k-\frac{1}{2}}\delta\mathcal{Q}_{k-1}]\end{aligned} \tag{2.156}$$

The Euler equations are now in a form of implicit equations with three unknown vectors of $\delta\mathcal{Q}^n_{i,j,k}$, $\delta\mathcal{Q}^n_{i,j+1,k}$ and $\delta\mathcal{Q}^n_{i,j-1,k}$. The equations are solved simultaneously to calculate the unknown vectors, which are later used to update the vector $\mathcal{Q}$ for the next time step.

The viscous fluxes can be further expanded as

$$R^{n+1}_{i+\frac{1}{2}} = \mathcal{R}_\xi \frac{\partial\hat{\mathcal{Q}}}{\partial\xi}\Big|^{n+1}_{i+\frac{1}{2}} + \mathcal{R}_\eta \frac{\partial\hat{\mathcal{Q}}}{\partial\eta}\Big|^{n+1}_{i+\frac{1}{2}} + \mathcal{R}_\zeta \frac{\partial\hat{\mathcal{Q}}}{\partial\zeta}\Big|^{n+1}_{i+\frac{1}{2}} \tag{2.157}$$

where

$$\hat{\mathcal{Q}} = \begin{Bmatrix} \rho \\ u \\ v \\ w \\ T \end{Bmatrix} \tag{2.158}$$

and

$$\delta\hat{\mathcal{Q}} = \mathcal{M}\delta\mathcal{Q} \tag{2.159}$$

where

$$\mathcal{M} = \begin{Bmatrix} 1 & 0 & 0 & 0 & 0 \\ -\frac{u}{\rho} & \frac{1}{\rho} & 0 & 0 & 0 \\ -\frac{v}{\rho} & 0 & \frac{1}{\rho} & 0 & 0 \\ -\frac{w}{\rho} & 0 & 0 & \frac{1}{\rho} & 0 \\ \frac{-1}{\rho c_v}[e + (u^2 + v^2 + w^2)] & \frac{u}{\rho c_v} & \frac{v}{\rho c_v} & \frac{w}{\rho c_v} & \frac{1}{\rho c_v} \end{Bmatrix} \tag{2.160}$$

Further approximation can be made by neglecting the derivatives along the surface, as follows.

$$\begin{aligned} R^{n+1}_{i+\frac{1}{2}} = R^{n}_{i+\frac{1}{2}} + \mathcal{R}_\xi \frac{\partial \delta\hat{\mathcal{Q}}}{\partial \xi}\bigg|^{n}_{i+\frac{1}{2}} &= R^{n}_{i+\frac{1}{2}} + \mathcal{R}_\xi\bigg|^{n}_{i+\frac{1}{2}} \frac{(\delta\hat{\mathcal{Q}}_{i+1} - \delta\hat{\mathcal{Q}}_{i})}{\Delta\xi} \\ &= R^{n}_{i+\frac{1}{2}} + \mathcal{R}_\xi\bigg|^{n}_{i+\frac{1}{2}} M^{n}_{i+\frac{1}{2}}[\delta\mathcal{Q}_{i+1} - \delta\mathcal{Q}_{i}] \end{aligned} \tag{2.161}$$

analogous simplification can be made for the other two directions and the left surfaces.

$$\begin{aligned} S^{n+1}_{j+\frac{1}{2}} = S^{n}_{j+\frac{1}{2}} + \mathcal{S}_\eta \frac{\partial \delta\hat{\mathcal{Q}}}{\partial \eta}\bigg|^{n}_{j+\frac{1}{2}} &= S^{n}_{j+\frac{1}{2}} + \mathcal{S}_\eta\bigg|^{n}_{j+\frac{1}{2}} \frac{(\delta\hat{\mathcal{Q}}_{j+1} - \delta\hat{\mathcal{Q}}_{j})}{\Delta\eta} \\ &= S^{n}_{j+\frac{1}{2}} + \mathcal{S}_\eta\bigg|^{n}_{j+\frac{1}{2}} M^{n}_{j+\frac{1}{2}}[\delta\mathcal{Q}_{j+1} - \delta\mathcal{Q}_{j}] \end{aligned} \tag{2.162}$$

$$\begin{aligned} T^{n+1}_{k+\frac{1}{2}} = T^{n}_{k+\frac{1}{2}} + \mathcal{T}_\zeta \frac{\partial \delta\hat{\mathcal{Q}}}{\partial \zeta}\bigg|^{n}_{k+\frac{1}{2}} &= T^{n}_{k+\frac{1}{2}} + \mathcal{T}_\zeta\bigg|^{n}_{k+\frac{1}{2}} \frac{(\delta\hat{\mathcal{Q}}_{k+1} - \delta\hat{\mathcal{Q}}_{k})}{\Delta\zeta} \\ &= T^{n}_{k+\frac{1}{2}} + \mathcal{T}_\zeta\bigg|^{n}_{k+\frac{1}{2}} M^{n}_{k+\frac{1}{2}}[\delta\mathcal{Q}_{k+1} - \delta\mathcal{Q}_{k}] \end{aligned} \tag{2.163}$$

The implicit time integration employs only on the j or η direction; as a result, the final Navier-Stokes equations for the DPLR method will be simplified to the Equation 2.164.

$$\begin{aligned} &\hat{\mathrm{B}}_{i,j,k}\delta\mathcal{Q}^{n}_{i,j+1,k} + \hat{\mathrm{A}}_{i,j,k}\delta\mathcal{Q}^{n}_{i,j,k} + \hat{\mathrm{C}}_{i,j,k}\delta\mathcal{Q}^{n}_{i,j-1,k} = \mathfrak{R}_{i,j,k} \\ &- \frac{\Delta t}{\nu_{i,j,k}}[(\mathrm{A}^{-}_{i+\frac{1}{2}} - \mathcal{R}_\xi M_{i+\frac{1}{2}})\delta\mathcal{Q}^{n-1}_{i+1} - (\mathrm{A}^{+}_{i-\frac{1}{2}} + \mathcal{R}_\xi M_{i-\frac{1}{2}})\delta\mathcal{Q}^{n-1}_{i-1} \\ &(\mathrm{C}^{-}_{k+\frac{1}{2}} - \mathcal{T}_\zeta M_{k+\frac{1}{2}})\delta\mathcal{Q}^{n-1}_{k+1} - (\mathrm{C}^{+}_{k-\frac{1}{2}} - \mathcal{T}_\zeta M_{k-\frac{1}{2}})\delta\mathcal{Q}^{n-1}_{k-1}] \end{aligned} \tag{2.164}$$

where

$$\hat{\mathrm{A}}_{i,j,k} = I + \frac{\Delta t}{\nu_{i,j,k}}[(\mathrm{A}^{+}_{i+\frac{1}{2}} - \mathrm{A}^{-}_{i-\frac{1}{2}}) + \mathcal{R}_{\xi} M_{i+\frac{1}{2}} + \mathcal{R}_{\xi} M_{i-\frac{1}{2}} +$$
$$(\mathrm{B}^{+}_{j+\frac{1}{2}} - \mathrm{B}^{-}_{j-\frac{1}{2}}) + \mathcal{S}_{\eta} M_{j+\frac{1}{2}} + \mathcal{S}_{\eta} M_{j-\frac{1}{2}} + (\mathrm{C}^{+}_{k+\frac{1}{2}} - \mathrm{C}^{-}_{k-\frac{1}{2}})$$
$$\mathcal{T}_{\zeta} M_{k+\frac{1}{2}} + \mathcal{T}_{\zeta} M_{k-\frac{1}{2}}] \tag{2.165}$$

$$\hat{\mathrm{B}}_{i,j,k} = \frac{\Delta t}{\nu_{i,j,k}}[\mathrm{B}^{-}_{j+\frac{1}{2}} - \mathcal{S}_{\eta} M_{j+\frac{1}{2}}], \quad \hat{\mathrm{C}}_{i,j,k} = \frac{\Delta t}{\nu_{i,j,k}}[-\mathrm{B}^{+}_{j-\frac{1}{2}} - \mathcal{S}_{\eta} M_{j-\frac{1}{2}}] \tag{2.166}$$

$$\mathfrak{R}_{i,j,k} = -\frac{\Delta t}{\nu_{i,j,k}}[(\mathcal{F}^{n}_{i+\frac{1}{2}} - \mathcal{F}^{n}_{i-\frac{1}{2}}) + (\mathcal{G}^{n}_{j+\frac{1}{2}} - \mathcal{G}^{n}_{j-\frac{1}{2}}) + (\mathcal{H}^{n}_{k+\frac{1}{2}} - \mathcal{H}^{n}_{k-\frac{1}{2}})$$
$$+ (\mathcal{R}^{n}_{i+\frac{1}{2}} - \mathcal{R}^{n}_{i-\frac{1}{2}}) + (\mathcal{S}^{n}_{j+\frac{1}{2}} - \mathcal{S}^{n}_{j-\frac{1}{2}}) + (\mathcal{T}^{n}_{k+\frac{1}{2}} - \mathcal{T}^{n}_{k-\frac{1}{2}})] \tag{2.167}$$

Dual-Time Stepping Method

Dual-time stepping [81] is a higher order temporal accuracy time integration method with an intermediate level of iterative calculations. It allows implicit calculation of the fluxes and due to the inner iterative steps, there is no limitations on the real time step for stability issues. In this scheme, since the time accuracy is maintained in the outer loop, the temporal accuracy should not necessarily be maintained in the inner iterations and time integration techniques in pseudo-time can be applied. The integral format of the implicit governing equations with a pseudo-time derivative can be written as

$$\frac{\partial}{\partial \tau} \iiint \mathcal{Q} dV = -(\frac{\partial}{\partial t} \iiint_{V(t)} \mathcal{Q} dV + \iint_{S(t)} \mathsf{F} \cdot \hat{n} dS)^{m+1} \tag{2.168}$$

where F is the net flux and m represents a discrete solution in pseudo-time τ. Iterative calculations in the pseudo-time are performed to converge the solution at level m, and assign that to the solution for the next real time step ($n+1$). When pseudo-time is set to infinity, the temporal accuracy technique reduces to the Newton sub-iteration technique. However, the physical time step restriction applies to the Newton sub-iteration scheme. This scheme for the time integration has only been used in the numerical simulation of the laser discharge in a supersonic flow in this Ph.D. dissertation.

Gauss-Seidel Relaxation Method

The Gauss-Seidel Relaxation method is an iterative method for the steady state Navier-Stokes equations [82]. In this scheme, the derivatives of the flow variables by time is omitted and iterative calculations are performed to reach to a converged to the steady state solution. The Gauss-Seidel Relaxation method is analogous to the traditional Gauss-Seidel method, with an addition of a relaxation term to enhance the efficiency of the convergence. In this Ph.D. dissertation, this method was part of the simulation of the flow control with laser discharge in a supersonic flow, and it has not been used in the simulations of hypersonic shock wave boundary layer interactions.

2.2.6 Message Passing Interface (MPI)

MPI or *Message Passing Interface* is a parallel computing architecture designed for high-performance calculations. It is a message-passing interface which is used for communication among processes that are used for parallel programming on a distributed memory system. This powerful interface allows programmers to discretize the computational domain into zones and assign the calculations of each zone to discrete processes. All the simulations in this Ph.D. dissertation have been performed in an MPI interface. An MPI code in C++ language is written partially by the author and is used in most of the simulations in this Ph.D. dissertation.

2.2.7 Boundary Condition

The boundary conditions can be implemented by some imaginary or ghost cells at each boundary of each zone that has been discretized from the whole computational domain. The flow variables in these imaginary cells can be assigned in a way that the desired boundary condition be implemented at that boundary. In the calculation of the fluxes in the cell surfaces of the real cells, the values of the ghost cells will be used and the effect of the boundary condition will propagate in the computational domain. Some of the boundary conditions used in this Ph.D. dissertation is described in this section.

Fixed Boundary Condition

The fixed boundary condition is used at the inflow boundary of the computational domain and it assigns fixed values to all the components of the vector $\mathcal{Q}$. When the freestream is supersonic this boundary condition is applicable, since all the eigenvalues of the Jacobian matrix are positive and there is no upstream propagation of information. As a result, all flow parameters at the inflow boundary can be fixed to the freestream condition.

Zero Gradient Boundary Condition

Zero gradient boundary condition is used at the outflow of the computational domain and it provides an approximation that the flow parameters are not changing in the direction normal to the boundary. When a boundary layer appears in the flow, this approximation can be accurate for the outflow boundary when it is orthogonal to the solid surface and the boundary layer is well-developed. The mathematical description of this boundary condition is as follows.

$$\frac{\partial \mathcal{Q}}{\partial n} = 0 \tag{2.169}$$

Symmetry or Slip Boundary Condition

The conditions used in the symmetry or slip boundary condition is as follows.

$$\vec{V} \cdot \hat{n} = 0 \tag{2.170}$$

$$\frac{\partial}{\partial n}(\vec{V} \times \hat{n}) = 0 \tag{2.171}$$

$$\frac{\partial p}{\partial n} = 0 \tag{2.172}$$

$$\frac{\partial T}{\partial n} = 0 \tag{2.173}$$

where $\vec{V}$ is the velocity vector and $\hat{n}$ is the normal unit vector to the surface of the boundary.

No-slip Adiabatic Boundary Condition

The conditions used in the no-slip adiabatic boundary condition is as follows.

$$\vec{V} \cdot \hat{n} = 0 \tag{2.174}$$

$$\vec{V} \times \hat{n} = 0 \tag{2.175}$$

$$\frac{\partial p}{\partial n} = 0 \tag{2.176}$$

$$\frac{\partial T}{\partial n} = 0 \tag{2.177}$$

No-slip Isothermal Boundary Condition

The conditions used in the no-slip isothermal boundary condition is as follows.

$$\vec{V} \cdot \hat{n} = 0 \tag{2.178}$$

$$\vec{V} \times \hat{n} = 0 \tag{2.179}$$

$$\frac{\partial p}{\partial n} = 0 \tag{2.180}$$

$$T\Big|_{wall} = T_{wall} \tag{2.181}$$

Internal Boundary Condition

The faces of the zones discretized from the computational domain are labeled by identification numbers that are recognized in the solver code. The surfaces with matching identification numbers are considered as equivalent surfaces of the neighboring zones. The ghost cells of the neighboring zones are updated using the information of the matching real cells in the other zone by the internal boundary condition. The information in the zones propagates to other zones in the computational domain by the application of the internal boundary condition.

2.2.8 Challenges of High Gradients

At hypersonic speeds, the gradient of the flow parameters inside the boundary layer -especially close to the wall- can be very large. In cases with a cold solid wall, this large gradient can impose unphysical values for the ghost cells. As we discussed in section 2.2.7, the flow parameters in the ghost cells are calculated using the boundary condition at that boundary. At a finite grid spacing and large gradients, the boundary condition might impose the ghost cells unphysical values such as negative pressure and temperature. This problem would have vanished if we could have had infinitely small grid spacing at the cold solid boundaries, which is impossible to achieve. In order to overcome this problem, the ghost cells at the cold wall should become irrelevant and the fluxes, reconstruction and the external boundary condition should be recalculated by methods with omission of the ghost cells in that boundary.

Chapter 3

Description of the Experiments

To pursue one of the main objectives of this Ph.D. dissertation, the numerical results need to be compared with the experimental data to assess the capability of the numerical methods in prediction of the flow parameters in high speed flows. In this Ph.D. dissertation three separate experiments are simulated and the results of the numerical calculations are compared with the experiments for validation. The experiments are conducted in separate studies in different research groups.

3.1 Adelgren *et.al.* Experiment

In the experiment conducted by Adelgren *et.al.* [17] a sphere with diameter of 25.4 mm is mounted on a sting in a Mach 3.45 supersonic wind tunnel (Figure 3.1). The sphere is rotatable about a spanwise axis. The pressure at any selected angle in the vertical plane is measured using an Endevco pressure transducer in a 1.32 mm $\times$ 1.78 mm deep cavity within the sphere. The uncertainty in the pressure measurements for the Endevco transducers is 0.05 psi [83]. A pulsed Nd-YAG laser beam (532 nm) creates a high temperature plasma for three different energy deposition levels in the upstream of the sphere which affects the flow.

When the laser is discharged in a focused volume, the air absorbs some of that energy and a plasma region with toroidal vortex ring forms [26]. In addition, a spherical blast wave forms from the plasma region moving radially outward while getting weaker as it propagates [84]. This blast wave interacts with the sphere and increases its surface pressure momentarily. The heated plasma convects with the freestream and interacts with the blunt body shock causing a lensing forward upstream of the shock wave and momentary reduction of the surface pressure.

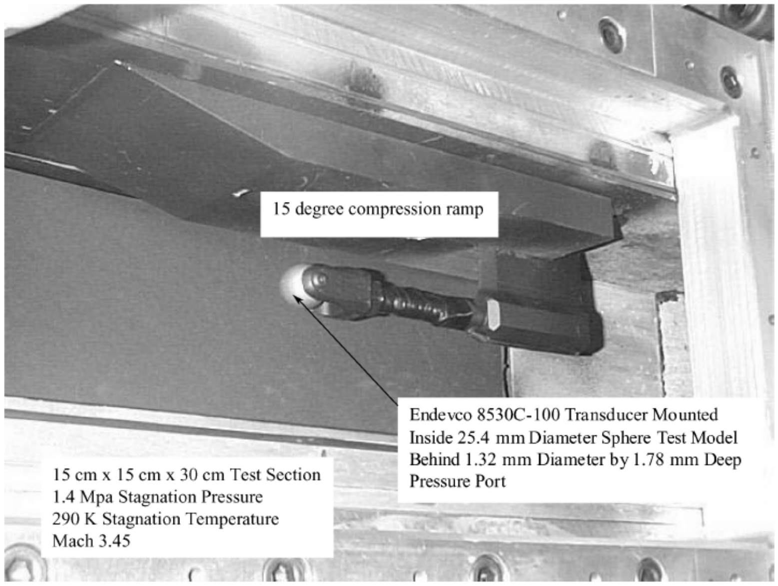

Figure 3.1: Experimental Setup [17]

The test condition is shown in Table 3.1 and the locations where the temporal pressure on the sphere is measured are presented in Table 3.2. In this experiment three different levels of laser discharge energy (as measured at the laser exit) are used. Experimental diagnostics include the distribution of pressure over time on the sphere and schlieren images. Figure 3.2 shows schlieren images for a 283 mJ energy discharge. The blast wave, lensing of the blunt body shock, the complex wave structure and the formation of the streamwise vorticity are evident. Figure 3.3 shows the temporal pressure distribution on the surface of the sphere for a discharge energy of 127 mJ. The interaction of the blast wave with the sphere causes the first pressure jump in Figure 3.3 which occurs at $t \approx 30\mu s$ (Figure 3.2(b)).

The non-dimensional experimental pressure history on the centerline of the sphere for laser energy discharge of Q=13, 127 and 258 mJ is presented in the Figure 3.4. In this figure τ is the normalized time using the freestream velocity and the diameter of the sphere and p_{02} is the stagnation pressure on the sphere centerline in the absence of the laser discharge. Experimental results show a strong dependency of the first peak pressure -which is due to the interaction of the blast wave with the sphere surface- on the laser discharge energy. Therefore, the first peak pressure is the single experimental value used to define the laser energy deposition model.

Table 3.1: Experimental Conditions[17]

Property	*Parameter*	*Value*
Freestream	Mach number	3.45
	Static pressure p_∞ (kPa)	13.1
	Static temperature T_∞ (K)	77.8
Laser	Pulse energy Q (mJ)	13, 127 and 258
	$Q/p_\infty L^3$	0.0606, 0.592, 1.202
	Distance L (mm)	25.4
	Beam focal volume (mm^3)	3
	Beam focal length (mm)	255
	Pulse duration (ns)	10
Hemisphere-cylinder	Diameter D (mm)	25.4

Table 3.2: Pressure Ports (deg)

13 mJ	127 mJ	258 mJ	13 mJ	127 mJ	258 mJ	13 mJ	127 mJ	258 mJ
56	57	57	19	19	19	-18	-19	-18
46	47	46	11	12	10	-29	-30	-32
37	39	36	1	1	0	-42	-43	-43
28	30	29	-8	-10	-9	-56	-55	-55

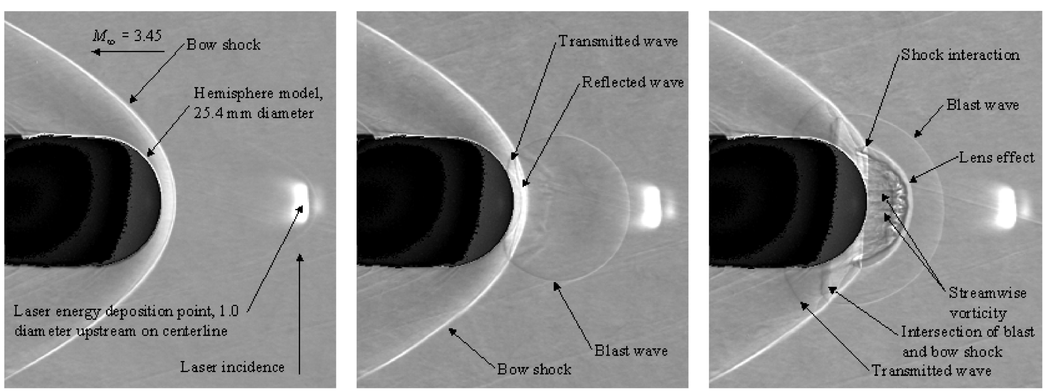

(a) $t = 0$ μs (b) $t = 30$ μs (c) $t = 50$ μs

Figure 3.2: Schlieren Images [17] (283 mJ)

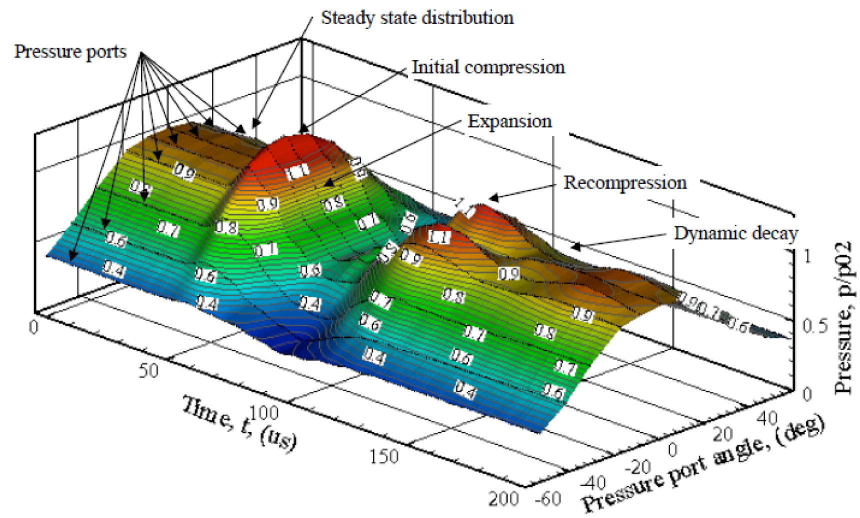

Figure 3.3: Experimental Surface Pressure *vs* Time [17] (127 mJ)

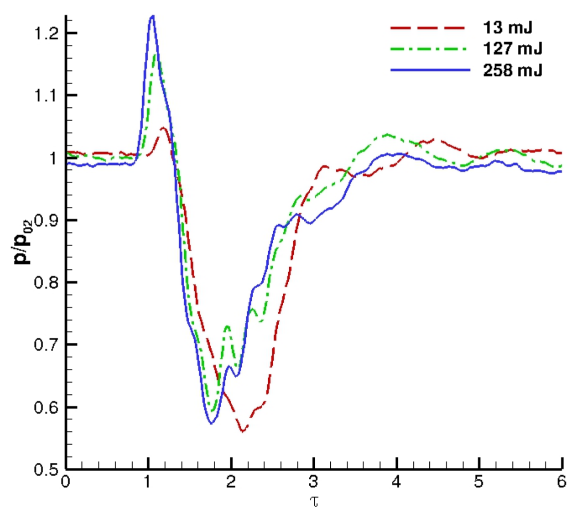

Figure 3.4: Experimental Centerline Pressure *vs* Time for Three Energy Levels [17]

3.2 Chanetz *et.al.* Experiment

The objective of the experiment conducted by Chanetz [85] was to qualify a laminar shock wave boundary layer interaction in an axisymmetric flow. The model is a hollow cylinder with a sharp leading edge, followed by a flare and a cylindrical part. The flare angle is 30^0 which is sufficient to cause boundary layer separation. The R5Ch wind tunndel is used in this experiment and it is designed to produce a uniform Mach 10 flow in the test section. The pressure and heat transfer on the model were measured. Variable reluctance VALIDYNE DP 45 differential transducers were used to measure the wall pressure. The heat transfer was determined by measuring the temperature change on the surface of the hollow cylinder in the first few seconds of the experiment. The temperature measurements were conducted using a thermometer element which is a platinum film on an insulating support made of MACOR ceramic.

The schematic figure of the model is shown in Figure 3.5. The length L used in the Reynolds definition is the distance between the sharp leading edge and the beginning of the flare and is 0.102 m. The diameter of the hollow cylinder flare at the leading edge and at the end of the flare is 0.065 m and 0.115 m, respectively. The separation line and the attachment lines are evident in Figure 3.6 and they are located at $X/L = 0.77$ and $X/L = 1.31$, respectively. The test conditions are presented in Table 3.3.

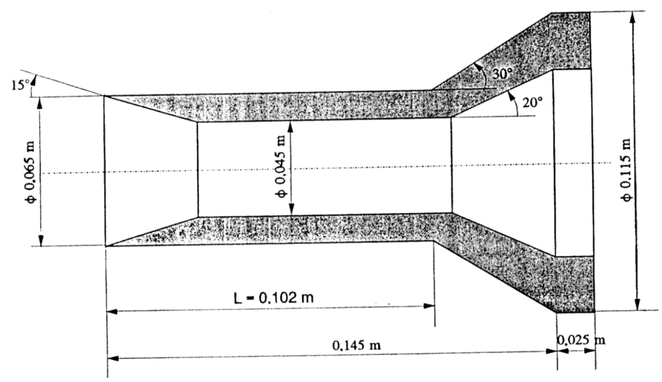

Figure 3.5: Schematic Figure of the Model [85]

Table 3.3: Experimental Conditions [85]

Parameter	*Value*
Mach number	9.91
Static pressure p_∞ (Pa)	6.3
Static temperature T_∞ (K)	51
Density ρ_∞ (kg/m^3)	0.43×10^{-3}
Reynolds number $\rho_\infty U_\infty L/\mu_\infty$	18,375
Wall temperature T_w (K)	293
Stagnation temperature T_{st} (K)	1050
Stagnation pressure p_{st} (Pa)	2.5×10^5

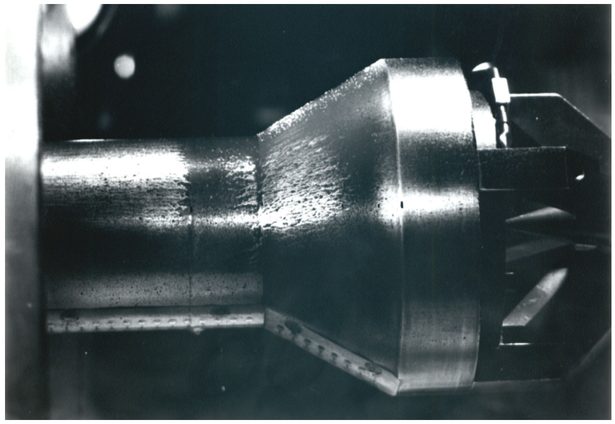

Figure 3.6: Visualization of the Separated Area [85]

3.3 Hiers *et al.* Experiment

The experiment conducted by Hiers *et.al.* [69] investigates the shock wave/laminar boundary layer interaction in a hypersonic flow over a blunt fin. Specifically, it investigates the effects of the shock wave impingement on the heat transfer of the leading edge of a blunt cylindrical fin and the flowfield characteristics at Mach 14. The model used in this research is a cylindrical blunt fin with sweep angles $\Lambda = 0^0$, 22.5^0 and 45^0, mounted on a sharp flat plate (Figure 3.7). The schematic of the model is presented in Figure 3.8, where all the dimensions are normalized with the diameter of the blunt fin ($D = 2.54$ cm (1 in)).

The experiment was conducted in the Ames 1-foot shock tunnel with reservoir stagnation enthalpy and stagnation pressure of 10.5 MJ/kg and 290 atm, respectively. The Reynolds number based on the diameter of the fin at the test section is 8,000, indicating that the flow is laminar. More information on the average flow parameters at the test section is presented in Table 3.4. The non-equilibrium effects are reported to be of negligible influence on the primarily convective phenomena of interest in this study, and the enthalpy of the frozen degrees of freedom at the test section is reported to be less than 10 percent of the total enthalpy. The model, which is initially at the isothermal condition of the room temperature is almost instantly exposed to the flow. The time average heat transfer on the blunt leading edge is measured in the experiment and normalized with the stagnation point heat transfer rate calculated by the method of Fay and Riddle [86] . The total uncertainty in the measurements of the heat transfer rate is reported less than ±20 percent and the estimated location of the heat transfer peak in the experiment is to an accuracy of 0.2 mm.

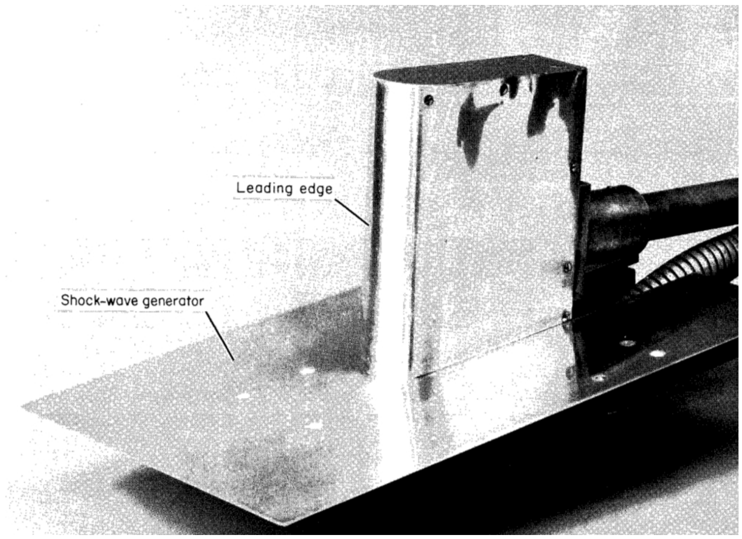

Figure 3.7: Experimental Setup [69]

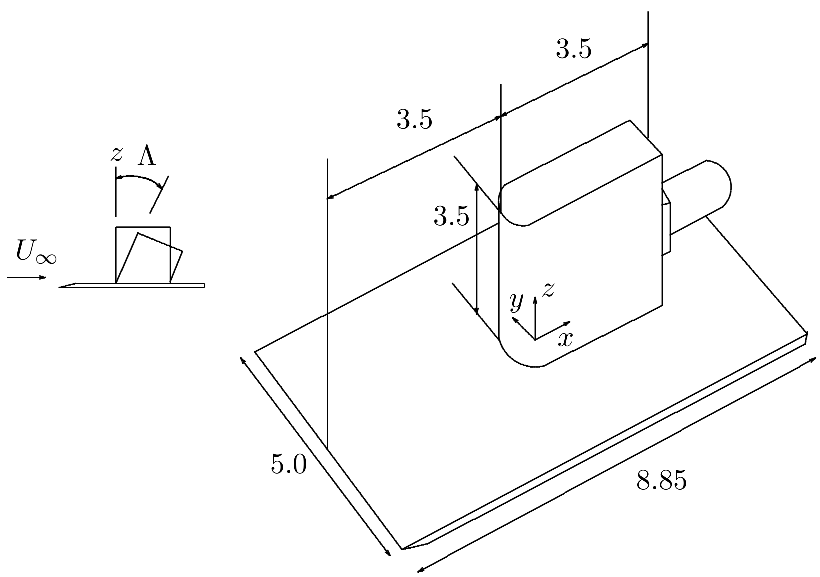

Figure 3.8: Schematics of the Model

Table 3.4: Experimental Condition[69]

Parameter	*Value*
Mach number	14
Reynolds number, $Re_d = \rho_\infty U_\infty D/\mu_\infty$	8,000
Stagnation pressure p_{st} (MPa)	29.38
Stagnation enthalpy h_0 (MJ/kg)	10.5
Velocity U_∞ (m/s)	4,270
Static temperature T_∞ (^{0}K)	195
Wall temperature T_w (^{0}K)	293
Diameter of the fin D (cm)	2.54
Sweep angle of the fin (Λ)	0^0, 22.5^0, 45^0

Chapter 4

Numerical Simulation Methods

4.1 Numerical Simulation of Adelgren *et.al.* Experiment

The experiment conducted by Adelgren *et.al.* [17] is simulated using both inviscid and viscous models. The laser discharge is modeled as an initial condition added to the steady state solution developed before the energy discharge (Figure 4.1). In the simulation, the energy deposition is modeled as a spherically symmetric region with radius r_0 and uniform temperature $T_\infty + \Delta T$ (Equation (4.1)). The density and the velocity of the heated region is the same as the freestream condition at the instant of the laser discharge due to the assumption of an instantaneous energy deposition. The pressure is calculated using the perfect gas equation.

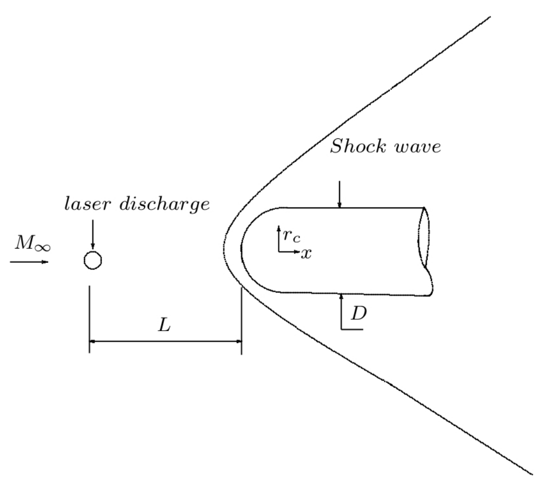

Figure 4.1: Schematic Domain

$$T = \begin{cases} T_\infty + \Delta T & ; r \leq r_o \\ T_\infty & ; r > r_o \end{cases} \tag{4.1}$$

Equation 4.1 describes the temperature distribution in the initial condition of the laser discharge where r is the spherical radius measured from the laser discharge focal point (not to be confused with the cylindrical radius r_c in Figure 4.1) and r_0 is the initial radius of the spherical plasma region, which is calculated using the volume of the plasma region in the experiment (Table 3.1). The laser is focused at the distance of L from the sphere on the centerline. In this study L is equal to the diameter of the hemisphere.

In the simulation, the amount of energy added to the volume V due to the laser discharge can be determined using the following equation.

$$\Delta E_s = \int_V \rho(c_v T + \frac{1}{2}\mathbf{u}.\mathbf{u})\bigg|_{\text{after}} dV - \int_V \rho(c_v T + \frac{1}{2}\mathbf{u}.\mathbf{u})\bigg|_{\text{before}} dV \tag{4.2}$$

Since the velocity and density remains the same during the instantaneous deposition of the energy, the added energy can be further simplified.

$$\Delta E_s = \int_V \rho c_v T\bigg|_{\text{after}} dV - \int_V \rho c_v T\bigg|_{\text{before}} dV \tag{4.3}$$

and therefore

$$\Delta E_s = \rho_\infty c_v \Delta T V \tag{4.4}$$

Dimensional analysis provides an understanding of the pressure history on the hemisphere. The first peak pressure is caused by the interaction of the blast wave with the surface of the hemisphere. In the viscous simulation, the non-dimensional first peak pressure (normalized using the total pressure after the blunt body shock in the absence of the laser discharge) depends on the following parameters

$$\frac{p_{\text{peak}}}{p_{o_2}} = g(M_\infty, \varepsilon, L/D, \gamma, r_o/D, Re, Pr) \tag{4.5}$$

where M_∞ is the freestream Mach number, $\varepsilon_s = \Delta E_s/p_\infty L^3$ is the dimensionless energy deposition parameter, γ is the ratio of the specific heats, $Re = \rho_\infty U_\infty D/\mu_\infty$ is the Reynolds number and Pr in the laminar Prandtl number. The peak pressure weakly depends on r_0/D, provided that $r_0/D << 1$ and Re and Pr numbers are viscous phenomenon and they are only considered in the viscous simulation.

The normalized energy deposition parameter for the experiment (ε_e) is defined as follows [87],[88].

$$\varepsilon_e = \frac{Q}{p_\infty L^3} \tag{4.6}$$

where Q is the laser discharge energy measured at the laser exit. The values for the experimental dimensionless energy deposition parameter studied in this research are listed in Table 3.1. In the numerical simulation, this parameter is

$$\varepsilon_s = \frac{\Delta E_s}{p_\infty L^3} = \frac{\rho_\infty c_v \Delta T V}{p_\infty L^3} = \frac{\rho_\infty c_v \Delta T (4/3)\pi r_0^3}{p_\infty L^3} = \frac{4}{3}\pi(\frac{r_0}{L})^3 \frac{\rho_\infty R \Delta T}{(\gamma-1)\rho_\infty R T_\infty} \tag{4.7}$$

$$\Rightarrow \varepsilon_s = \frac{4}{3}\frac{\pi}{(\gamma-1)}\frac{\Delta T}{T_\infty}\left(\frac{r_o}{L}\right)^3 \tag{4.8}$$

The *thermal efficiency* can be defined as

$$\eta = \frac{\Delta E_s}{Q} \tag{4.9}$$

where ΔE_s is the amount of the energy needed in the numerical simulation to match the normalized first peak pressure with that of the experiment. The radius of the initial spherical plasma region (r_0/D) is calculated using the volume of the plasma in the experiment presented in Table 3.3.

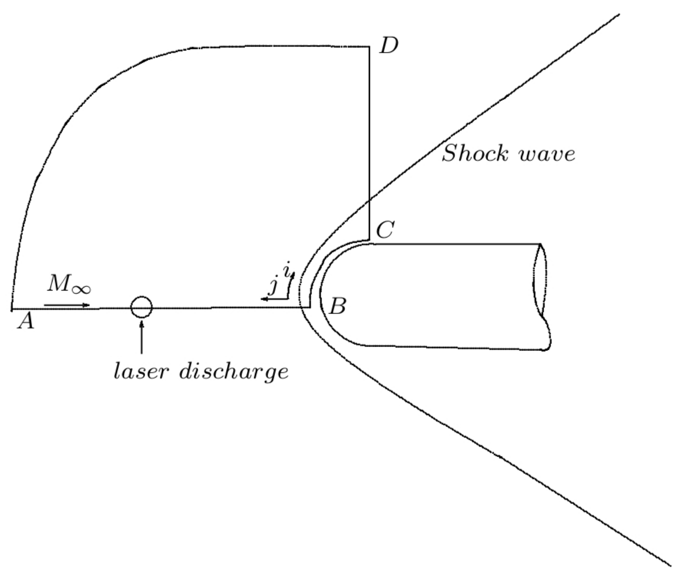

Figure 4.2: Computational Domain

The computational domain is shown in the Figure 4.2. The flow at the boundary CD in Figure 4.2 is supersonic; therefore, the flow parameters past this point do not affect the upstream flow. If we are using a viscous model, a boundary layer will form on the sphere with a subsonic sublayer. For a well-developed boundary layer, the equations governing the flow will become parabolic and therefore, we still do not have a propagation of the information upstream. As a result, it is reasonable to study a hemisphere instead of a sphere due to its simplicity. The boundary AD is fixed at the freestream condition. AB is the axis of symmetry and the computational domains becomes three dimensional when it rotates from the axis of AB, although we still have a two-dimensional flow. The zero normal gradient boundary condition is used in the boundary of CD. A tangency boundary condition is used for BC in the inviscid model and no-slip adiabatic boundary condition is considered for this surface in the viscous model. The simulations are conducted using the commercial software GASPex [29], and the structural grids are created by ANSYS ICEM CFD commercial code.

4.1.1 Inviscid Model

In this simulation, inviscid perfect gas model is considered for calculation of the flow. Therefore the Euler equations and the Ideal Gas Equation are solved to simulate the flow. The flux algorithm is second order upwind-biased Van Leer [73] with the Modified ENO limiter [75],[76]. The steady state solution is initially obtained using Gauss-Seidel [82] relaxation with a constant CFL number of one. Then the energy deposition is simulated as a new initial condition added to the steady state solution and it is solved using a second order Runge-Kutta [78] scheme.

A grid refinement study is conducted using three sequences of mesh with the spacing half of the previous one (Table 4.1). The criteria of the grid refinement study is the normalized first peak pressure P_{peak}/P_{02}. The relative difference of this parameter in the fine and base grids is 0.37% and 0.40%, respectively.

Table 4.1: Details of Grid (inviscid model)

Grid	$\Delta_{\min,i}/D$	$\Delta_{\min,j}/D$	*No. of nodes*
coarse	$6.540 \cdot 10^{-4}$	$8.333 \cdot 10^{-4}$	$0.270 \cdot 10^{6}$
base	$3.270 \cdot 10^{-4}$	$4.167 \cdot 10^{-4}$	$1.080 \cdot 10^{6}$
fine	$1.645 \cdot 10^{-4}$	$2.083 \cdot 10^{-4}$	$4.320 \cdot 10^{6}$

4.1.2 Viscous Model

For this part of the simulation, viscosity is added to understand its effects on the structure of the flow. The Navier-Stokes equations and the Ideal Gas Equation are solved to simulate the flow. In this simulation, the second order upwind-biased Van Leer method [73] with the Modified ENO limiter [75],[76] is used for the flux algorithm. The steady state condition prior to the energy deposition is obtained using Gauss-Seidel [82] relaxation with the CFL number fixed at one. For the unsteady part of the simulation second order accurate implicit dual time stepping is performed [81].

A grid refinement study is performed similar to the inviscid cases with three sequences of mesh with each spacing half the previous one. The information of the grids is presented in Table 4.2. On the axis of the symmetry starting from the surface of the hemisphere a growth ratio of 1.04 is used and continued as a uniform spacing as the non-dimensional spacing reached to 0.001. The minimum non-dimensional spacing for the fine grid in this direction is 1.76×10^{-5}. The spacing is normalized using the diameter of the hemisphere. Uniform spacing is used along the surface of the hemisphere. the grid refinement study of steady state viscous simulation is based on the skin friction on the hemisphere surface. The relative difference of this parameter between fine and middle grids is 7%.

Table 4.2: Details of Grid (viscous model)

Grid	Δ_i/D	$\Delta_{\min,j}/D$	*No. of nodes*
coarse	$13.085 \cdot 10^{-4}$	$7.041 \cdot 10^{-4}$	$0.2364 \cdot 10^{6}$
medium	$6.542 \cdot 10^{-4}$	$3.520 \cdot 10^{-4}$	$0.9456 \cdot 10^{6}$
fine	$3.271 \cdot 10^{-4}$	$0.176 \cdot 10^{-4}$	$3.7824 \cdot 10^{6}$

4.1.3 Determination of Laser Discharge Parameter ($\Delta T/T_\infty$)

The experimental results for the unsteady pressure distribution on the centerline of the hemisphere (Figure 3.4) show that the first peak pressure -which is the result of the interaction of the blast wave with the hemisphere surface- is the most influenced parameter by the amount of energy deposited during the laser discharge. Therefore, in these simulations, the first peak pressure is the single criterion to determine the energy of the laser discharge in the numerical calculations. The energy of the laser discharge in the numerical simulations can be calculated using Equation (4.8). The radius of the initial laser discharge region is fixed and determined by the volume of the plasma reported in the experiment (Table 3.1). As a result, the only parameter to match the experimental first peak pressure is $\Delta T/T_\infty$. Iterative calculations with different $\Delta T/T_\infty$ (*i.e.,* different energies in the laser discharge for the numerical simulations) were performed until the first peak pressure of the numerical calculations matched the experiment within 5%. The efficiency of the laser discharge can be calculated with Equation (4.9) where we have the ratio of the energy discharged in the numerical simulation to the experiment.

4.2 Numerical Simulation of Chanetz *et.al.* Experiment

In this study the experiment of Chanetz [85] was simulated numerically with a laminar perfect gas model. The flow is assumed to be uniform at the inflow with Mach number equal to 9.91 and Re_L = 18,375. All the numerical parameters are normalized with freestream properties and the lengths are normalized with L which is the distance from the leading edge of the model to the beginning of the flare (Figure 4.3). Since the fluid is assumed to be viscous, perfect gas with no chemical reactions, the unsteady laminar Navier-Stokes and Ideal Gas equations can be used to solve for the computational domain.

Figure 4.3 shows the computational domain in which AG and FE boundaries have freestream boundary condition and symmetry boundary condition is applied for AB, GF and ED boundaries. For the wall (BC) a no-slip isothermal boundary condition is used and CD has zero gradient boundary condition. An MPI code was developed in part by the author for the laminar ideal gas model and has been validated using the exact solution of the compressible Blasius problem. The computations were performed on a 48 core machine. The second order accurate Runge Kutta [78] algorithm is used to integrate in time to reach the steady state. In this simulation, the inviscid flux algorithm is Roe's [71],[72] scheme and the reconstruction is performed by second order primitive MUSCL [89],[90] with the CFL number fixed at 0.2 and Prandtl number of

0.72. Moreover, the powerlaw viscosity law is used to calculate the viscosity coefficient. The grid has been created by a C++ code by the author and the details of the grids are presented in Table 4.3. Both grids have uniform spacing in all directions.

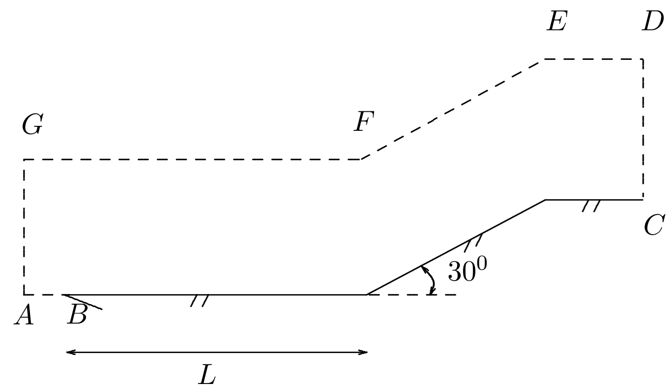

Figure 4.3: Computational Domain

Table 4.3: Details of the Grid in Present Study

Grid	*No. of cells*	Δ_i/L	Δ_j/L
Fine	3,110,400	1.372×10^{-3}	3.4391×10^{-4}
Coarse	1,382,400	2.0576×10^{-3}	5.0364×10^{-4}

4.3 Numerical Simulation of Hiers *et.al.* Experiment

The experiment of Hiers *et.al.* [69] is numerically simulated with a laminar perfect gas model. The equations used in this simulation are based on normalized properties using the freestream conditions (Table 3.4) and the length scale is chosen to be the diameter of the cylindrical fin. The inflow is assumed to be uniform with Mach number 14 and the Reynolds number based on the diameter of the fin equal to 8,000. The equations for the chosen model, which is laminar perfect gas, are the Navier-Stokes and Ideal Gas equations. The equations are solved using an MPI code partially written by the author in C++ language and validated before. The finite volume method is used in the code and the unsteady equations are integrated in time by DPLR method [80] in the beginning of the calculations and a second order Runge-Kutta method [79] for the rest of the time integration. Second order primitive MUSCL [89],[90] is used to reconstruct the pressure, temperature and the velocities and the inviscid fluxes are solved by Roe's scheme [71],[72]. Sutherland's law [91] is used to calculate the molecular viscosity of the flow and the laminar Prandtl number is assumed fixed at 0.72.

4.3.1 Grid Generation

The grid is generated using a C++ code written by the author. The flow structure for this geometry is symmetric from the center-plane of the cylindrical blunt fin. As a result, a symmetry boundary condition is used at the mentioned boundary, and only half of the domain is simulated in this numerical simulation. The grid consists of layers of zones that are built over one another. Primarily, a simple computational domain, presented in Figure 4.4 is chosen, with the left boundary fixed at the freestream condition and front, rear and top boundaries with symmetry boundary condition. The left boundary is the outflow boundary with zero-gradient boundary condition, and the solid walls have no-slip isothermal boundary condition. I should add that since the height of the fin is larger than twice the diameter of the fin, it can be considered as a semi-infinite fin [65] and symmetry boundary condition can be used at that boundary for the zero degree sweep angle case. Moreover, it will not be necessary to simulate for the whole height of the fin; therefore, in the grid refinement study section of this research, the flow is simulated upto the height of $z/D = 2.36$ of the fin to save the computational costs.

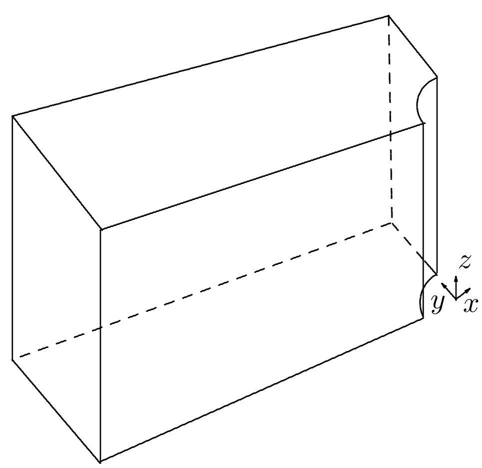

Figure 4.4: Primary Computational Domain

Calculation with this initial computational domain, provides with approximate information such as the location and angle of the shock waves and the extent of the boundary layer thickness. This information can be used to omit some of the zones that have the freestream condition without change throughout the whole calculations. Having these omission of zones, we can have a finer grid with the same computational resources. Moreover, some further examination of the results, help us decide to add some zones where needed, which are going to be explained later in this section.

The schematics of the final computational domain for the zero degree sweep angle case is presented in Figure 4.5, with the top view of the first layer of the grid presented in Figure 4.6. In this final computational domain, there are 127 zones, with 15 zones in the first layer (Figure 4.6). The process of omitting the unnecessary zones start from the second layer, knowing the locations and angles of the physical phenomena, approximated in previous calculations in prior computational domains. In this final computational domain, we have one layer with 15, 5 layers with 14 and 7 layers with 6 zones. The height of each zone is the same, but stretching in the i and j direction has been implemented by having different lengths in the zones in those directions. The lengths in Figure 4.6 is normalized by the diameter of the fin.

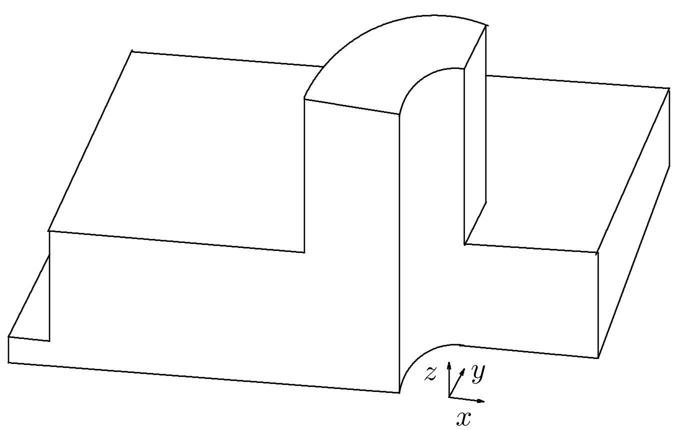

Figure 4.5: Computational Domain, 0^0 Sweep Angle

The zones 1-8 and 10-13 in Figure 4.6 represent the plate and have no-slip isothermal boundary condition on the bottom; however, the zones 9, 14 and 15 have symmetry boundary condition, and they are not presenting the zones over the plate. The reason for addition zones 10-13 and simulating further on the plate was that the prior calculations showed that the boundary layer at the exit was not well-developed and the zero-gradient boundary condition was not a suitable boundary condition to use for that boundary.

The unphysical use of the zero-gradient boundary condition at that boundary led to entrance of the streamlines from the outflow boundary and creating unphysical results. Therefore, a larger portion of the plate is simulated to allow the boundary layer to become well-developed and the zero-gradient boundary condition become physically sensible to be implemented at that boundary.

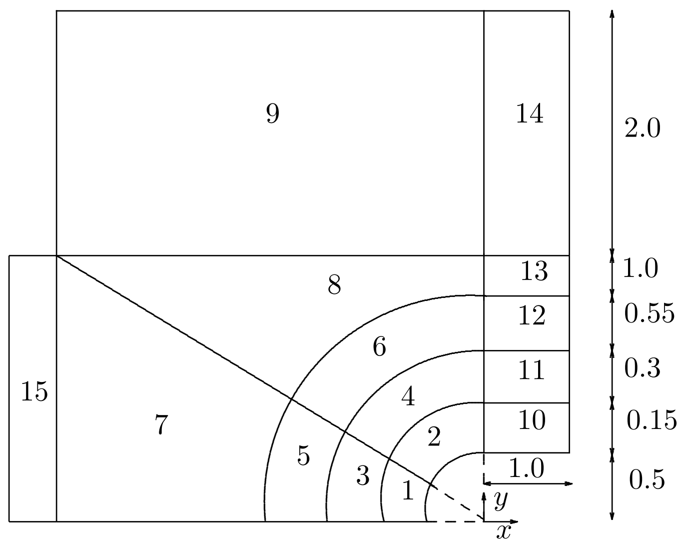

Figure 4.6: Top View of the First Layer

Zones 9 and 14 with symmetry boundary condition on the bottom are added due to observance of a very large separated region, which is going to be discussed in the next chapter. Due to the effect of that large separated region, the flow further away from the plate needed to be simulated and the zero-gradient boundary condition was not a suitable boundary condition to simulate the behavior of the flow at that part. Moreover, the fixed boundary condition needed to be implemented further away from the formation of the boundary layer to avoid generation of a subsonic region at that boundary. Therefore, zone 15 is added at the inflow with a symmetry boundary condition at the bottom to assure the physical implementation of the fixed boundary condition at the inflow.

Moreover, due to high Mach number in these simulations ($M_\infty = 14$) the gradients of the flow parameters are large, especially at the vicinity of the cold wall on the fin. To avoid numerical instability, one of the approaches used in this study is to provide a better initial condition for the unsteady calculations. Since the steady state solution is of our interest, the choice of the initial condition does not necessarily need to be the experimental initial condition. As a result, primary calculations with first order reconstruction and no-slip adiabatic boundary condition is used for further calculations with second order MUSCL [89],[90] reconstruction with no-slip adiabatic boundary condition. The results of those calculations are used as the initial condition for second order MUSCL reconstruction and no-slip isothermal boundary condition. The solid walls in these simulations are cold with one order of magnitude lower temperature at the wall comparing to the adiabatic calculations. As a result, step by step reduction of the wall temperature has been taken place by continuously reducing the wall temperature to the experimental condition.

The analogous approach has been used for the 22.5^0 sweep angle case. Figure 4.7 presents the schematics of the final computational domain. The algorithm used to create the computational domain for the 22.5^0 case is the same as the 0^0 case, with the addition of a simple 22.5^0 rotation of x and z coordinates in the $+y$ rotational direction. The information of the final mesh for both sweep angles of zero and 22.5^0 is presented in Table 4.4, where $\Delta_{\min,n}/D$, $\Delta_{\max,s}/D$ and $\Delta_{\min,t}/D$ are the dimensionless minimum spacing in the radial, tangent in θ direction, and tangent along the centerline of the cylindrical fin, respectively.

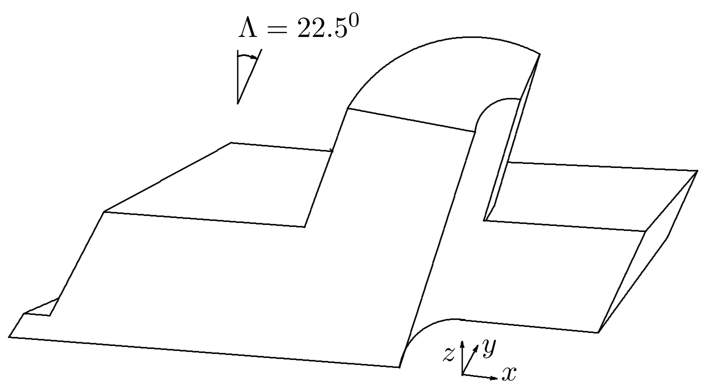

Figure 4.7: Computational Domain, 22.5^0 Sweep Angle

Table 4.4: Details of the Grids ($\Lambda = 0^0$ and 22.5^0)

No. of real cells	$\Delta_{\min,n}/D$	$\Delta_{\min,s}/D$	$\Delta_{\min,t}/D$
17,462,500	0.0014	0.0056	0.0108

The generation of the grid for the 45^0 sweep angle case is substantially more difficult compared to the other two cases, due to high non-orthogonality it has within its computational domain. The nonorthogonality adjacent to the solid walls and at the outflow with zero-gradient boundary condition is important due to the sensitivity of the solver code on this issue. As a result, 45^0 non-orthogonality is not acceptable and the grid for this case cannot be created by the same method that was used for the 22.5^0 sweep angle case.

There are two solid walls in two directions where the attempt to make the grid orthogonal should be made: the fin and the flat plate. Two independent continuous rotations of the mesh have been performed to get a more orthogonal mesh on the solid surfaces. The first rotation is relative to the fin, with centers of rotations fixed on the surface of the fin. Each radial series of grids are rotated relative to the grid at the fin by the criterion of the difference in the x coordinates. The angles of the rotation are linearly increasing from one layer of grids to the other. The final angle of rotation at each layer of each zone is editable by the user.

In this computational domain, there are 15 zones in the first layer (Figure 4.6), 14 zones (by omission of the zone number 15) in the next four layers, and 11 zones in the last 5 layers of zones. In the top layers, the zones number 1-6 and 10-14 (Figure 4.6) are built over the lower layers. Figure 4.8 presents the schematics of the computational domain and the zones as blocks, forming the computational domain. The rotation of each zone relative to the fin is apparent in the figure. The first five layers are rotated linearly from numbers obtained from the user. Inside the zones, the grids are rotated from the initial to the final angle of rotation linearly. In these calculations, the final angles of the rotation in five first layers are $\Omega_1 = 5^0$, $\Omega_2 = 12^0$, $\Omega_3 = 26^0$, $\Omega_4 = 37^0$, and finally, $\Omega_5 = \Lambda = 45^0$. The angle of rotation in top layers are constant at 45^0, making an orthogonal mesh relative to the fin at the center-plane.

The other solid surface that requires orthogonal grids at its vicinity is the flat plate. In the zones upstream the cylindrical fin, rotation of the grids has been performed with a second order polynomial function from centers of rotations located on the flat plate. The zones downstream the cylindrical portion of the fin are rotated by the same function from centers of rotations located on the top of the top layer of the computational domain. The reason for building the zones number 10-14 (Figure 4.6) is that at the outflow with zero-gradient boundary condition, orthogonal grid is needed and that could not be achieved without adding more zones downstream in the upper layers.

In this computational domain, the height of each layer is not constant and we have three groups of layers with three separate length chosen by the user. Moreover, the length M presented in Figure 4.6 at the top layer is 0.8. Table 4.5 presents some more detail of the grid spacing for this grid, where $\Delta_{\min,n}/D$, $\Delta_{\min,s}/D$ and $\Delta_{\min,t}/D$ are the dimensionless minimum spacing in the radial, tangent in θ direction, and tangent along the centerline of the cylindrical fin at the plate, respectively.

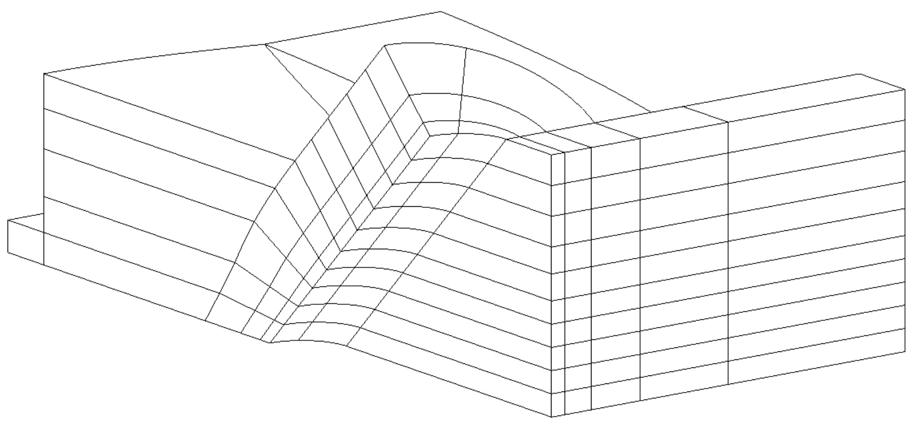

Figure 4.8: Computational Domain, 45^0 Sweep Angle

Table 4.5: Details of the Grids ($\Lambda = 45^0$)

No. of real cells	$\Delta_{\min,n}/D$	$\Delta_{\min,s}/D$	$\Delta_{\min,t}/D$
34,650,000	0.0014	0.0056	0.0062

Grid-Refinement Study

In order to show that the solution is independent of the grid spacing, a grid refinement study with finer grids should be performed. A selected criteria from the results should be compared with that of the coarser grids to show its independency on the grid spacing. The criterion used in this grid refinement study is the averaged heat transfer on the centerline of the fin. The zero degree sweep angle case with the strongest shock wave boundary layer interaction (described in the next chapter) has been chosen for the grid refinement study. It is sufficient to perform the grid refinement study on the zero degree sweep angle case, since it is the strongest interaction amongst all the sweep angle cases and it has the strongest dependency on the grid spacing.

Two additional levels of medium and fine grids were chosen to perform the grid refinement study. The schematics of the computation domains for both of the meshes is analogous to Figure 4.5 and the top view of the first layer of the grids is presented in Figure 4.9 with dimensions normalized by the diameter of the fin. In these computational domains we have one layer with 15, 10 layers with 14 and 8 layers with 6 zones. It has been shown in the previous studies [65] that in the fin-plate junction configurations, for the fin heights above twice its diameter, the fin can be considered semi-infinite. As a result, for convenience, only $2.36D$ of the height of the fin is simulated for the medium and fine levels of the grid instead of simulating the whole length of the computational domain.

More details of the computational domains of the medium and fine grids is presented in Table 4.6. In the medium level of the grid-refinement study, the spacing normal to the solid walls (n and t directions) have been reduced in half, and these spacings for the fine grid has been reduced by a factor of 2/3 from the previous level of the grid refinement study. The initial condition of the fine level of the grid refinement study has been estimated using first order interpolation of the results of the medium level.

Table 4.6: Details of the Grids for the Grid-Refinement Study ($\Lambda = 0^0$)

Grid	*No. of real cells*	$\Delta_{\min,n}/D$	$\Delta_{\min,s}/D$	$\Delta_{\min,t}/D$
Medium	28,014,000	7.5×10^{-4}	0.0056	0.0051
Fine	56,385,000	5×10^{-4}	0.0056	0.0033

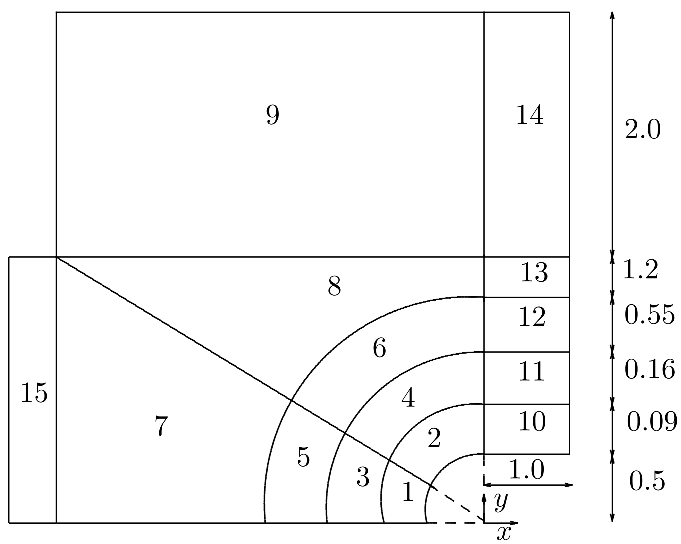

Figure 4.9: Top View of the First Layer, Grid-Refinement Study

Chapter 5

Results

5.1 Numerical Simulation of Adelgren *et.al.* Experiment

5.1.1 Steady State

In the simulation which models the Adelgren *et.al.* experiment [17] a steady state solution is achieved prior to the unsteady laser discharge. The steady state solution is reached when the relative residual dropped eight orders of magnitude for the inviscid model and three orders of magnitude for the viscous model. The normalized peak pressure and the surface skin fiction are the criteria for the grid refinement study for the inviscid and viscous models, respectively. The skin friction is normalized by the freestream velocity and density as follows.

$$c_f = \frac{\tau_w}{\frac{1}{2}\rho_\infty U_\infty^2} \tag{5.1}$$

The relative difference of the calculations of the maximum pressure and average of the skin friction on the surface of the hemisphere between the middle and fine grids are less than 0.2% and 10%, respectively. The Mach contours of the steady state condition in the viscous calculations is presented in Figure 5.1(a). The ratio of the freestream static pressure to the total pressure after the shock measured on the centerline for inviscid and viscous simulations and the shock stand off distance from the sphere surface agree with experimental results [17] within 1%, 4% and 4%, respectively. Additionally, the non-dimensional pressure in different angles on the sphere shows excellent agreement with the experimental data as described in the Figure 5.1(b) for the inviscid calculations.

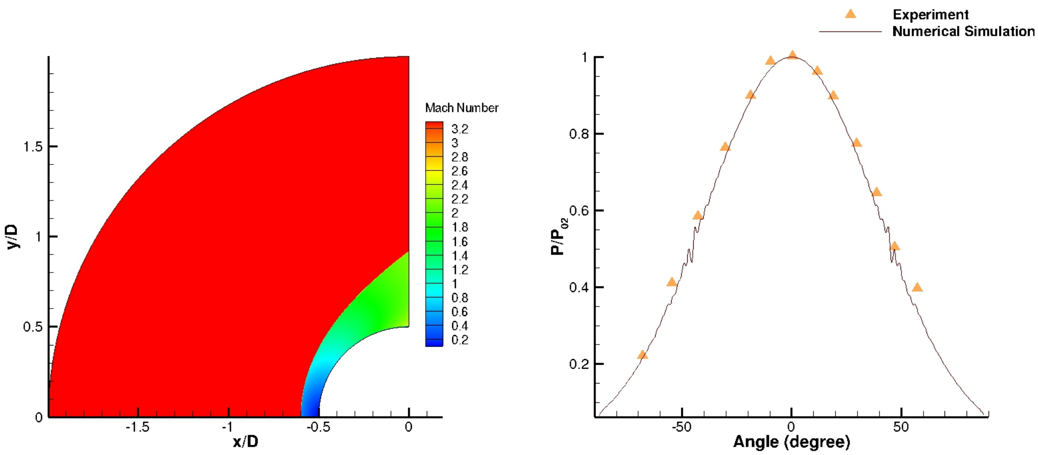

(a) Mach Number Contours (b) Numerical and Experimental Comparison

Figure 5.1: Steady State Solution

5.1.2 Flow Structure in Unsteady Simulation

In the next step, the laser discharge is modeled as an instantaneous uniform increase in static temperature (and pressure) in a spherical region superimposed on the steady state solution. The velocity and density at the instant of the laser discharge in the spherical heated region are equal to the freestream condition. The normalized radius of the plasma r_0/D is 0.05 and it is located one diameter from the hemisphere surface on the centerline in agreement with the experiment.

Figure 5.2 shows the Schlieren images at non-dimensional time τ where $\tau = tU_\infty/D$ and $\tau = 0$ corresponds to the instant of energy deposition. From the heated region a blast wave and expansion waves are formed and propagate radially outward and inward, respectively. The heated region convects with the flow and the pressure on the surface of the hemisphere rises as the blast wave reaches the surface (Figure 5.2(a)). The reflected shock from the surface of the hemisphere can be observed in Figure 5.2(b) and 5.2(c). Lensing forward of the blunt body shock is evident in Figure 5.2(d) where the heated region reaches the blunt body shock and changes the speed of sound in that region, moving the blunt body shock further to the upstream. Due to the Richtmyer-Meshkov instability [92],[93], toroidal vortices form downstream of the blunt body shock

(Figure 5.2(d) through 5.2(h)). These vortices and the expansion waves from the heated region reduce the pressure on the surface of the hemisphere. A secondary shock wave forms in the vicinity of the centerline and it impacts the centerline causing a secondary pressure jump in the centerline of the hemisphere. This secondary pressure jump is not captured in the experimental data (Figure 3.4), and is a physical consequence of the models chosen in these simulations. This secondary shock wave has been captured in numerical simulation of other research groups with the same geometric configuration of the model. Examples of these studies are the investigations performed by Azarova *et.al.* and Shulein *et.al.* [94],[95]. The heated region eventually convects with the flow past the hemisphere and the flow converges to the previous steady state condition.

(a) $\tau = 0.77$

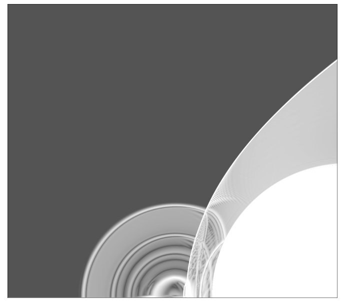

(b) $\tau = 0.86$

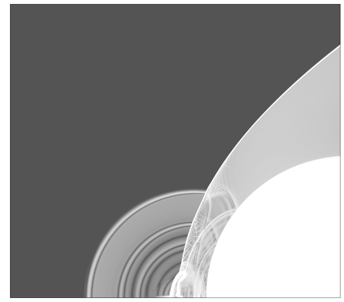

(c) $\tau = 0.96$

(d) $\tau = 1.06$

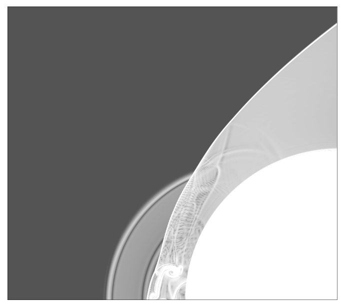

(e) $\tau = 1.20$

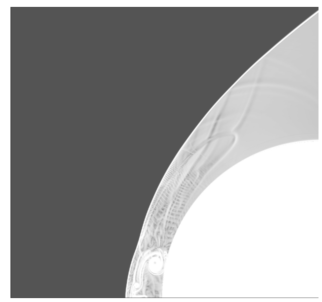

(f) $\tau = 1.44$

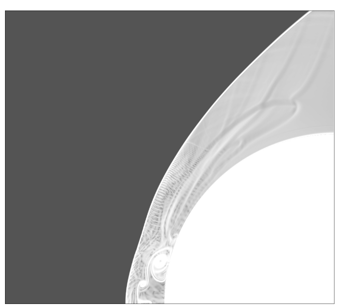

(g) $\tau = 1.68$

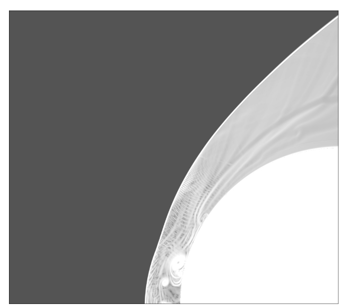

(h) $\tau = 1.92$

Figure 5.2: Schilieren Images for $Q = 258$ mJ

5.1.3 Drag Coefficient

The drag coefficient is defined as the non-dimensional force in the streamwise direction normalized with the freestream density and velocity and the frontal area of the sphere.

$$c_d = \frac{F}{\frac{1}{2}\rho_\infty U_\infty^2 A} \tag{5.2}$$

Figure 5.3 shows the history of the drag coefficient in the inviscid model for $\varepsilon_s = 1.178 \cdot 10^{-2}$ ($\Delta T/\ T_\infty = 9$ and $r_0/L = 0.05$) where $\tau = tU_\infty/D$ is the non-dimensional time. The drag coefficient increases at point B due to the interaction of the blast wave with the hemisphere surface. When the heated region reaches the hemisphere the drag coefficient drops considerably (point C) and later it converges to the steady state condition (point D). The whole process occurs in approximately three characteristic times (D/U_∞).

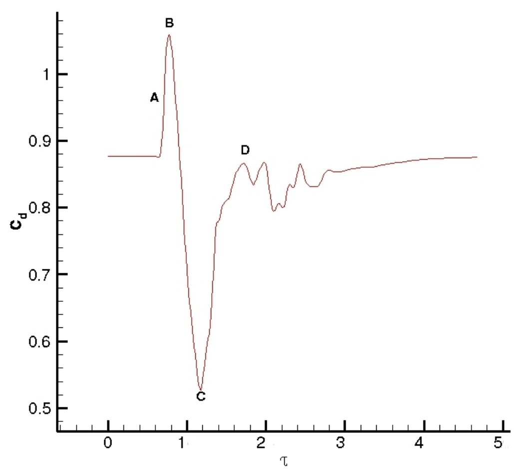

Figure 5.3: $c_d\ vs\ \tau$

The Mach number contours and some streamlines at points A through D are presented in Figure 5.4. At point A, the blast wave starts to interact with the hemisphere surface and the drag coefficient on the sphere increases due to this interaction. Point B is when the blast wave has its maximum effect on the hemisphere surface and the drag reaches its maximum. Since the static pressure relaxes rapidly, the heated region has the equal pressure and velocity to the freestream when it reaches the hemisphere. However, the temperature does not relax as quickly leading to a lower Mach number in the heated region. As a result, the total pressure in the heated region is less than the total pressure in the freestream when it reaches the hemisphere; therefore, the stagnation point moves upstream of the hemisphere surface when the heated region interacts with the blunt body shock (point B). The lower Mach number in the heated region causes the lensing of the shock which is apparent in point C. Due to this phenomenon the shock wave moves to the upstream increasing the stand off distance of the blunt body shock. The interaction of the heated region with the blunt body shock causes toroidal vortices due to the Richtmyer-Meshkov instability [92],[93] which reduces the pressure on the hemisphere surface (point C). Later on at point D, the heated region convects downstream and the flow converges back to steady state condition.

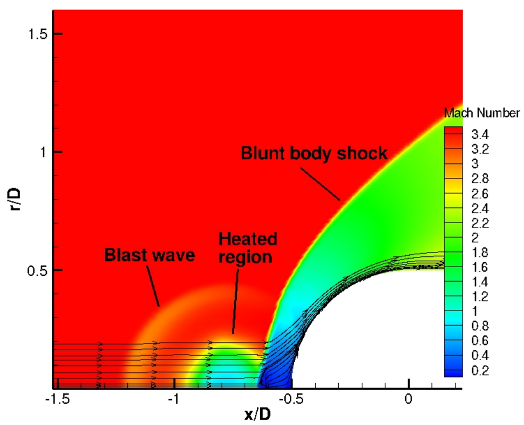

(a) Point A

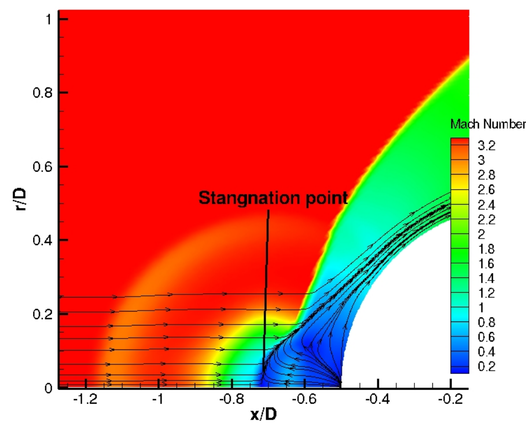

(b) Point B

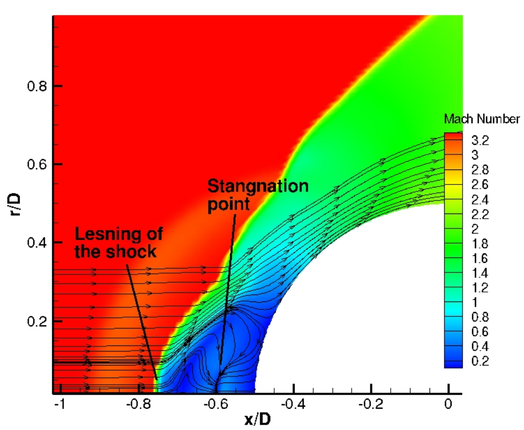

(c) Point C

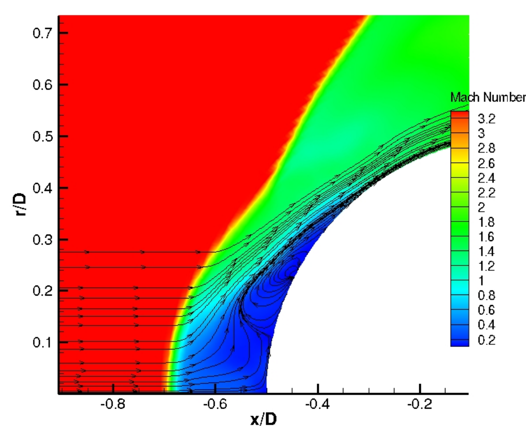

(d) Point D

Figure 5.4:

5.1.4 Comparison with Experiment

As indicated in Figure 3.4, the amount of energy deposited to the flow strongly affects the first pressure peak in the experimental pressure on the centerline of the hemisphere. As a result, by matching the first peak pressure in the numerical simulation to that of the experimental data we can determine the single empirical parameter $\Delta T/T_\infty$ (*i.e.*, the uniformly added temperature in the energy deposition region) in the laser energy deposition model (Equation (4.1)). We performed a series of simulations to determine $\Delta T/T_\infty$ to match the experimental result within 5%.

The change of the non-dimensional pressure centerline ($\Delta P/P_{02} = (p - p_{02})/p_{02}$) *vs* non-dimensional time ($\tau = tU_\infty/D$) for the inviscid and viscous models and the experiment for all three energy deposition cases are presented in Figures 5.5 through 5.7. The figures show very close agreement between the inviscid and viscous simulations, which shows that this phenomena is inviscid principally. This is due to the high Reynolds number in the viscous model ($Re = 1.7 \cdot 10^6$) which leads to a very thin boundary layer compared to the hemisphere diameter. Moreover, the nature of the Richtmyer-Meshkov instability is inviscid dominated and the location of observation of the pressure history at the centerline is not strongly dependent on the viscous effects.

Figures 5.5 through 5.7 display a significant difference between the experimental and numerical centerline pressure time history. The second high peak in the pressure observed in the numerical simulation is not seen in the experiment; however, it has been observed in numerical simulation of other research groups with hemisphere configuration [94]. The low peak pressure and the duration of the unsteady behavior in the numerical calculations do not match the experiment. Although qualitatively the influence of the blast wave and the interaction of the heated region with the blunt body shock is captured in the numerical models, the quantitative predictions lack accuracy.

The calculated thermal efficiency defined by Equation (4.4) and (4.9) is in the order of 1%. The laser pulse energy (measured at the laser exit in the experiment) is expended in 1) transmitted and reflected energy (*i.e.*, not absorbed by the air), and increase in the 2) translational-rotational temperature, 3) vibrational temperature, 4) electronic excitation, 5) dissociation and 6) ionization of the air in the focal volume [26]. In view of the discrepancies between the calculated and experimental centerline pressure time history, the calculated efficiency is not a reliable estimate.

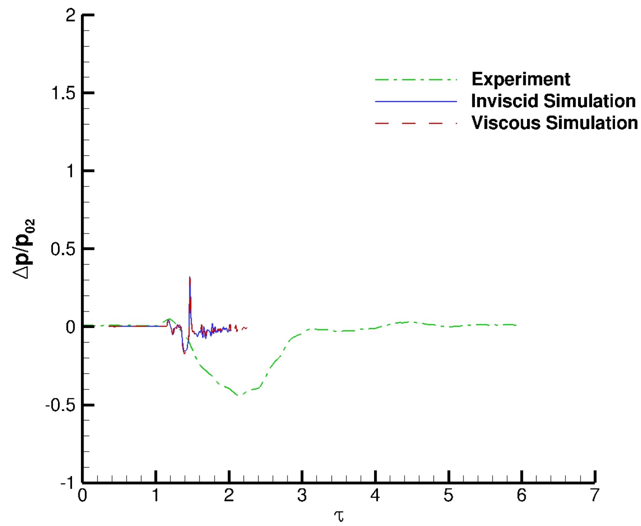

Figure 5.5: Q = 13 mJ

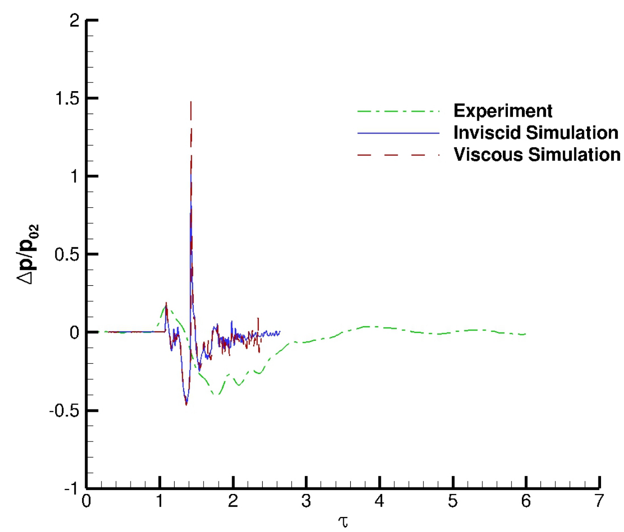

Figure 5.6: Q = 127 mJ

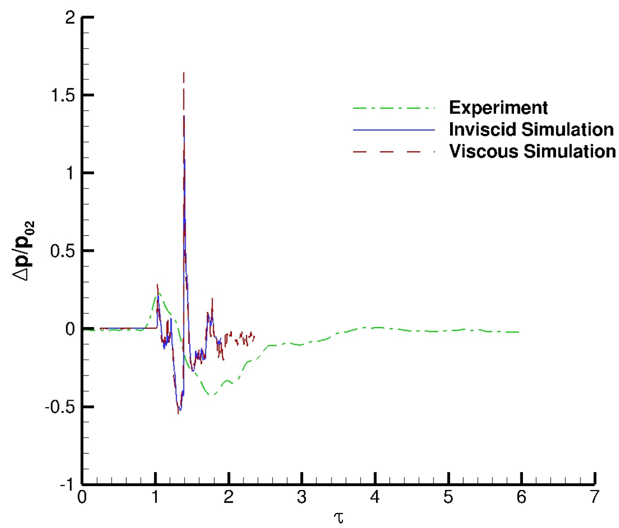

Figure 5.7: Q = 258 mJ

5.2 Numerical Simulation of Chanetz *et.al.* Experiment

In the numerical simulation of the experiment conducted by Chanetz *et.al.* [85] two dimensional axisymmetric shock wave boundary layer interaction in a hollow-cylinder configuration is studied. The results for the normalized density contours are described in Figure 5.8. A boundary layer displacement shock forms from the beginning of the sharp edge. The flare shock which forms over the flare imposes an adverse pressure gradient on the flow and separates the boundary layer. At the reattachment point of the boundary layer on the flare, a reattachment shock wave forms and meets the boundary layer displacement shock at the reattachment point where the pressure increases. The flare shock bends when it interacts with the expansion waves created from the edge of the cylinder downstream of the flare. The boundary layer displacement shock, the reattachment shock and the flare shock which coincide at the reattachment point are evident in the figure.

Figure 5.9 shows the pressure contours and the streamlines for this computation. The pressure in the contours is normalized using the freestream velocity and density. The separation point and the recirculation in the separated region can be detected using the streamlines. The figure shows that the highest pressure is at the reattachment point where the boundary layer displacement shock, reattachment shock and the flare shock meet, and the distance of the separation point from the junction of the flare and the cylinder is $x_{sep}/L = 0.16$.

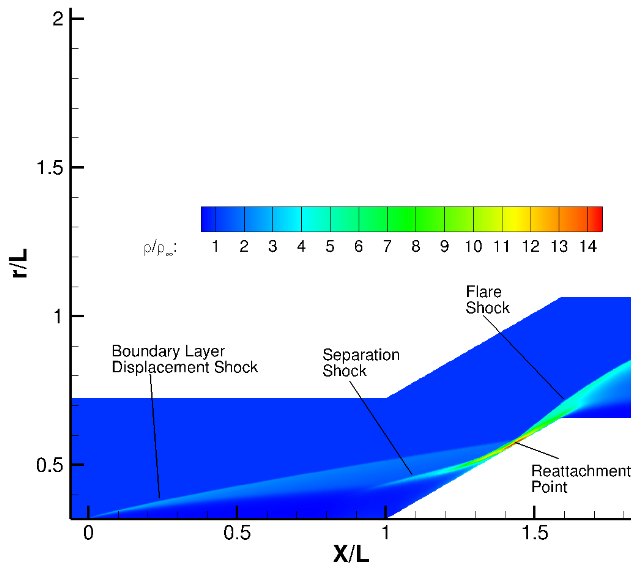

Figure 5.8: Normalized density Contours

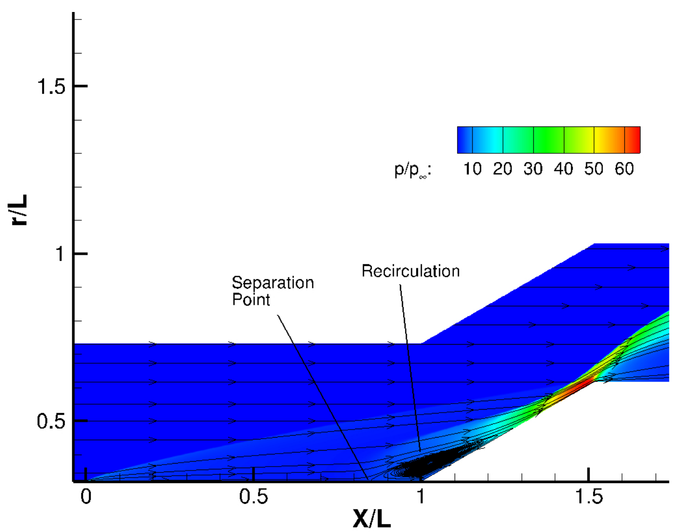

Figure 5.9: Normalized Pressure Contours

The Mach contours are presented in Figure 5.10. The recirculation region is evident with the streamlines plotted in the edge of the flare. The boundary displacement shock coincides with the flare shock and the reattachment shock at the reattachment point and creates a complex shock-shock interaction flow structure. Downstream of the flare and over the second cylinder a flow structure similar to a jet forms where the velocity is maximum between the flare shock and the wall of the cylinder and it decreases close to the wall and the flare shock. Figure 5.11 shows the normalized temperature contours. The temperature reaches its maximum over the flare; however, it decreases to the constant wall temperature at the boundary, causing a large temperature gradient and therefore large heat transfer on the flare.

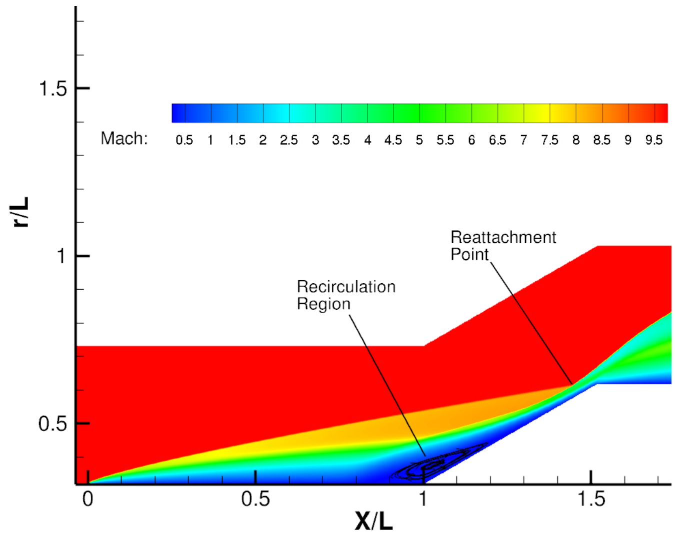

Figure 5.10: Mach Number Contours

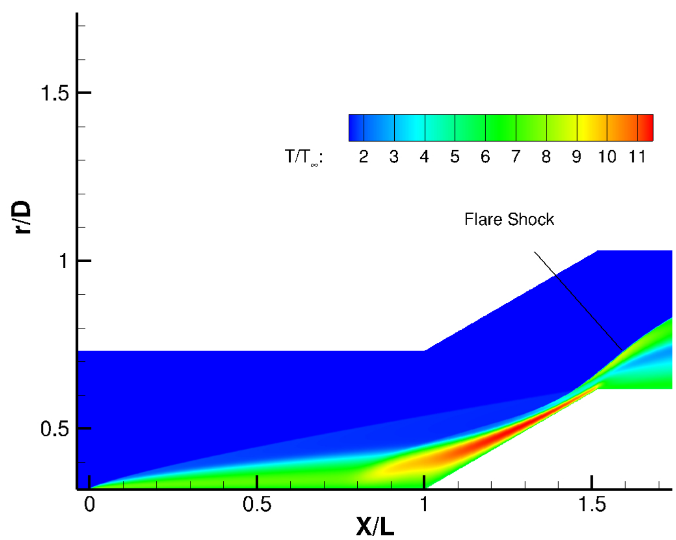

Figure 5.11: Normalized Temprerature Contours

Figure 5.12 presents the pressure coefficient for the numerical calculations and the experiment. The Stanton number -which is the normalized heat transfer on the wall- for the numerical and experimental simulations are presented in Figure 5.13. The pressure coefficient and the Stanton number are defined by the following equations.

$$c_p = \frac{p - p_\infty}{1/2 \rho_\infty U_\infty^2} \tag{5.3}$$

$$St = \frac{q_w}{\rho_\infty U_\infty c_p (T_{ust} - T_w)} \tag{5.4}$$

where q_w and T_w are the heat transfer and temperature at the wall, ρ_∞ and U_∞ are the freestream density and velocity, c_p is the heat capacity and T_{ust} is the upstream stagnation temperature.

At the leading edge of the cylinder the pressure increases due to the existence of the boundary layer displacement shock at that point. At the region where the shock waves interact with the boundary layer the pressure has two major rises; the first one is at the separation point and the other one is at the reattachment point. The pressure is almost constant in the recirculation region. The heat transfer is almost constant on the hollow cylinder and it increases on the flare reaching its maximum at the reattachment point. In this study, the pressure coefficients and the Stanton numbers of the numerical analysis are in good agreement with the experimental results.

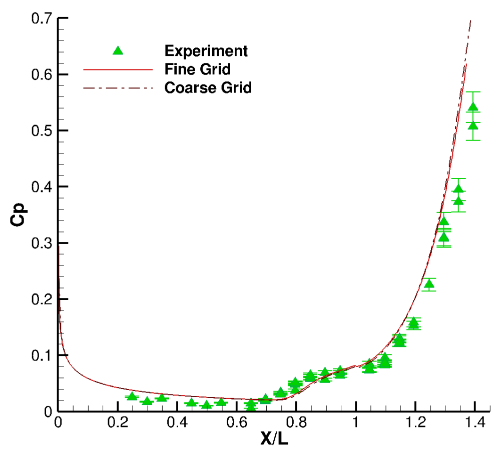

Figure 5.12: Pressure Coefficient

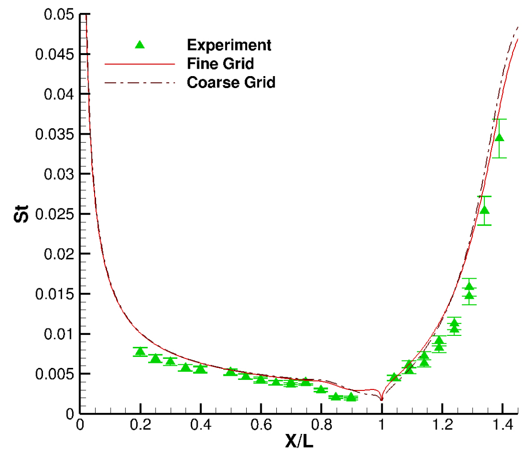

Figure 5.13: Stanton Number

5.3 Numerical Simulation of Hiers *et.al.* Experiment

The Mach number contours for the results of the calculations are presented in Figures 5.14 through 5.16. The complex flow structure of the shock wave boundary layer interaction is evident in the figures. Due to the viscous effects, a laminar boundary layer forms on the flat plate, which interacts with the strong blunt body shock wave upstream of the cylindrical fin. The strength of the blunt shock wave weakens as the sweep angle increases. The blunt body shock wave imposes an adverse pressure gradient, which separates the boundary layer and creates a lambda type shock wave structure. The influence of the pressure gradient travels within the subsonic region, increasing the separation size, until an approximate steady state is reached. It is evident from the Mach number contours that the separated region shrinks as the sweep angle increases, since the strength of the blunt fin shock wave and the adverse pressure gradient subsides as the sweep angle of the fin increases.

Figures 5.17 through 5.19 present the $log(p/p_{\infty})$ contours for the different sweep angle cases. The separation point and the blunt fin shock wave are evident in the figures. The separated boundary layer reattaches to the fin and creates a localized high pressure at the reattachment point. It is evident from the figures that the maximum pressure in the reattachment point on the fin surface decreases by increasing the sweep angle of the fin.

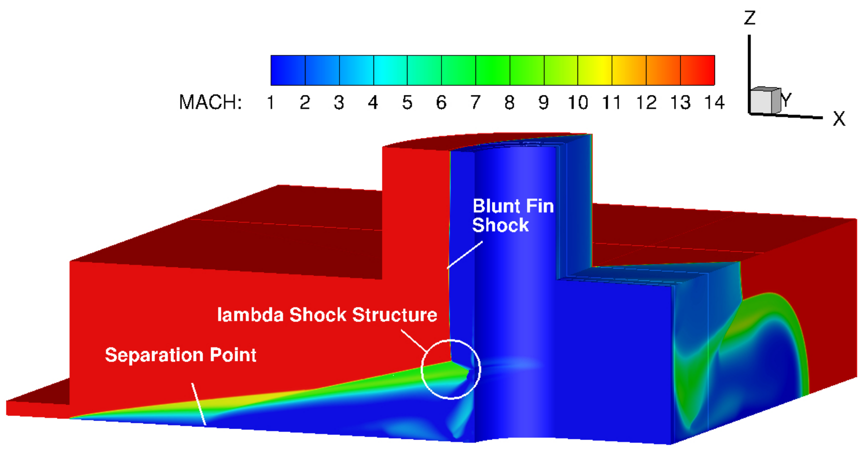

Figure 5.14: Mach Number Contours, $\Lambda = 0^0$ (Fine Grid)

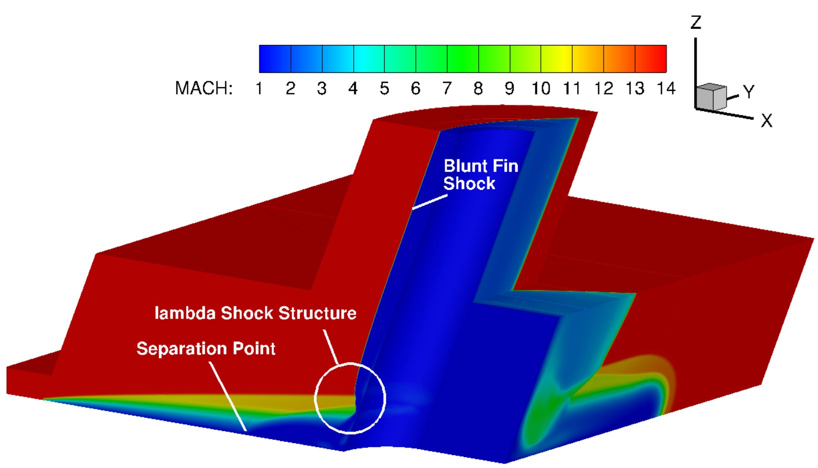

Figure 5.15: Mach Number Contours, $\Lambda = 22.5^0$

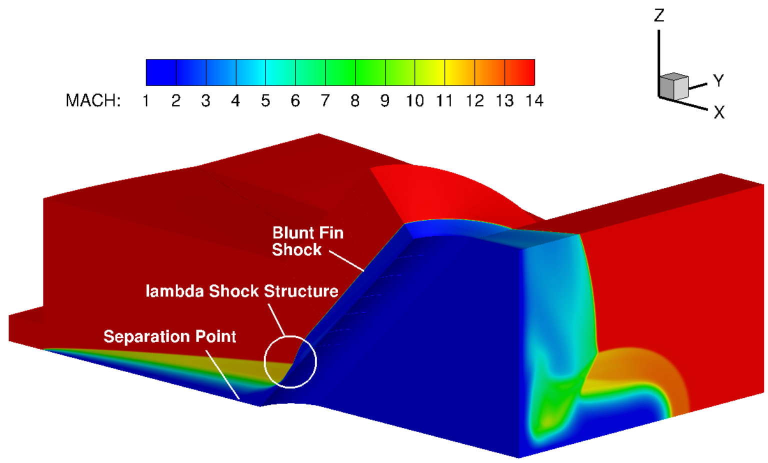

Figure 5.16: Mach Number Contours, $\Lambda = 45^0$

Figures 5.20 through 5.22 present the Mach number contours and the streamlines in the $y = 0$ plane for all the sweep angles, respectively. The figures identify the shock waves and their interactions in this study. A boundary layer displacement shock wave builds over the laminar boundary layer on the flat plate, with its angle independent of the separation size. The separation region for the zero degree sweep angle case takes more than 62% of the plate, while for the 22.5 and 45 degree cases this number reduces to 29% and 6%, respectively. This is due to the larger pressure gradient imposed by the stronger blunt fin shock waves in smaller sweep angle fins, which results in larger separation regions.

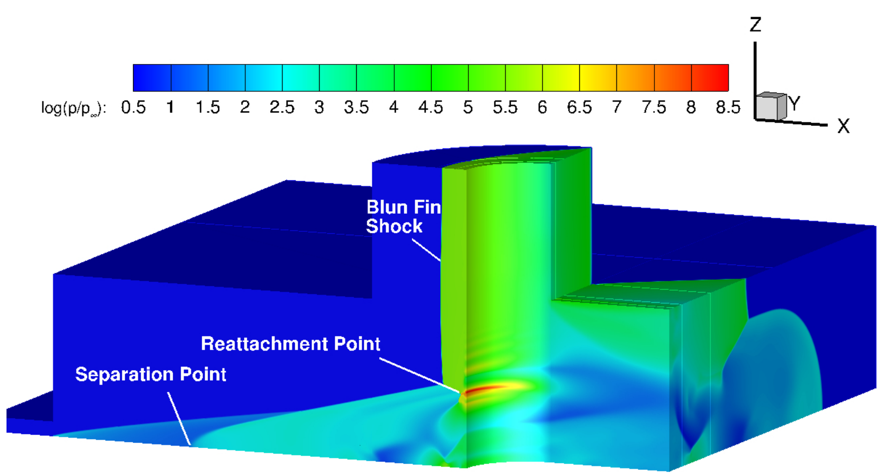

Figure 5.17: Pressure Logarithm Contours, $\Lambda = 0^0$ (Fine Grid)

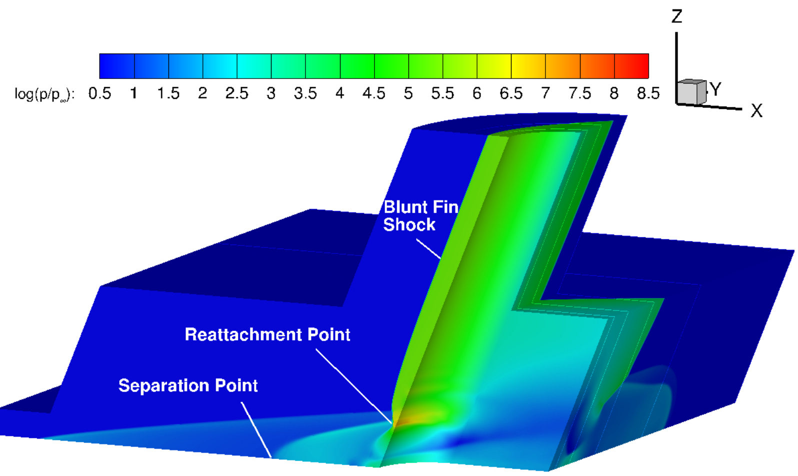

Figure 5.18: Pressure Logarithm Contours, $\Lambda = 22.5^0$

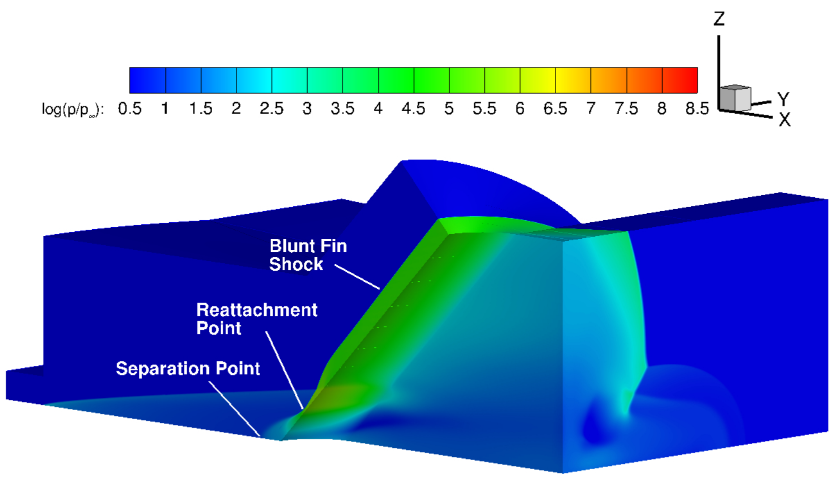

Figure 5.19: Pressure Logarithm Contours, $\Lambda = 45^0$

A separation shock wave forms over the separated region for the zero and 22.5 degree sweep angle cases, with its location and strength depending on the separation size. The extent of the recirculation region for the 45^0 sweep angle is so small, that there is no separation shock wave detectable in this case. Due to the larger separation region in the zero degree sweep angle case, the separation shock wave of this case intersects the boundary layer displacement shock ahead of the blunt fin shock wave. However, in the 22.5^0 sweep angle case, the separation shock wave forms below the boundary layer displacement shock wave, leading to two separate shock/shock interactions; one of them is the weak interaction of the boundary layer displacement shock wave and the blunt fin shock wave, and the other is the stronger interaction of the separation and the resultant transmitted shock waves. However, in the zero degree case, the separation shock wave interacts the displacement thickness shock wave prior to intersecting the blunt shock wave.

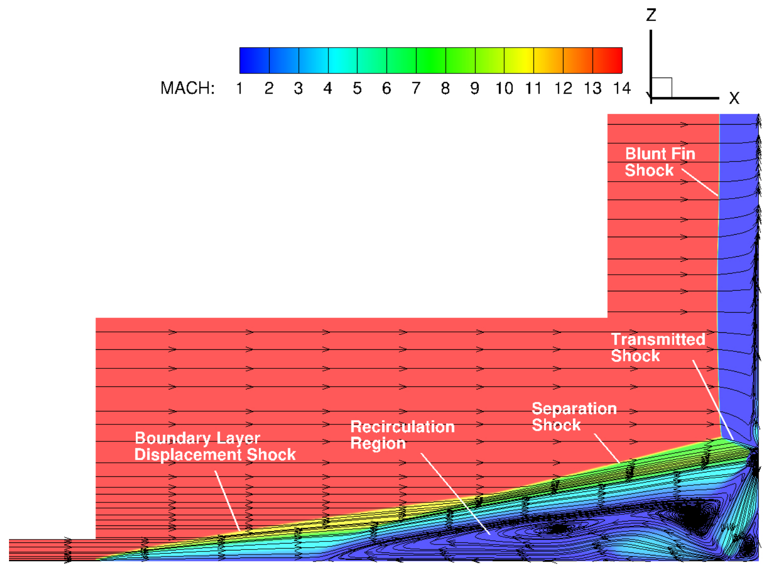

Figure 5.20: Mach Number Contours, $y = 0$ Plane, $\Lambda = 0^0$, (Fine Grid)

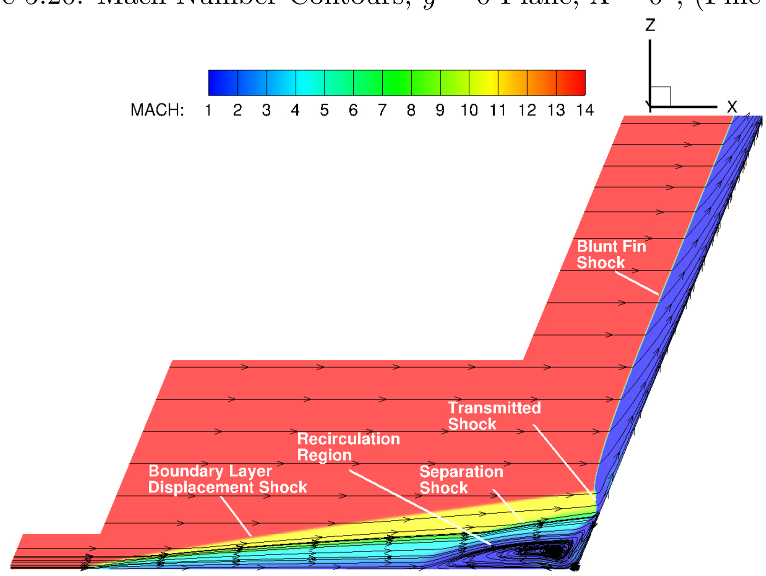

Figure 5.21: Mach Number Contours, $y = 0$ Plane, $\Lambda = 22.5^0$

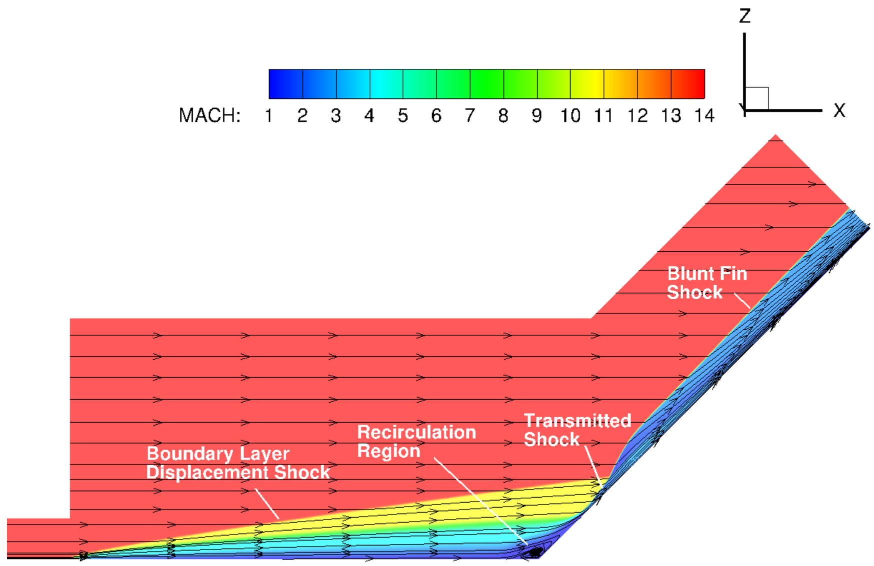

Figure 5.22: Mach Number Contours, $y = 0$ Plane, $\Lambda = 45^0$

The separation of the boundary layer results in formation of a primary horseshoe vortex with one or more secondary vortices. This phenomenon has been seen in subsonic, supersonic and hypersonic flows [96] . Figures 5.23 through 5.25 present the temperature contours and some streamlines at the center-plane of the computational domain. The separated region in this study contains upto four vortices depending on the sweep angle of the fin. The small secondary vortex is generated by the recompression from the supersonic to subsonic layer near the plate.

Moreover, the sonic lines and the Mach number contours are presented in Figures 5.26 through 5.28, where there are distinct supersonic areas inside the separated region for the zero and 22.5 degree sweep angle calculations. As the high momentum fluid accelerates in the horseshoe vortices, it forms low pressure supersonic reversed flow that can be detected from the Figures 5.26 and 5.27. Due to the very small extent of the separation region in the 45^0 sweep angle case, there is no supersonic reversed flow in the recirculation region in those calculations (Figure 5.28); However, there is a shear layer separating two regions of highly rotational viscous dominated subsonic sublayer and a supersonic inviscid dominated flow below the separation shock wave. Analogous flow structures with such slip lines have been encountered in other studies [63].

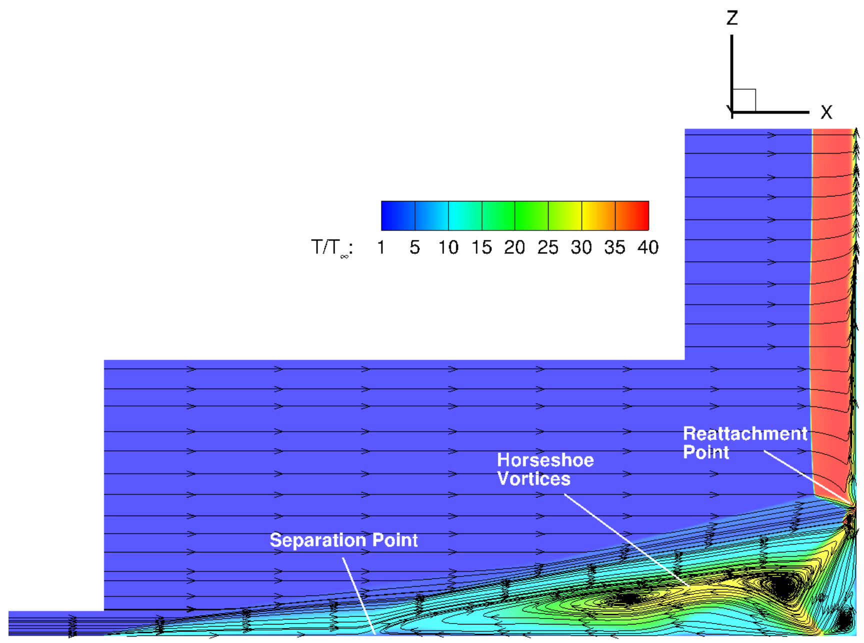

Figure 5.23: Static Temperature, $\Lambda = 0^0$ (Fine Grid)

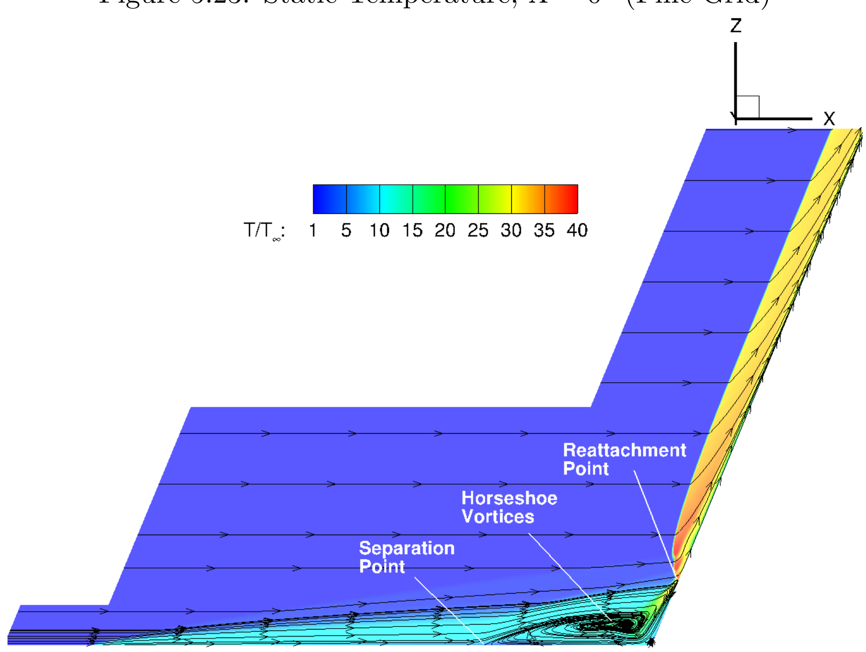

Figure 5.24: Static Temperature, $\Lambda = 22.5^0$

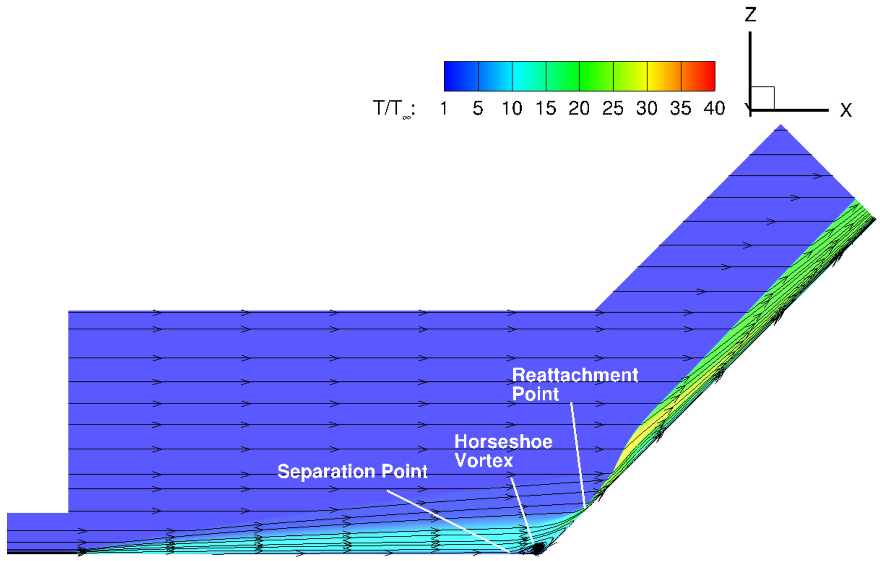

Figure 5.25: Static Temperature, $\Lambda = 45^0$

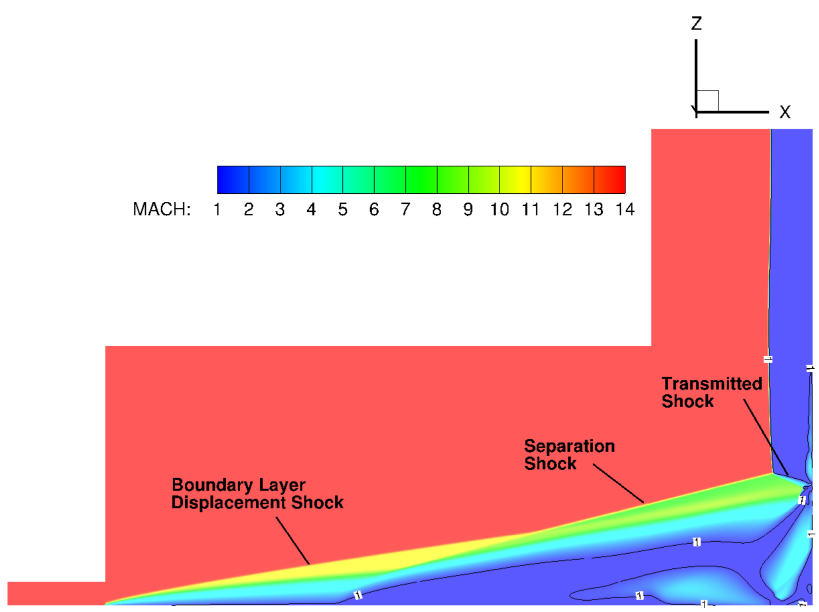

Figure 5.26: Mach Number, $\Lambda = 0^0$ (Fine Grid)

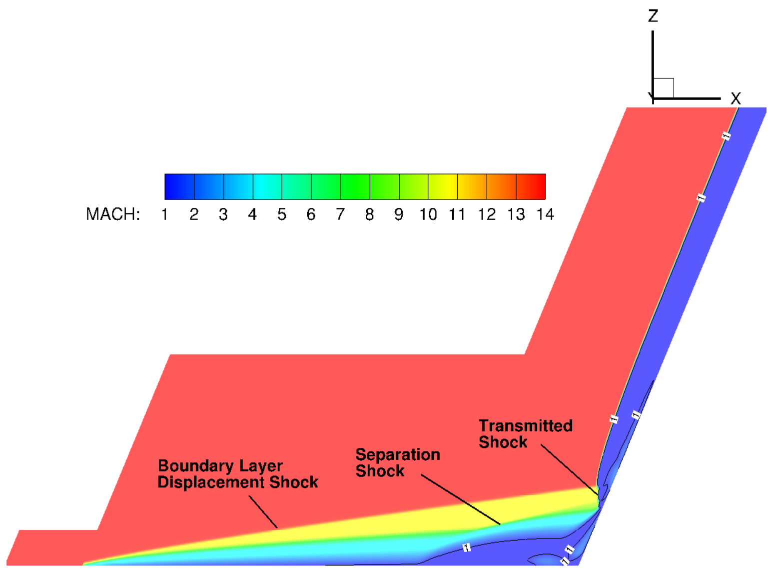

Figure 5.27: Mach Number, $\Lambda = 22.5^0$

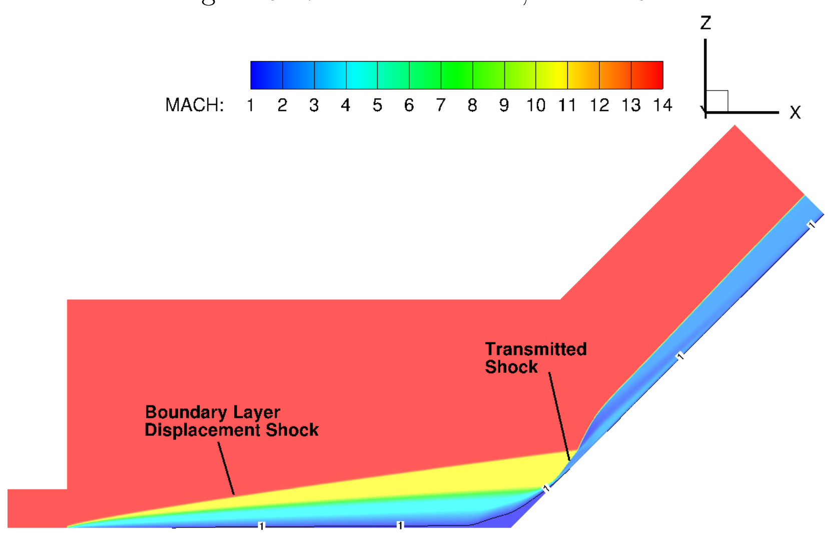

Figure 5.28: Mach Number, $\Lambda = 45^0$

Figures 5.29 through 5.31 present the shadow-graph at the center-plane for all the sweep angle cases. The boundary layer displacement, separation, reattachment, transmitted and blunt fin shock waves are evident from the figures. The faded rectangles and parallelograms do not have a physical representation and are the separate zones in the grid that the data visualization software (tecplot) could not blend well enough with the neighboring zones. The complex shock wave structure inside the separated region -especially for the zero degree sweep angle case- is evident from the figures.

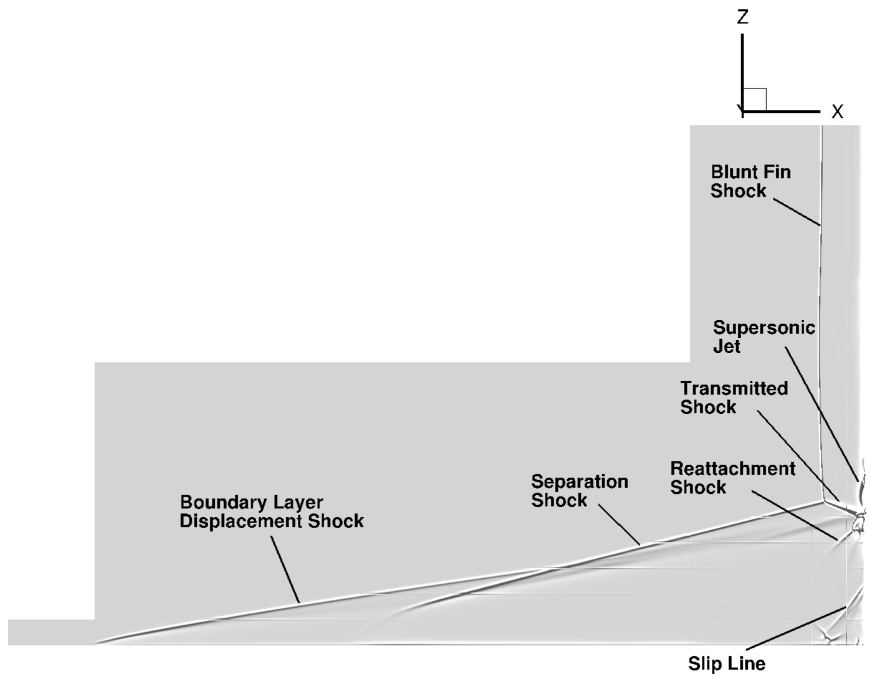

Figure 5.29: shadowgraph, $\Lambda = 0^0$ (Fine Grid)

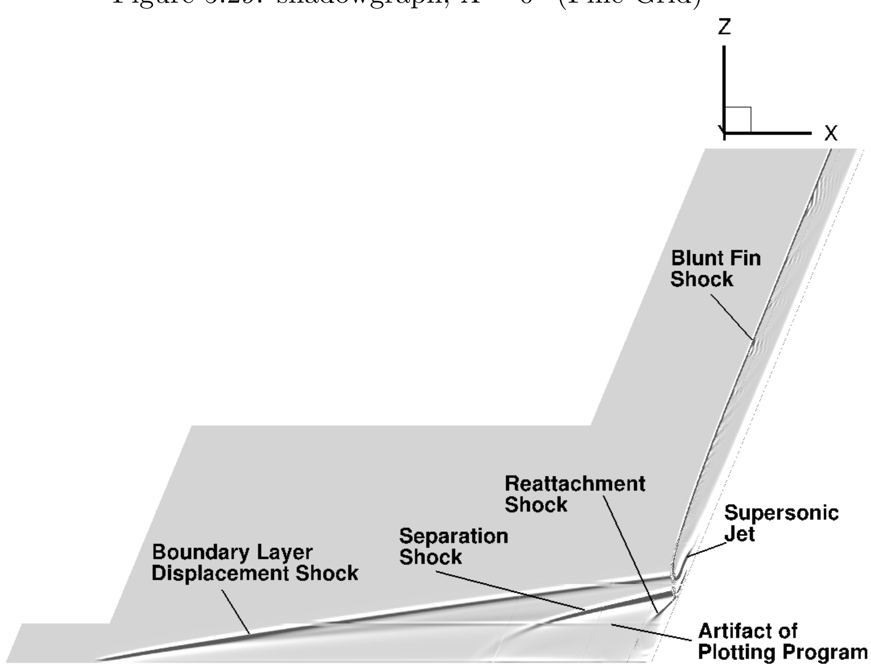

Figure 5.30: shadowgraph, $\Lambda = 22.5^0$

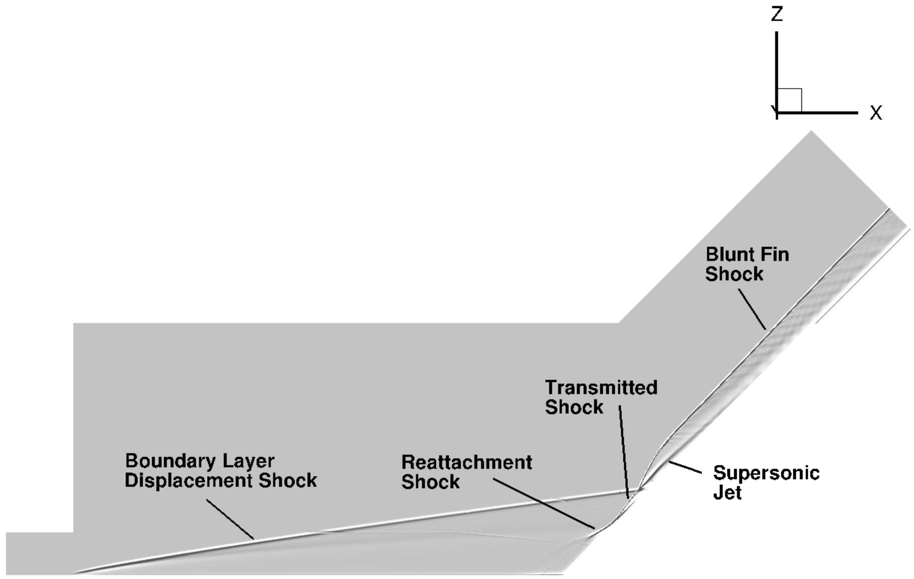

Figure 5.31: shadowgraph, $\Lambda = 45^0$

Figure 5.32 through 5.34 present the schlieren images on the centerline of the computational domain zoomed at the interaction region. A nearly normal shock wave can form at the interaction of two strong shock waves, which is referred to as the Mach reflection or Mach stem [30]. This phenomenon is captured at the interaction of the transmitted and the reattachment shock waves for the zero and 22.5 degree sweep angle cases (Figures 5.32 and 5.33). Since the strength of the shock waves subside in the 45^0 sweep angle case, the Mach reflection has disappeared in those results (Figure 5.34). A small secondary vortex forms downstream the Mach reflection in the zero degree sweep angle case, which influences the pressure and heat transfer prior to the reattachment point. This secondary vortex is detectable in Figure 5.32 by presentation of some streamlines in the separated region.

The Mach reflection oscillates leading to change in pressure and heat transfer close to the interaction region. Moreover, the slip-lines and the shock waves inside the separated boundary layer presented in the center-plane contours display temporal oscillations. The unsteady behavior rapidly subsides in the 22.5^0 and even more in the 45^0 sweep angle cases. Due to the large perturbation caused by the flow separation in the zero degree sweep angle case, another characteristic of these simulations, which is the unsteady oscillations at the interaction region arises.

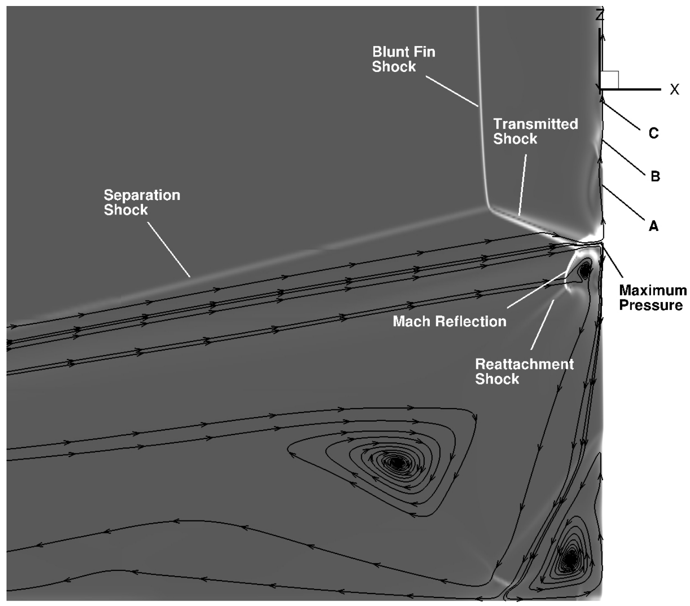

Figure 5.32: Schlieren Images, $\Lambda = 0^0$ (Fine Grid)

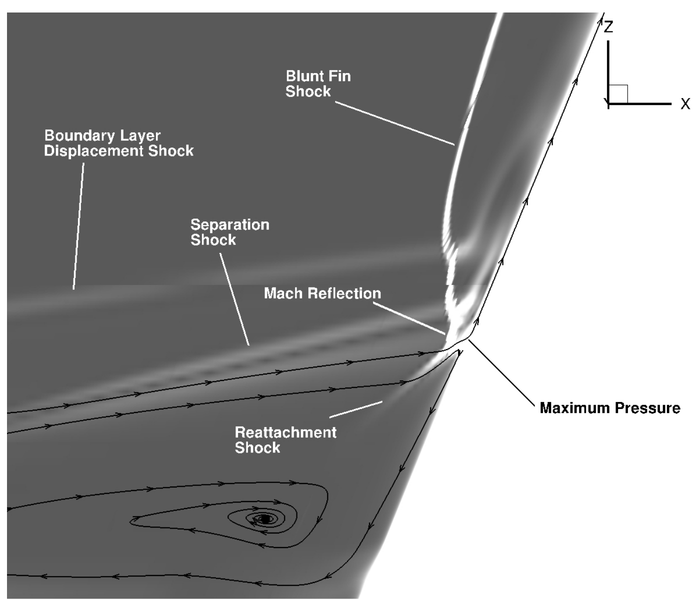

Figure 5.33: Schlieren Images, $\Lambda = 22.5^0$

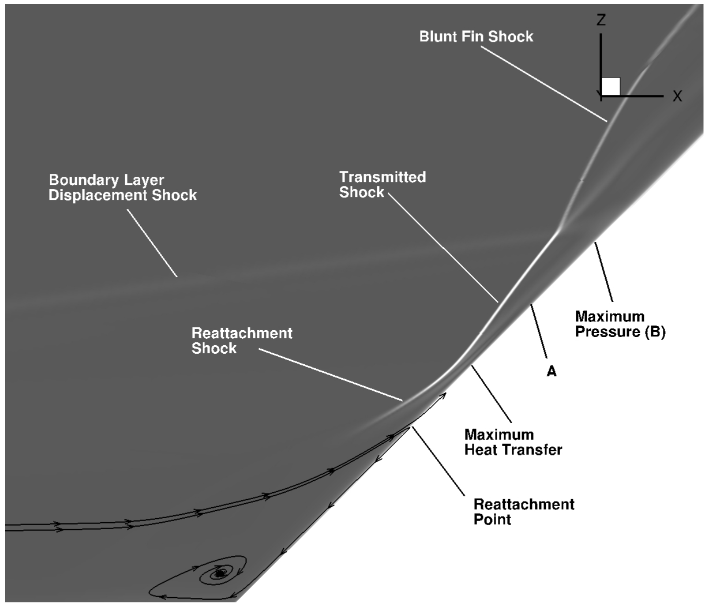

Figure 5.34: Schlieren Images, $\Lambda = 45^0$

Moreover, the supersonic jet flow downstream the blunt fin captured in Figures 5.26 through 5.28 contain compression and expansion waves. As the compression waves interact with the sonic line, they reflect as expansion waves. These expansion waves decrease the pressure on the fin as they interact with it. The expansion waves later reflect from the fin and interact with the sonic line and reflect from the sonic line as compression waves. The compression waves increase the pressure on the fin. As a result, we have oscillation of pressure on the fin as the expansion and compression waves interact with it. This phenomenon is evident from the plots of pressure on the centerline, which are presented in Figures 5.35(a) through 5.35(c). The local extrema of the pressure on the centerline of the fin have been labeled as A through C in Figures 5.32 and 5.35(a) for the zero degree sweep angle case calculations. The local minimum pressure prior to the global maximum in the zero degree sweep angle case, corresponds to the effect of the core of the small secondary vortex downstream the Mach reflection (Figure 5.32). The maximum pressure in the zero degree sweep angle case corresponds to the stagnation point of the flow at the reattachment point. On the other hand, the reattachment shock wave interacts with the blunt fin in the 22.5 degree sweep angle case, causing the maximum peak pressure. The strength of the reattachment shock wave and the peak pressure drastically decrease for the 22.5 and even more in the 45 degree sweep angle cases, compared with the zero degree case. The maximum pressure in the 45^0 sweep angle calculations corresponds to the interaction of the resultant shock wave formed from the impingement of the transmitted and the reattachment shock waves and the slip line generated at the interaction of the blunt fin and the boundary layer displacement shock waves. The maximum heat transfer, on the other hand, corresponds to the location of the minimum boundary layer thickness at the reattachment point for all the three cases calculated in these simulations (Figure 5.34).

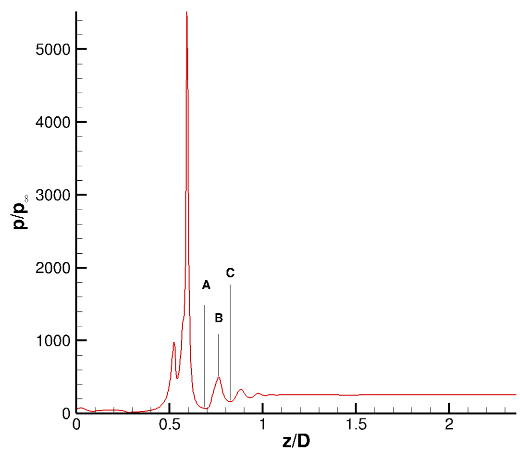

(a) $\Lambda = 0^0$ (Fine Grid)

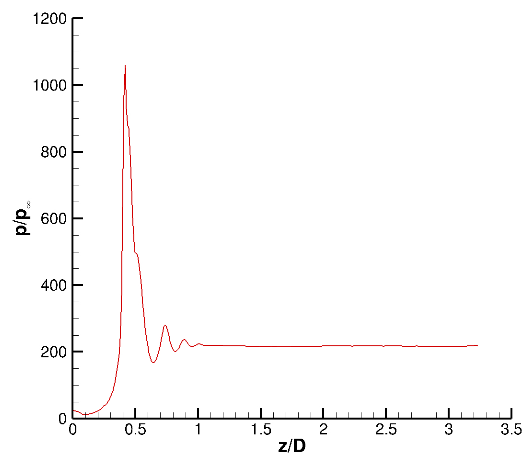

(b) $\Lambda = 22.5^0$

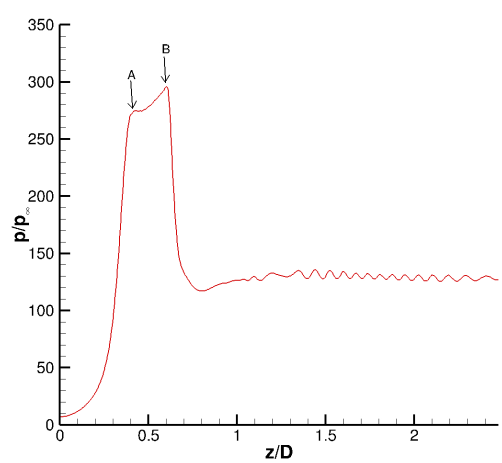

(c) $\Lambda = 45^0$

Figure 5.35: Normalized Pressure on the Centerline of the Fin

The shock wave boundary layer interaction in this study is highly three-dimensional. Figures 5.36(a) through 5.36(c) present the shadowgraph of the three-dimensional shock wave surface in the computational domain. The shock wave over the separated boundary layer and the blunt fin shock wave are evident. At the exit of the computational domain a complex structure of shock waves and slip-lines are captured (Figures 5.37(a) through 5.37(c)). The blunt fin shock wave interacts with the boundary layer through the three dimensional domain and a three dimensional transmitted shock wave forms from this interaction. The transmitted shock wave is evident in the shadow-graphs at the end of the computational domain. Moreover, some streamlines at the vicinity of the center-plane are presented in Figures 5.38(a) through 5.39 to show the structure of the streamlines inside the separated region in a three-dimensional perspective. It can be seen from these figures that the extent of the separated region drastically decreases by increase in the sweep angle of the fin.

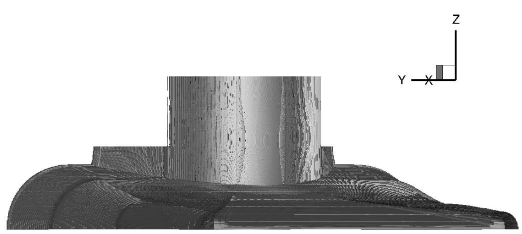

(a) $\Lambda = 0^0$ (Fine Grid)

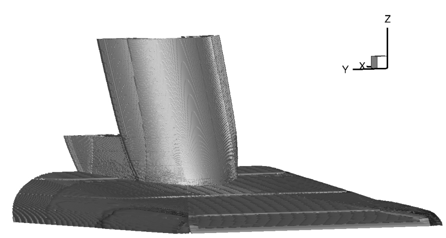

(b) $\Lambda = 22.5^0$

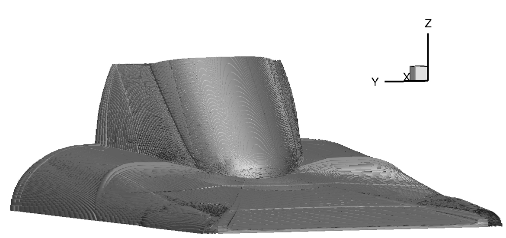

(c) $\Lambda = 45^0$

Figure 5.36: Iso-Surface of Shadowgraph

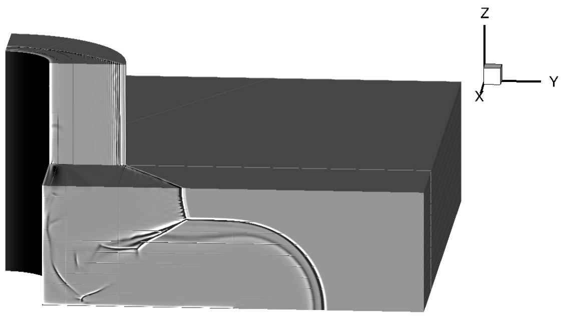

(a) $\Lambda = 0^0$ (Fine Grid)

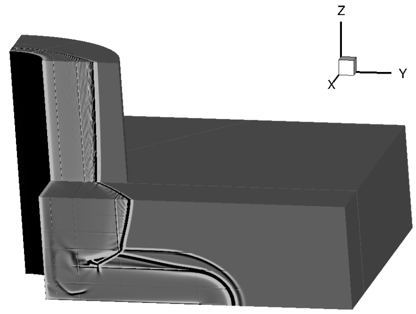

(b) $\Lambda = 22.5^0$

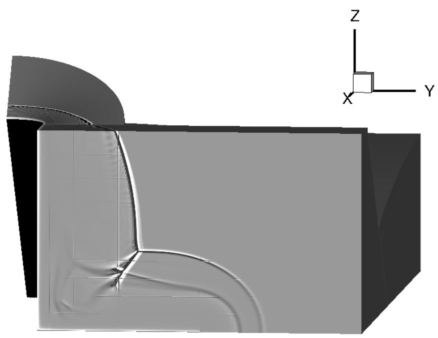

(c) $\Lambda = 45^0$

Figure 5.37: Shadowgraph

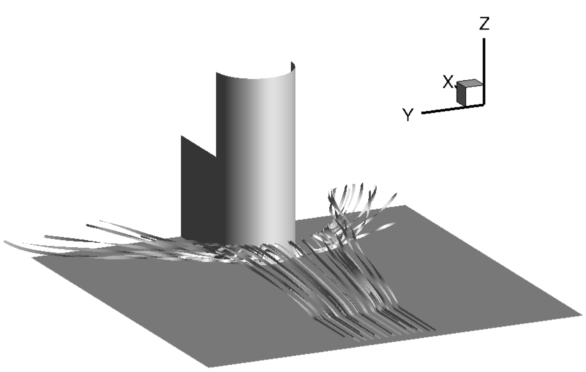

(a) $\Lambda = 0^0$ (Fine Grid)

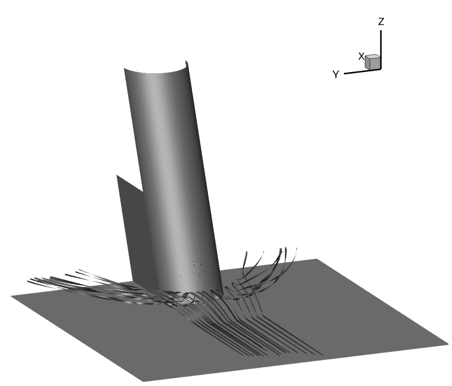

(b) $\Lambda = 22.5^0$

Figure 5.38: Three-Dimensional Streamlines

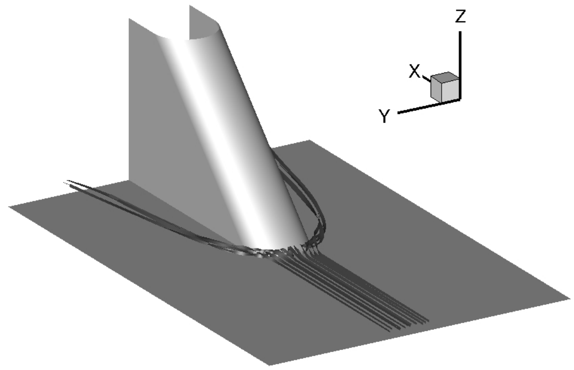

Figure 5.39: Three-Dimensional Streamlines, $\Lambda = 45^0$

Streamlines inside the three vortices for the zero degree sweep angle case, in the coarse level of the grid, are presented in Figure 5.40, where we can see that the core of the vortices incline away from the flat plate due to the existence of the boundary layer, which pushes the vortices upwards. Moreover, we can see that the area of the cross section of the vortex tubes are shrinking as they move to the downstream due to second Helmholtz Vortex Theorem [97], which states that the circulation at each cross section of the vortex tube should stay constant. In this problem, the velocity, and therefore vorticity of the fluid increases as the fluid moves away from the vertical center-plane, leading to smaller cross section in the vortex tubes.

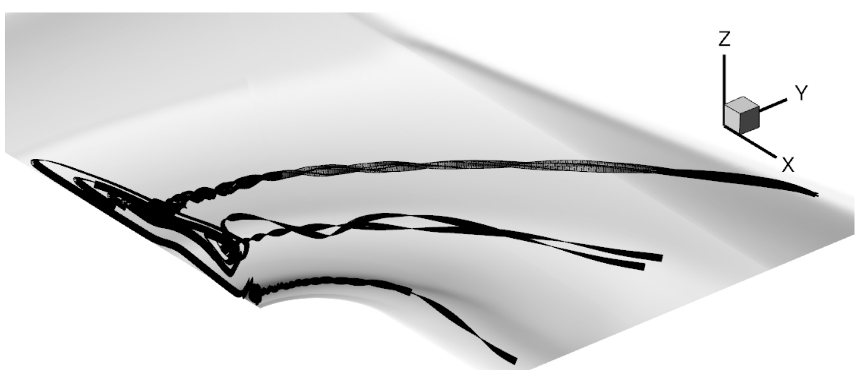

Figure 5.40: Three Dimensional Streamlines Inside Vortices, $\Lambda = 0^0$

The surface skin friction lines on the solid surfaces together with the pressure contours are presented in Figures 5.41(a) through 5.3. Low pressure region in zero and 22.5 degree sweep angle cases are detected (Figures 5.41(a) and 5.41(b)), which correspond to supersonic revered flow in the recirculation region. Since the shock wave boundary layer interaction in the zero degree sweep angle case is stronger and the extent of the separation region is larger compared with the other two cases, more vortices are detected in this case. From the pattern of the skin friction lines we can identify ten singular points in the zero degree sweep angle case with five nodes and five saddle points (Figure 5.41(a)); where as in the 45 and 22.5 degree cases we have four and two singular points presented in the Figures 5.41(b) and 5.3. Nodes are defined as singular points with all trajectories pointed either towards or away from them. On the other hand, saddle points have two characteristic directions; through one, the trajectories point towards the singular point, and through the other direction they point away from the saddle point. If the surface skin friction lines point away from the node, that point is an attachment node [98]. We can see that all the nodes in all of the cases are attachment points with surface skin friction lines pointing away from them. Moreover, the global separation line is evident from the first saddle point, directing away from it.

The surface heat transfer on the solid surfaces with dimension of kW/m^2 are presented in Figures 5.43(a) through 5.44. The adverse pressure gradient imposed by the smaller sweep angle fins is stronger than that of the larger cases, resulting to a more severe interaction. This results in increase in the maximum heat transfer and the size of the separated region by decrease in the sweep angle of the fin. This effect is evident in all of the graphs and contour plots as well as the surface skin friction lines.

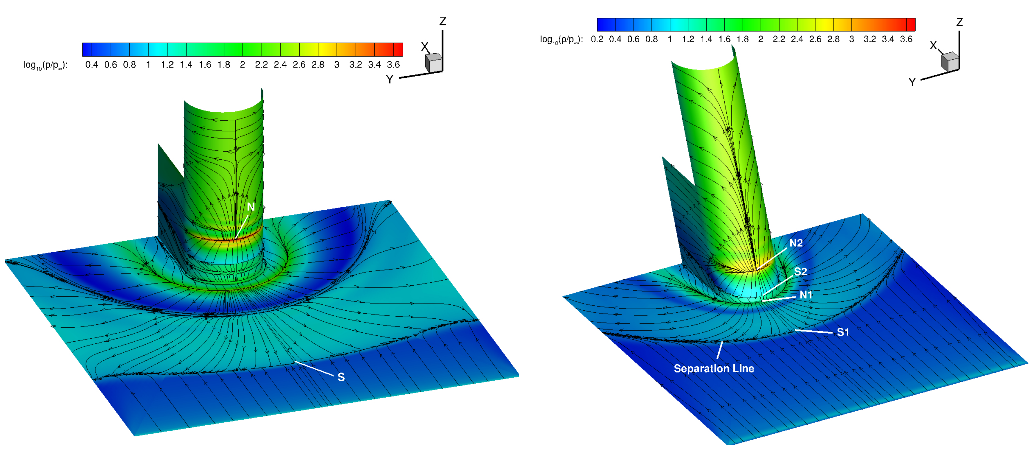

(a) $\Lambda = 0^0$, (Fine Grid)

(b) $\Lambda = 22.5^0$

Figure 5.41: Skin Friction and Logarithm 10 of Pressure

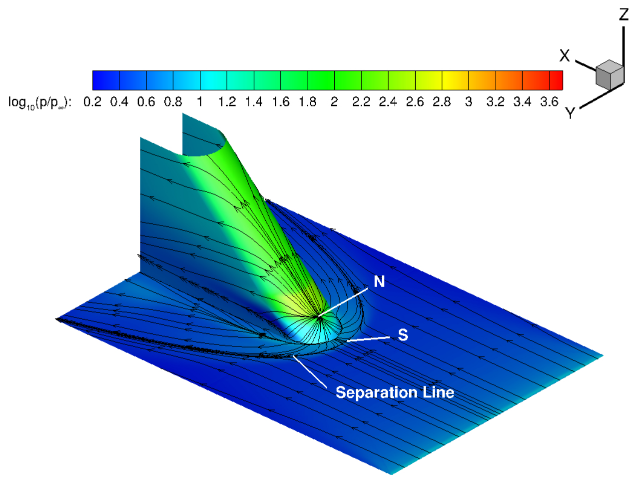

Figure 5.42: Skin Friction and Logarithm 10 of Pressure, $\Lambda = 45^0$

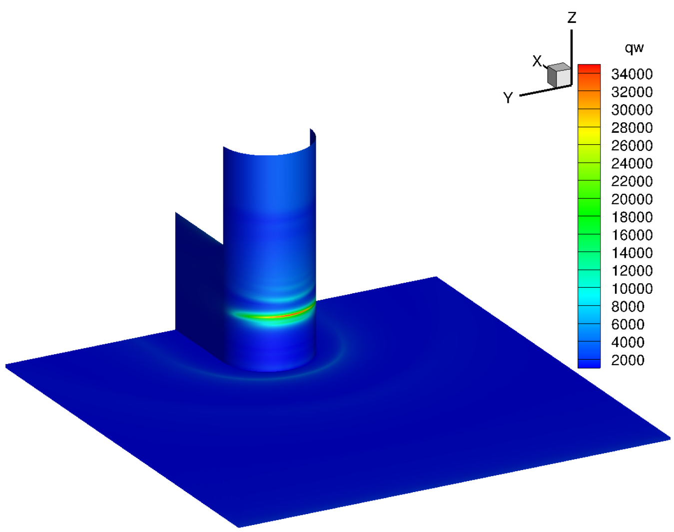

(a) $\Lambda = 0^0$, (Fine Grid)

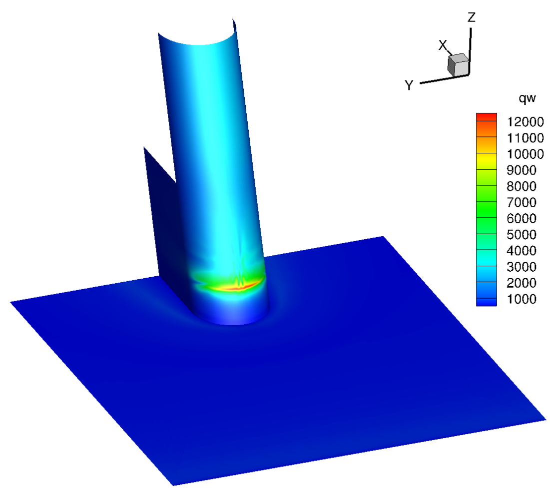

(b) $\Lambda = 22.5^0$

Figure 5.43: Skin Friction and Heat Transfer

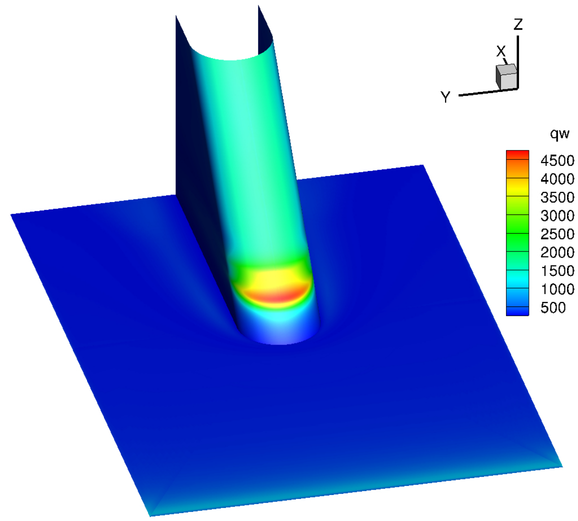

Figure 5.44: Skin Friction and Heat Transfer, $\Lambda = 45^0$

Figures 5.45(a) and 5.45(b) present the non-dimensional pressure history, normalized by the freestream pressure for the zero (coarse grid) and 22.5 degree sweep angle cases at the fixed locations of $z/D = 0.3016$ and $z/D = 0.4079$ on the center-plane, respectively. These locations are chosen where the most oscillation was captured to study the unsteady behavior of the flow. Time is normalized by the diameter of the blunt fin and the freestream velocity. Moreover, non-dimensional heat transfer history for the zero (coarse grid) and 22.5 degree sweep angle cases at the fixed locations of $z/D = 0.3016$ and $z/D = 0.4079$ on the center-plane are presented in Figures 5.46(a) and 5.46(b), respectively. Although the heat transfer history for the 22.5^0 sweep angle case is larger than that of the zero degree case, it does not necessarily represent the maximum heat transfer on the fin. The observation of the pressure and heat transfer was intended to study the unsteady behavior, and the location chosen to do so was not at the exact location of the maximum aerothermodynamic loads for either of the cases.

The heat transfer is normalized by the stagnation point heat transfer calculated on the nose of the blunt fin away from the interaction region in the zero degree sweep angle case. Since the heat transfer calculations at hypersonic speeds are highly dependent on the grid spacing, it is important to normalize the heat transfer at each computational domain with the corresponding stagnation point heat transfer calculated at the same level of the grid spacing. The stagnation point heat transfer in the coarse, medium and fine grids are 3.09, 3.31 and 3.35 MW/m^2, respectively. The calculations of the heat transfer for the 22.5 and 45 degree sweep angle cases are normalized by the stagnation point heat transfer, calculated at the coarse grid for the zero degree sweep angle case.

Great decay in the unsteady behavior is observed for both pressure and heat transfer history for the 22.5^0, compared with the zero degree sweep angle case. The decay in the unsteady behavior for the 45 degree sweep angle case is even more considerable. The relative peak to peak variations in the pressure for the 22.5 degree case has decreased compared with the zero degree case approximately from 70% to 2%; and for the heat transfer rate this number has decreased approximately from 25% to 3%. The relative peak to peak variations for the 45 degree sweep angle case for both heat transfer and pressure calculations are in the order of 0.01%. It can be concluded that the unsteady oscillations rapidly decline by increase in the sweep angle of the fin.

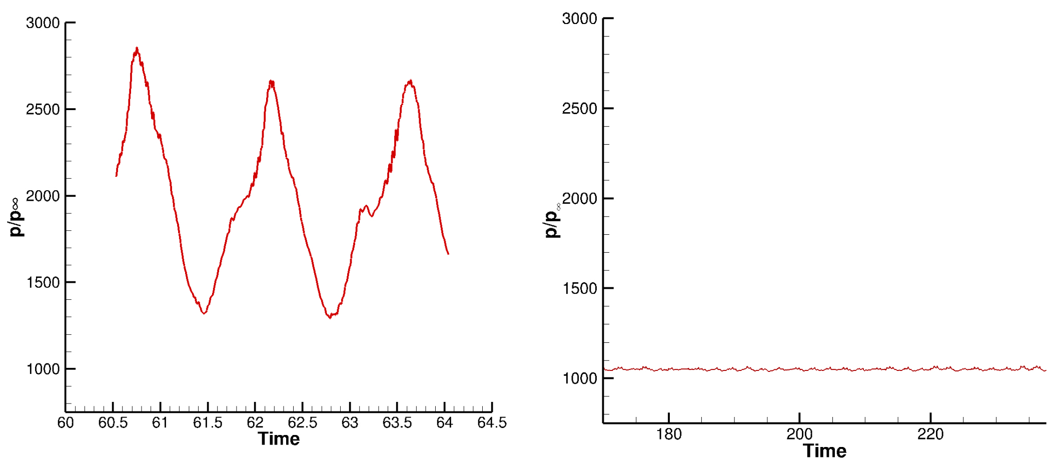

(a) $\Lambda = 0^0$, $z/D = 0.3016$, Coarse Grid

(b) $\Lambda = 22.5^0$, $z/D = 0.4079$

Figure 5.45: Normalized Pressure History

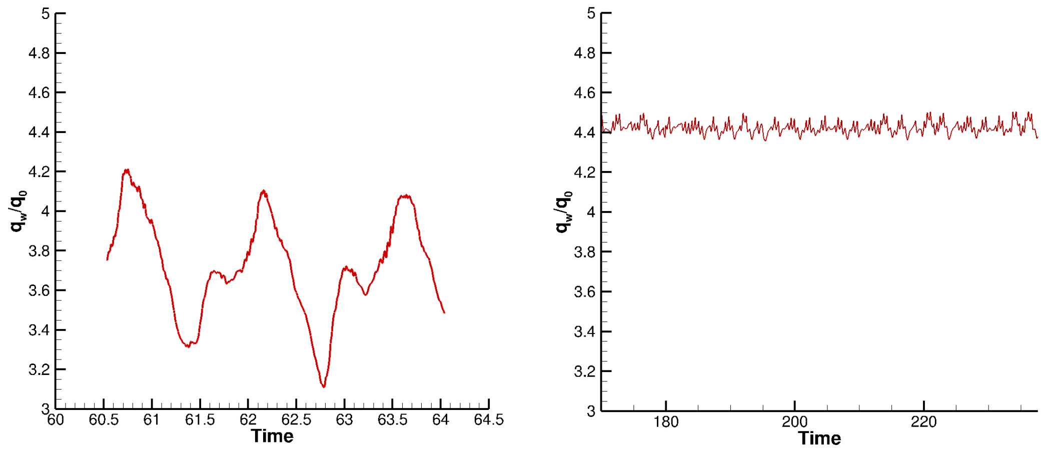

(a) $\Lambda = 0^0$, $z/D = 0.3016$, Coarse Grid

(b) $\Lambda = 22.5^0$, $z/D = 0.4079$

Figure 5.46: Normalized Heat Transfer History

The time-averaged heat transfer over multiple periods of the oscillation[1] has been calculated and compared with the experimental data (Figures 5.47(a) and 5.47(b)). The averaged heat transfer calculated in different periods of oscillation are almost identical, showing that the statistically stationary solution has been reached and one period of oscillation is an appropriate period to average the heat transfer through. The heat transfer in the experiment is normalized by the stagnation point heat transfer rate calculated by the method of Fay and Riddle [86]. In the numerical simulations, the heat transfer is normalized by the stagnation point heat transfer calculated at the stagnation point on the fin away from the shock wave boundary layer interaction in the zero degree sweep angle case. Good agreement with the experiment has been achieved, which validates the choice of the model and shows that laminar perfect gas model is appropriate to use for simulation of this problem. Although in the zero degree sweep angle case the computed peak heat transfer exceeds the experiment, since the heat transfer measurements were obtained on a coarser grid than in the computations, the actual experimental heat transfer may be higher. The spacing between the experimental measurements of the heat transfer normalized by the diameter of the fin is approximately

[1]For the zero degree sweep angle case and the coarse level of the grid, one period of oscillation -which is equivalent to 1.6 time scale, normalized by the freestream velocity and the diameter of the fin- is used to average the heat transfer over the fin.

0.1, which is one order of magnitude higher than the grid spacing in that direction for the numerical calculations. The influence of the attachment of the separated region on the fin at the reattachment point is evident from the increase in the localized heat transfer for both of the sweep angle cases. The maximum peak heat transfer, as well as the pressure, decreases with increase in the sweep angle of the fin, due to weaker shock wave boundary layer interaction in higher sweep angles of the fin.

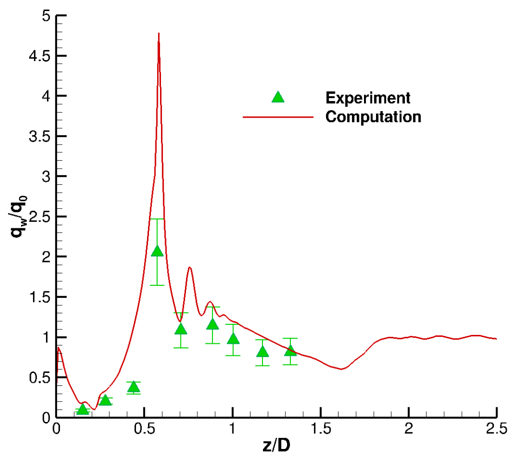

(a) $\Lambda = 0^0$

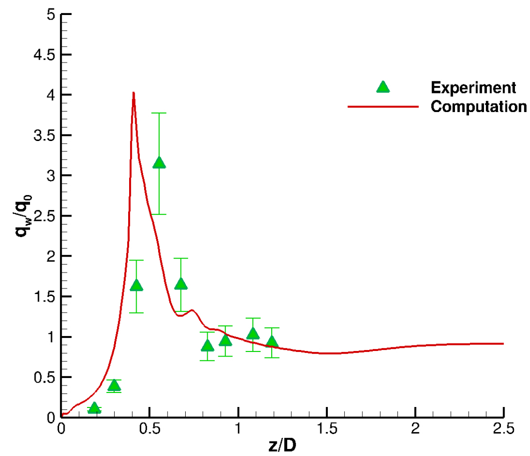

(b) $\Lambda = 22.5^0$

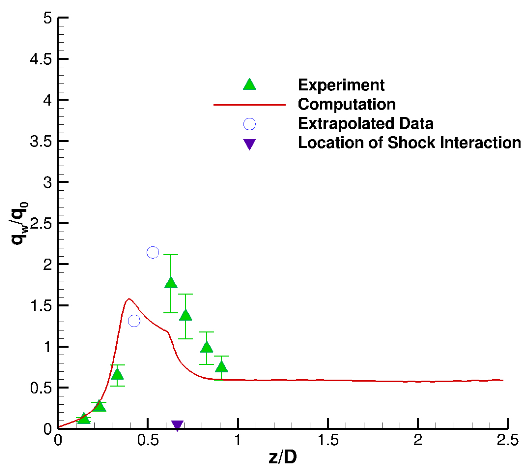

(c) $\Lambda = 45^0$

Figure 5.47: Heat Transfer

A grid refinement study with two additional levels of grid has been performed in this simulation. The grids used in this grid refinement study have been described in section 4.3.1. Since the zero degree sweep angle case has the strongest shock wave boundary layer interaction, it is the most sensitive case to the grid spacing; as a result, this case is chosen for the grid refinement study. Two levels of medium and fine grids are chosen to perform the grid refinement study. The fixed point $z/D = 0.5935$ on the centerplane is chosen for the medium and fine grids to observe the normalized pressure and heat transfer history throughout several time scales, and the results are presented in the Figures 5.48(a) through 5.49(b). The location of the observance of the pressure and heat transfer history has been chosen approximately at the location of the maximum heat transfer. The results for all the levels of the grid refinement study present a statistically stationary solution for the zero degree sweep angle case. The smallest and the most dominant Strouhal number -which is the non-dimensional frequency based on the freestream velocity and the diameter of the fin- in the coarse, medium and fine grids are 0.70, 0.42 and 0.41, respectively.

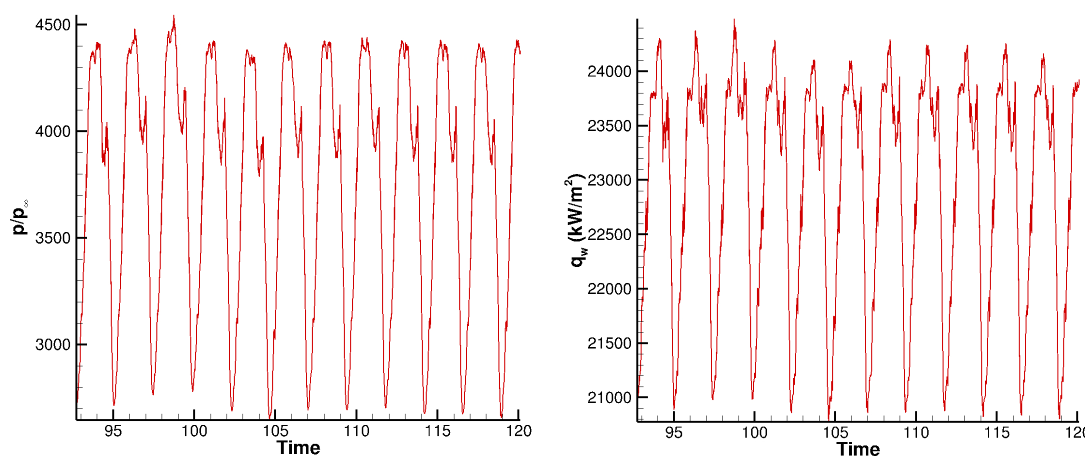

(a) Pressure History

(b) Heat Transfer History

Figure 5.48: Grid Refinement Study (Medium Grid)

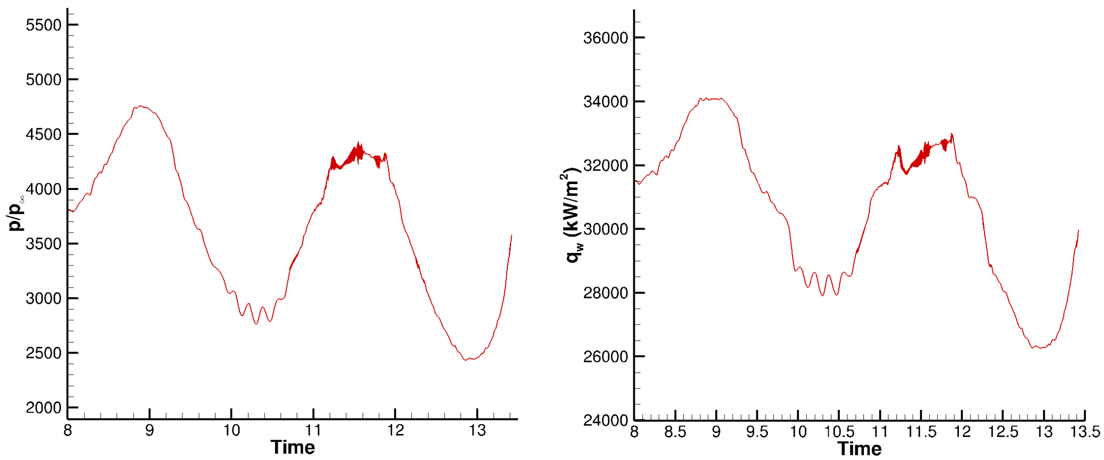

(a) Pressure History (b) Heat Transfer History

Figure 5.49: Grid Refinement Study (Fine Grid)

The averaged normalized heat transfer for the zero degree sweep angle calculations of all the levels of grid, in addition to the experimental measurements have been shown in Figure 5.50. The dotted curve represents the approximate analytical solution obtained by Hiers *et.al.* [69],[99]. The location of the maximum heat transfer has been accurately predicted by all the levels of the grid refinement study. The over prediction of the heat transfer in the numerical simulations is not necessarily a representative of an inaccurate solution. The measurements of the heat transfer in the experiment has been conducted in a coarser spacing compared with the extent of the maximum heat transfer rate. The heat transfer results of the three levels of the grid refinement study match very well over the fin, except for the maximum heat transfer, which requires considerably significant grid resolution. The average relative difference between the heat transfer calculations of the fine and medium grids is 8%, with the maximum relative difference of 29% focused at the location of the maximum heat transfer.

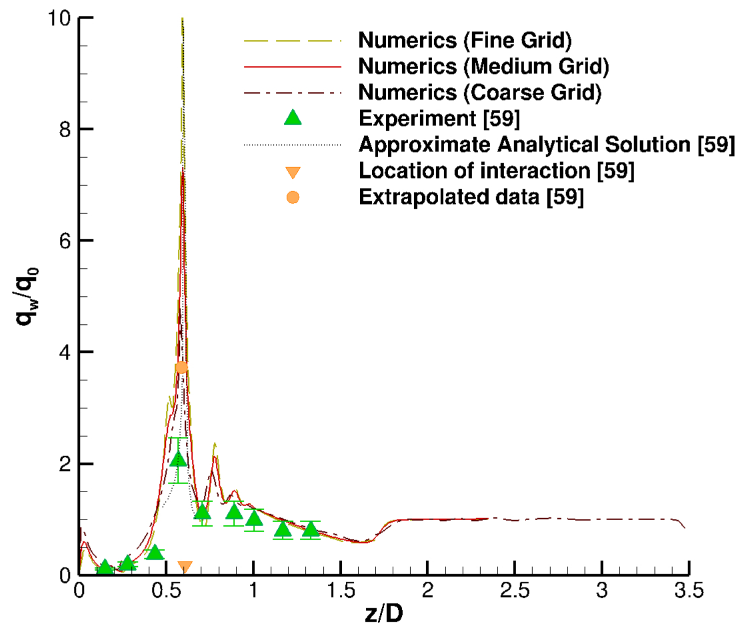

Figure 5.50: Heat Transfer, Grid Refinement Study

Chapter 6

Conclusion

In this research high speed flows are studied numerically and three separate experimental cases are considered to assess the capability of Euler or laminar Navier-Stokes and Ideal Gas equations to predict aerothermodynamic loads on high speed vehicles. The first case study is an instantaneous laser discharge in a flow at Mach 3.45 past a hemisphere, which was numerically simulated using the Euler and Navier-Stokes equations assuming a perfect gas model. The laser discharge is modeled as an instantaneous increase in pressure and temperature in a spherical volume and the same velocity and density as the freestream. The Euler and Navier-Stokes equations are solved to simulate the interaction of the heated region with the blunt body shock and the hemisphere surface. An initial increase in the centerline pressure is observed due to the interaction with the blast wave generated from the laser discharge. This pressure jump is matched with the experimental data [17] to determine the initial energy deposited in the spherical region according to the model. Comparison of the calculated and experimental surface centerline pressure indicates that a simple perfect gas model of laser energy deposition combined with either the Euler or laminar Navier-Stokes equations is incapable of accurately predicting the surface pressure time history. Therefore, a more physically realistic, non-equilibrium thermochemistry model of laser discharge combined with the non-equilibrium Navier-Stokes equations, is essential for accurate prediction of the aerodynamic effects of the interaction of an laser discharge with an aerodynamic body.

The second case study is the shock wave boundary layer interaction in a Mach 9.91 flow with Reynolds number of 18,375, which is numerically simulated and the results for the pressure coefficient is compared with the experiment [85]. The flare shock creates a separated region due to the adverse pressure gradient it imposes on the boundary layer. A separation shock wave forms over the separation zone which meets the boundary layer displacement shock and the flare shock at the reattachment point. A viscous perfect gas model is used to numerically simulate the complex flow structure using an MPI code developed in part by the author and validated using the exact solution of the compressible Blasius problem. The numerical calculations in this study agree with the experimental results [85], which validates the calculations presented in this Ph.D. dissertation.

The third case study is the shock wave laminar boundary layer interaction in a three dimensional geometry with a blunt fin mounted on a flat plate. The freestream has Mach number of 14, total enthalpy of 10.5 MJ/kg and Reynolds number, based on the diameter of the fin equal to 8,000. The blunt fin is rotatable around the flat plate, allowing us to study the effects of the sweep angle on the flow parameters, specifically the heat transfer rate on the blunt fin. The average Reynolds number based on the diameter of the cylindrical blunt fin at the test section, which is 8,000, indicates that the shock wave boundary layer interaction is laminar. Three different sweep angles of zero and 22.5 and 45 degree have been studied in this research.

The blunt body shock generated upstream the blunt fin interacts with the boundary layer over the flat plate and separates the boundary layer with multiple vortices inside the separation region. Due to the stronger blunt fin shock waves upstream the fins with smaller sweep angles, the separated region decreases in size dramatically by increase in the sweep angle of the fin. As the boundary layer reattaches on the solid surface over the fin, a reattachment shock wave forms creating a peak pressure on the solid wall. Moreover, the heat transfer rate reaches its maximum level at the reattachment point, where the boundary layer thickness is minimum. Temporal oscillations in the flow parameters and shock waves and slip-lines in the zero degree sweep angle case are captured. The Discrete Fourier Transform analysis show that the statistically stationary solution has been reached for the zero degree case, while the 22.5 and 45 degree cases are steady. The Strouhal numbers of the oscillations in the zero degree sweep angle case for the coarse, medium and fine grids are 0.70, 0.42 and 0.41, respectively. Moreover, the maximum pressure and heat transfer decreases by increase in the sweep angle of the fin.

The numerical calculations are based on the laminar, perfect gas model with Navier-Stokes and Ideal Gas equations, which are solved using an MPI code written in C++ language partially by the author. No-slip isothermal boundary condition is used for the solid walls in the computational domain. Experimental results of the Hiers *et.al.*[69] for the normalized heat transfer on the centerline of the blunt fin are used to compare with the numerical calculations to assess the capability of the model chosen in this study to predict the flow parameters in such hypersonic regimes. Good agreement with the experimental data validates our numerical calculations and the choice of the model.

All the simulations in this Ph.D. dissertation are based on a perfect gas model. For the future work, real gas effects should be studied in both flow control with energy discharge, as well as the shock wave/boundary layer interactions with high total enthalpies.

References

[1] Anderson, J., *Hypersonic and High Temperature Gas Dynamics*, AIAA, New York, 2000.

[2] Nelson, R., *National Innovation Systems: A Comparative Analysis*, Oxford University Press, 1993.

[3] Stone, D., Lindenmoyer, A., French, G., Musk, E., Gump, D., Kathuria, C., Miller, C., Sirangelo, M., and Pickens, T., "NASA's Approach to Commercial Cargo and Crew Transportation," *Acta Astronautica*, Vol. 63, No. 1, 2008, pp. 192–197. doi:10.1016/j.actaastro.2007.12.004.

[4] Valentine, P., Rivers, K., and Chen, V., "X-37 C-Sic CMC Control Surface Components Development Status of the NASA/Boeing/USAF Orbital Vehicle and Related Efforts," Tech. rep., NASA Marshall Space Flight Center, January 2004.

[5] Ross, J. and Schuster, D., "Orion Multi-Purpose Crew Vehicle (MPCV) Capsule Parachute Assembly System (CPAS) Wake Deficit Wind Tunnel Testing," Technical Report NASA/TM-2014-218171, L-20384, NESC-RP-11-00697, NF1676L-18396, NASA Langley Research Center, February 2014.

[6] Crouch, G., Devinney, T., Louviere, J., and Islam, T., "Modelling Consumer Choice Behaviour in Space Tourism," *Tourism Management*, Vol. 30, No. 3, 2009, pp. 441–454. doi:10.1016/j.tourman.2008.07.003.

[7] Maull, D., "Hypersonic Flow Over Axially Symmetric Spiked Bodies," *Journal of Fluid Mechanics*, Vol. 8, No. 4, 1960, pp. 584–592. doi:10.1017/S0022112060000815.

[8] Crawford, D., "Investigations of the Flow Over a Spiked-Nose Hemisphere-Cylinder," *NASA TN D-118*, 1959.

[9] Knight, D., "Survey of Aerodynamic Drag Reduction at High Speed by Energy Deposition," *Journal of Propulsion and Power*, Vol. 24, No. 6, 2008, pp. 1153–1167. doi:10.2514/1.24595.

[10] Belokon, V., Rudenko, O., and Khokhlov, R., "Aerodynamic Effects of Supersonic-Flow Past a Laser-Beam," *Soviet Physics Acoustic-Ussr*, Vol. 23, No. 4, 1977, pp. 361–362.

[11] Krasnobaev, K. and Syunyaev, R., "Calculation of Flow of Stellar Wind Past an X-Ray Source," *Fluid Dynamics*, Vol. 18, No. 4, 1983, pp. 584–589. doi:10.1007/BF01090625.

[12] Krasnobaev, K., "Supersonic Flow Past Weak Sources of Radiation," *Fluid Dynamics*, Vol. 19, No. 4, 1984, pp. 629–632. doi:10.1007/BF01091088.

[13] Terent'eva, L., "Supersonic Flow Over Energy-Releasing Sources," *Fluid Dynamics*, Vol. 27, No. 5, 1992, pp. 747–750. doi:10.1007/BF01051619.

[14] Tretyakov, P., Kraynev, V., Yakovlev, V., Grachev, G., Ivanchenko, A., Ponomarenko, A., and Tischenko, V., "A Powerful Optical Pulsating Discharge as a Source of Energy Release in a Supersonic Flow," *Proceedings of the 7th International Conference on Methods in Aerophysical Research*, Novosibirsk, Russia, 1994, pp. 224–228.

[15] Tretyakov, P., Garanin, A., Kraynev, V., Tupikin, A., and Yakovlev, V., "Investigation of Local Laser Energy Release Influence on Supersonic Flow by Methods of Aerophysical Experiments," *International Conference on the Methods of Aerophysical Research: Proc. Pt*, Vol. 1, Novosibirsk, Russia, 1996, pp. 200–203.

[16] Zaidi, S., Shneider, M., Mansfield, D., Ionikh, Y., and Miles, R., "Influence of Upstream Pulsed Energy Deposition on a Shockwave Structure in Supersonic Flow," AIAA Paper 2002-2703, American Institute of Aeronautics and Astronautics, 2002. doi:10.2514/6.2002-2703.

[17] Adelgren, R., Yan, H., Elliott, G., Knight, D., Beutner, T., and Zheltovodov, A., "Control of Edney IV Interaction by Pulsed Laser Energy Deposition," *AIAA Journal*, Vol. 43, No. 2, 2005, pp. 256–269. doi:10.2514/1.7036.

[18] Sakai, T., Sekiya, Y., Mori, K., and Sasoh, A., "Interaction Between Laser-Induced Plasma and Shock Wave Over a Blunt Body in a Supersonic Flow," *Proceedings of the Institution of Mechanical Engineers, Part G: Journal of Aerospace Engineering*, Vol. 222, No. 5, 2008, pp. 605–617. doi:10.1243/09544100JAERO294.

[19] Vlasov, V., Grudnitskii, B., and Rygalin, V., "Gas Dynamics with Local Energy Release in Subsonic and Supersonic Flow," *Fluid Dynamics*, Vol. 30, No. 2, 1995, pp. 275–280. doi:10.1007/BF02029841.

[20] Levin, V. and Terent'eva, L., "Supersonic Flow over a Cone with Heat Release in the Neighborhood of the Apex," *Fluid Dynamics*, Vol. 28, No. 2, 1993, pp. 244–247. doi:10.1007/BF01051214.

[21] Levin, V. and Terent'eva, L., "Effect of a Local Energy Supply Region on 3-D Flow Around a Cone," *Fluid Dynamics*, Vol. 34, No. 3, 1999, pp. 388–394.

[22] Riggins, D., Nelson, H., and Johnson, E., "Blunt-Body Wave Drag Reduction Using Focused Energy Deposition," *AIAA Journal*, Vol. 37, No. 4, 1999, pp. 460–467. doi:10.2514/2.756.

[23] Riggins, D. and Nelson, H., "Hypersonic Flow Control Using Upstream Focused Energy Deposition," *AIAA Journal*, Vol. 38, No. 4, 2000, pp. 723–725. doi:10.2514/2.1020.

[24] Georgievskii, P. and Levin, V., "Unsteady Interaction of a Sphere with Atmospheric Temperature Inhomogeneity at Supersonic Speed," *Fluid Dynamics*, Vol. 28, No. 4, 1993, pp. 568–574. doi:10.1007/BF01342694.

[25] Georgievskii, P. and Levin, V., "Control of the Flow Past Bodies Using Localized Energy Addition to the Supersonic Oncoming Flow," *Fluid Dynamics*, Vol. 38, No. 5, 2003, pp. 794–805. doi:10.1023.

[26] Kandala, R. and Candler, G., "Numerical Studies of Laser-Induced Energy Deposition for Supersonic Flow Control," *AIAA Journal*, Vol. 42, No. 11, 2004, pp. 2266–2275. doi:10.2514/1.6817.

[27] Ogino, Y., Ohnishi, N., Taguchi, S., and Sawada, K., "Baroclinic Vortex Influence on Wave Drag Reduction Induced by Pulse Energy Deposition," *Physics of Fluids*, Vol. 21, No. 6, 2009, pp. 066102. doi:10.1063/1.3147932.

[28] Zheltovodov, A., Pimonov, E., and Knight, D., "Energy Deposition Influence on Supersonic Flow Over Axisymmetric Bodies," AIAA Paper 2007-1230, American Institute of Aeronautics and Astronautics, 2007. doi:10.2514/6.2007-1230.

[29] "Aerosoft Inc. GASPex Blacksburg, Virginia," http://www.aerosoftinc.com, 2009.

[30] Délery, J. and Dussauge, J., "Some Physical Aspects of Shock Wave/Boundary Layer Interactions," *Shock Waves*, Vol. 19, No. 6, 2009, pp. 453–468. doi:10.1007.

[31] Délery, J., Marvin, J. G., and Reshotko, E., "Shock-Wave Boundary Layer Interactions," Tech. Rep. AGARD-AG-280, DTIC Document, 1986.

[32] Dolling, D., "Fifty Years of Shock-Wave/Boundary-Layer Interaction Research: What Next?" *AIAA Journal*, Vol. 39, No. 8, 2001, pp. 1517–1531. doi:10.2514/2.1476.

[33] Gaitonde, D., "Progress in Shock Wave/Boundary Layer Interactions," *Progress in Aerospace Sciences*, Vol. 72, 2015, pp. 80–99. doi:10.1016/j.paerosci.2014.09.002.

[34] Knight, D., Yan, H., Panaras, A., and Zheltovodov, A., "Advances in CFD Prediction of Shock Wave Turbulent Boundary Layer Interactions," *Progress in Aerospace Sciences*, Vol. 39, No. 2, 2003, pp. 121–184.

[35] Chanetz, B., "Low and High Enthalpy Shock Wave/Boundary Layer Interactions Around Cylinder-Flare Models," *Progress in Flight Physics*, Vol. 3, EDP Sciences, 2012, pp. 107–118. doi:10.1051/eucass/201203107.

[36] Chanetz, B., Pot, T., Bur, R., Joly, V., Larigaldie, S., Lefebvre, M., Marmignon, C., Mohamed, A. K., Perraud, J., Pigache, D., et al., "High-Enthalpy Hypersonic Project at ONERA," *Aerospace Science and Technology*, Vol. 4, No. 5, 2000, pp. 347–361. doi:10.1016/S1270-9638(00)00145-0.

[37] Bur, R. and Chanetz, B., "Experimental Study on the PRE-X Vehicle Focusing on the Transitional Shock-Wave/Boundary-Layer Interactions," *Aerospace Science and Technology*, Vol. 13, No. 7, 2009, pp. 393–401. doi:10.1016/j.ast.2009.09.002.

[38] Boldyrev, S., Borovoy, V., Chinilov, A., Gusev, V., Krutiy, S., Struminskaya, I., Yakovleva, L., Délery, J., and Chanetz, B., "A Thorough Experimental Investigation of Shock/Shock Interferences in High Mach Number Flows," *Aerospace Science and Technology*, Vol. 5, No. 3, 2001, pp. 167–178. doi:10.1016/S1270-9638(01)01094-X.

[39] Swantek, A. and Austin, J., "Flowfield Establishment in Hypervelocity Shock-Wave/Boundary-Layer Interactions," *AIAA Journal*, Vol. 53, No. 2, 2014, pp. 311–320. doi:10.2514/1.J053104.

[40] Holden, M. and Wadhams, T., "Code Validation Study of Laminar Shock/Boundary Layer and Shock/Shock Interactions in Hypersonic Flow, Part A: Experimental Measurements," AIAA Paper 2001-1031, American Institute of Aeronautics and Astronautics, 2001.

[41] Harvey, J., Holden, M., and Wadhams, T., "Code Validation Study of Laminar Shock/Boundary Layer and Shock/Shock Interactions in Hypersonic Flow Part B: Comparison with Navier-Stokes and DSMC Solutions," AIAA Paper 2001-1031, American Institute of Aeronautics and Astronautics, 2001.

[42] Wright, M., Sinha, K., Olejniczak, J., Candler, G., Magruder, T., and Smits, A., "Numerical and Experimental Investigation of Double-Cone Shock Interactions," *AIAA Journal*, Vol. 38, No. 12, 2000, pp. 2268–2276.

[43] Neuenhahn, T. and Olivier, H., "Influence of the Wall Temperature and the Entropy Layer Effects on Double Wedge Shock Boundary Layer Interactions," AIAA Paper 2006-8136, American Institute of Aeronautics and Astronautics, 2006. doi:10.2514/6.2006-8136.

[44] Coet, M., "Etude experimentale de l'effet d'une couche d'entropie sur l'interaction onde de choc/couche limite en ecoulement hypersonique," *Rapport Complementaire, ONERA, Rapport Final no. 29/4362 AY*, 1992.

[45] Coet, M., Chanetz, B., and Delery, J., "Shock-Wave Boundary Layer Interaction with Entropy Layer Effect in Hypersonic Flow," *ONERA, Colloque sur les Ecoulements Hypersoniques, Garchy, France*, 1992.

[46] Borovoy, V., Egorov, I., Skuratov, A., and Struminskaya, I., "Two-Dimensional Shock-Wave/Boundary-Layer Interaction in the Presence of Entropy Layer," *AIAA Journal*, Vol. 51, No. 1, 2012, pp. 80–93. doi:10.2514/1.J051496.

[47] John, B. and Kulkarni, V., "Effect of Leading Edge Bluntness on the Interaction of Ramp Induced Shock Wave with Laminar Boundary Layer at Hypersonic Speed," *Computers & Fluids*, Vol. 96, 2014, pp. 177–190. doi:10.1016/j.compfluid.2014.03.004.

[48] John, B. and Kulkarni, V., "Numerical Assessment of Correlations for Shock Wave Boundary Layer Interaction," *Computers & Fluids*, Vol. 90, 2014, pp. 42–50.

[49] Needham, D. and Stollery, J., "Hypersonic Studies of Incipient Separation and Separated Flows (Schlieren Photography, and Heat Transfer and Pressure Surface Measurements of Transitional and Laminar Boundary Layer Separations)," *1966.*, 1966, pp. 89–119.

[50] Holden, M., "Boundary-Layer Displacement and Leading-Edge Bluntness Effects on Attached and Separated Laminar Boundary Layers in a Compression Corner. II-Experimental Study," *AIAA Journal*, Vol. 9, No. 1, 1971, pp. 84–93. doi:10.2514/3.6084.

[51] Hankey Jr, W. and Holden, M., "Two-Dimensional Shock Wave-Boundary Layer Interactions in High Speed Flows," Tech. rep., DTIC Document, 1975.

[52] Katzer, E., "On the Lengthscales of Laminar Shock/Boundary-Layer Interaction," *Journal of Fluid Mechanics*, Vol. 206, 1989, pp. 477–496. doi:10.1017/S0022112089002375.

[53] Druguet, M., Candler, G., and Nompelis, I., "Effects of Numerics on Navier-Stokes Computations of Hypersonic Double-Cone Flows," *AIAA Journal*, Vol. 43, No. 3, 2005, pp. 616–623. doi:10.2514/1.6190.

[54] Gaitonde, D., Canupp, P., and Holden, M., "Heat Transfer Predictions in a Laminar Hypersonic Viscous/Inviscid Interaction," *Journal of Thermophysics and Heat Transfer*, Vol. 16, No. 4, 2002, pp. 481–489.

[55] Grasso, F. and Marini, M., "Analysis of Hypersonic Shock-Wave Laminar Boundary-Layer Interaction Phenomena," *Computers & Fluids*, Vol. 25, No. 6, 1996, pp. 561–581.

[56] Olejniczak, J., Wright, M., and Candler, G., "Numerical Study of Shock Interactions on Double-Wedge Geometries," AIAA Paper 1996-0041, American Institute of Aeronautics and Astronautics, 1996.

[57] Nompelis, I. and Candler, G., "Numerical Investigation of Double-Cone Flow Experiments with High-Enthalpy Effects," AIAA Paper 2010-1283, American Institute of Aeronautics and Astronautics, January 2010. doi:10.2514/6.2010-1283.

[58] Gnoffo, P., "CFD validation studies for hypersonic flow prediction," AIAA Paper 2001-1025, American Institute of Aeronautics and Astronautics, 2001. doi:10.2514/6.2001-1025.

[59] Roy, C., Gallis, M., Bartel, T., and Payne, J., "Navier-Stokes and DSMC Simulations for Hypersonic Laminar Shock-Shock Interaction Flows," AIAA Paper 2002-737, American Institute of Aeronautics and Astronautics, 2002.

[60] Marini, M., "Effects of Flow and Geometry Parameters on Shock-Wave Boundary-Layer Interaction Phenomena," AIAA Paper 1998-1570, American Institute of Aeronautics and Astronautics, 1998. doi:10.2514/6.1998-1570.

[61] Gai, S. and Hayne, M., "Heat Transfer Behind a Step in High-Enthalpy Laminar Hypersonic Flow," *Journal of Thermophysics and Heat Transfer*, Vol. 24, No. 4, 2010, pp. 839–841. doi:10.2514/1.49300.

[62] John, B., Kulkarni, V. N., and Natarajan, G., "Shock Wave Boundary Layer Interactions in Hypersonic Flows," *International Journal of Heat and Mass Transfer*, Vol. 70, 2014, pp. 81–90. doi:10.1016/j.ijheatmasstransfer.2013.10.072.

[63] Houwing, A., Smith, D., Fox, J., Danehy, P., and Mudford, N., "Laminar boundary Layer Separation at a Fin-Body Junction in a Hypersonic Flow," *Shock Waves*, Vol. 11, No. 1, 2001, pp. 31–42.

[64] Wang, S., Ren, Z., and Wang, Y., "Effects of Mach Number on Turbulent Separation Behaviours Induced by Blunt Fin," *Experiments in Fluids*, Vol. 25, No. 4, 1998, pp. 347–351.

[65] Dolling, D. S., "Comparison of Sharp and Blunt Fin-Induced Shock Wave/Turbulent Boundary-Layer Interaction," *AIAA Journal*, Vol. 20, No. 10, 1982, pp. 1385–1391.

[66] Dolling, D. and Bogdonoff, S., "Blunt Fin-Induced Shock Wave/Turbulent Boundary-Layer Interaction," *AIAA Journal*, Vol. 20, No. 12, 1982, pp. 1674–1680.

[67] Hung, C. and Buning, P., "Simulation of Blunt-Fin-Induced Shock-Wave and Turbulent Boundary-Layer Interaction," *Journal of Fluid Mechanics*, Vol. 154, 1985, pp. 163–185.

[68] Chanetz, B., Benay, R., Bousquet, J., Bur, R., Pot, T., Grasso, F., and Moss, J., "Experimental and Numerical Study of the Laminar Separation in Hypersonic Flow," *Aerospace Science and Technology*, Vol. 2, No. 3, 1998, pp. 205–218. doi:10.1016/S1270-9638(98)80054-0.

[69] Hiers, R. and Loubsky, W., "Effects of Shock-Wave Impingement on the Heat Transfer on a Cylindrical Leading Edge," Tech. Rep. NASA TN D-3859, 1967.

[70] Knight, D., *Elements of Numerical Methods for Compressible Flows*, Vol. 19, Cambridge University Press, New York, 2006.

[71] Roe, P., "Approximate Riemann Solvers, Parameter Vectors, and Difference Schemes," *Journal of Computational Physics*, Vol. 43, No. 2, 1981, pp. 357–372. doi:10.1016/0021-9991(81)90128-5.

[72] Roe, P., "Characteristic-Based Schemes for the Euler Equations," *Annual Review of Fluid Mechanics*, Vol. 18, No. 1, 1986, pp. 337–365. doi:10.1146/annurev.fl.18.010186.002005.

[73] Van Leer, B., "Flux-Vector Splitting for the Euler Equation," *Upwind and High-Resolution Schemes*, Springer, 1997, pp. 80–89.

[74] Colella, P., "A Direct Eulerian MUSCL Scheme for Gas Dynamics," *SIAM Journal on Scientific and Statistical Computing*, Vol. 6, No. 1, 1985, pp. 104–117. doi:10.1137/0906009.

[75] Harten, A., Engquist, B., Osher, S., and Chakravarthy, S., "Uniformly High Order Accurate Essentially Non-Oscillatory Schemes, III," *Journal of Computational Physics*, Vol. 71, No. 2, 1987, pp. 231–303. doi:10.1016/0021-9991(87)90031-3.

[76] Harten, A. and Osher, S., "Uniformly High-Order Accurate Nonoscillatory Schemes. I," *SIAM Journal on Numerical Analysis*, Vol. 24, No. 2, 1987, pp. 279–309. doi:10.1137/0724022.

[77] Van Albada, G., Van Leer, B., and Roberts Jr, W., "A Comparative Study of Computational Methods in Cosmic Gas Dynamics," *Upwind and High-Resolution Schemes*, Springer, 1997, pp. 95–103.

[78] Jameson, A., Schmidt, W., and Turkel, E., "Numerical solutions of the Euler equations by finite volume methods using Runge-Kutta time-stepping schemes," AIAA Paper 1981-1259, American Institute of Aeronautics and Astronautics, January 1981.

[79] Gottlieb, S. and Shu, C., "Total Variation Diminishing Runge-Kutta Schemes," *Mathematics of Computation of the American Mathematical Society*, Vol. 67, No. 221, 1998, pp. 73–85. doi:10.1090/S0025-5718-98-00913-2.

[80] Wright, M., Candler, G., and Bose, D., "Data-Parallel Line Relaxation Method for the Navier-Stokes Equations," *AIAA Journal*, Vol. 36, No. 9, 1998, pp. 1603–1609. doi:10.2514/2.586.

[81] Withington, J., Yang, V., and Shuen, J., "A Time-Accurate Implicit Method for Chemically Reacting Flows at All Mach Numbers," *29th Aerospace Sciences Meeting*, 1991.

[82] Hoffmann, K. A. and Chiang, S. T., *Computational Fluid Dynamics Volume I*, Engineering Education System, Wichita, Kansas, USA, 2000.

[83] Adelgren, R. G., "Localized Flow Control with Energy Deposition," Tech. rep., Rutgers, The State University of New Jersey, 2002.

[84] Jiang, Z., Takayama, K., Moosad, K., Onodera, O., and Sun, M., "Numerical and Experimental Study of a Micro-Blast Wave Generated by Pulsed-Laser Beam Focusing," *Shock Waves*, Vol. 8, No. 6, 1998, pp. 337–349. doi:10.1007.

[85] Chanetz, B., "Study of Axisymmetric Shock Wave/Boundary Layer Interaction in Hypersonic Laminar Flow," *ONERA Report RT*, Vol. 42, 1995, pp. 4365.

[86] Fay, J., "Theory of Stagnation Point Heat Transfer in Dissociated Air," *Journal of the Aerospace Sciences*, Vol. 25, No. 2, 1958, pp. 73–85. doi:10.2514/8.7517.

[87] Sedov, L., "General Theory of One-Dimensional Motion of Gas," *Dokl. Akad. Nauk SSSR*, Vol. 85, 1952, pp. 723–726.

[88] Korobeĭnikov, V., *Problems in the Theory of Point Explosion in Gases*, Vol. 119, American Mathematical Soc., 1976.

[89] Quirk, J., "An Alternative to Unstructured Grids for Computing Gas Dynamic Flows Around Arbitrarily Complex Two-Dimensional Bodies," *Computers & Fluids*, Vol. 23, No. 1, 1994, pp. 125–142. doi:10.1016/0045-7930(94)90031-0.

[90] Van Leer, B., "On the Relation between the Upwind-Differencing Schemes of Godunov, Engquist-Osher and Roe," *SIAM Journal on Scientific and Statistical Computing*, Vol. 5, No. 1, 1984, pp. 1–20. doi:10.1137/0905001.

[91] Sutherland, W., "LII. The Viscosity of Gases and Molecular Force," *The London, Edinburgh, and Dublin Philosophical Magazine and Journal of Science*, Vol. 36, No. 223, 1893, pp. 507–531. doi:10.1080/14786449308620508.

[92] Richtmyer, R., "Taylor Instability in Shock Acceleration of Compressible Fluids," *Communications on Pure and Applied Mathematics*, Vol. 13, No. 2, 1960, pp. 297–319. doi:10.1002/cpa.3160130207.

[93] Meshkov, E., “Instability of the Interface of Two Gases Accelerated by a Shock Wave,” *Fluid Dynamics*, Vol. 4, No. 5, 1969, pp. 101–104. doi:10.1007/BF01015969.

[94] Schülein, E., Zheltovodov, A., Pimonov, E., and Loginov, M., “Experimental and Numerical Modeling of the Bow Shock Interaction with Pulse-Heated Air Bubbles,” *International Journal of Aerospace Innovations*, Vol. 2, No. 3, 2010.

[95] Mortazavi, M., Knight, D., Azarova, O., Shix, J., and Yan, H., “Numerical Simulation of Energy Deposition in a Supersonic Flow Past a Hemisphere,” AIAA Paper 2014-944, American Institute of Aeronautics and Astronautics, January 2014. doi:10.2514/6.2014-0944.

[96] Brusniak, L. and Dolling, D., “Physics of Unsteady Blunt-Fin-Induced Shock Wave/Turbulent Boundary Layer Interactions,” *Journal of Fluid Mechanics*, Vol. 273, 1994, pp. 375–409. doi:10.1017/S0022112094001989.

[97] Helmholtz, H. v., “LXIII. On Integrals of the Hydrodynamical Equations, Which Express Vortex-Motion,” *The London, Edinburgh, and Dublin Philosophical Magazine and Journal of Science*, Vol. 33, No. 226, 1867, pp. 485–512.

[98] Tobak, M. and Peake, D., “Topology of Three-Dimensional Separated Flows,” *Annual Review of Fluid Mechanics*, Vol. 14, No. 1, 1982, pp. 61–85.

[99] Schlichting, H., Gersten, K., Krause, E., and Oertel, H., *Boundary-layer theory*, Vol. 7, Springer, 1955.